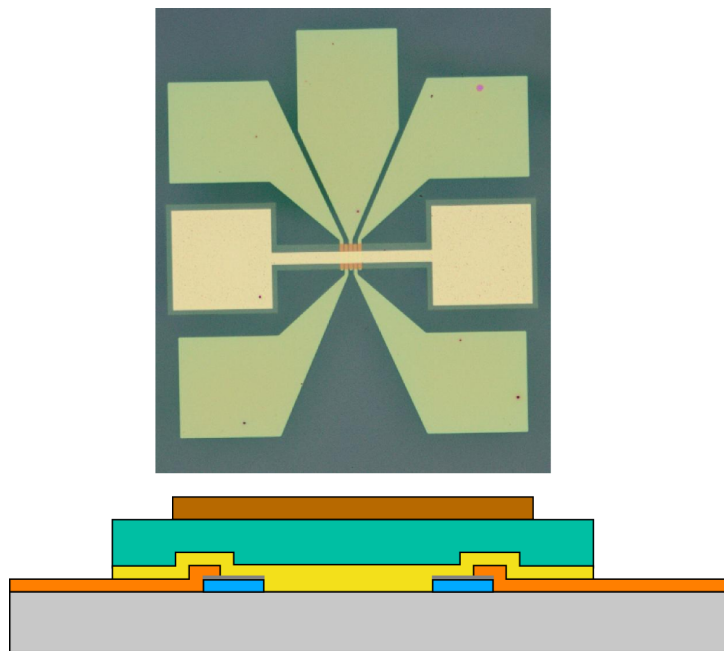


# Fabrication of a magnetic O-FET based on a semiconducting polymer for spin accumulation measurements



Master Thesis  
January, 2014

*Author*

Frans van Wijngaarden

*Graduation committee*

prof.dr. W.G. van der Wiel  
prof.dr. J.W.M. Hilgenkamp  
dr. M.P. de Jong  
K. Wang, MPhil

UNIVERSITY OF TWENTE.

NANO ELECTRONICS.



## Abstract

Presented in this work are the results of a masters assignment at the NanoElectronics research chair of the University of Twente, the Netherlands. The goal of this assignment was to develop a magnetic organic field-effect transistor, which can be used for spin accumulation measurements. The organic layer is the polymer poly(3-hexylthiophene). In such a device, the injection of a spin polarised current is achieved by using a ferromagnetic material for both the source and the drain contacts. Both a back-gated and a top-gated geometry was developed. For a back-gated magnetic O-FET device, the fabrication process is short and uncomplicated. However, this geometry has disadvantages when compared to a top-gated magnetic O-FET device. Experiments have been designed and realised to develop the fabrication recipe, focussing on obtaining high-quality magnetic electrodes without ridges at the edge of the electrodes. This is achieved by using an image reversal photoresist with a pronounced undercut, in combination with lift-off photolithography. Furthermore, the process of spin-coating the organic polymer was tested.

For the spin-coating process, different organic solvents were tested to ensure no negative reactions occurred with the magnetic injection electrodes. As a result of these tests, 1,2-dichlorobenzene was selected as the solvent for poly(3-hexylthiophene). The spin-coating process was calibrated, resulting in a range of available thicknesses of approximately 10-40 nm, selectable by adjusting the spin-coating rotational speed.

To achieve high-quality magnetic electrodes, Ti35 image reversal photoresist was used to obtain a pronounced undercut. The specific recipe for applying this photoresist was tested, and the resulting photoresist profiles were imaged using scanning electron microscopy. These measurements show that a good undercut is achieved. Both back-gated and top-gated O-FET devices have been fabricated, and preliminary electrical measurements were performed on these devices. Difficulties with etching of the magnetic electrodes were traced to the organic solvent used for lift-off, and were solved by changing the organic solvent to a more suitable one. A combination of AFM and dark field microscopy images indicate that this mostly prevents the etching of magnetic electrodes. AFM measurements also indicate that lift-off is achieved without ridges on the edge of the electrodes, although some surface roughness is still observed in between the electrodes.

In this work, major progress is reported on the fabrication recipe for magnetic O-FET devices. The optimisation of a method to obtain high-quality magnetic electrodes is a crucial step, since any imperfections in these electrodes will negatively influence the spin polarisation of the injected current. However, the fabrication recipe is not yet completely tested and optimised. Furthermore, no spin accumulation measurements have yet been done. In addition to many small improvements, three critical steps remain to be optimised in the fabrication recipe. The first step is finding a solution for the etching that is observed on the magnetic electrodes. Although the major etching problem is solved, minor etching pits are still visible. The second step is the organic etching step, using reactive ion beam etching. The third step is the integration of electron-beam lithography into the recipe, since it is suspected that a four-terminal device may be necessary for spin accumulation measurements. In such a device, two of the four terminals need to be closer together than is achievable using photolithography.



# Contents

	Page
<b>1 Introduction</b>	<b>1</b>
1.1 Spintronics . . . . .	1
1.1.1 Ferromagnetism . . . . .	1
1.1.2 Semiconductor spintronics . . . . .	6
1.2 Organic semiconductors . . . . .	7
1.2.1 Molecular orbitals . . . . .	8
1.2.2 Charge transport . . . . .	8
1.2.3 Spintronics using organic materials . . . . .	10
1.2.4 P3HT . . . . .	11
1.2.5 Organic field-effect transistor . . . . .	12
1.3 Spin measurement methods . . . . .	13
1.3.1 Magneto-transport methods . . . . .	13
1.4 Motivation . . . . .	14
<b>2 Theory</b>	<b>17</b>
2.1 Charge transport in organic materials . . . . .	17
2.2 Organic field-effect transistor . . . . .	18
2.3 Spin transport . . . . .	20
2.3.1 Spin scattering . . . . .	22
2.3.2 Spin-orbit coupling . . . . .	22
2.4 Spin transport in organic materials . . . . .	23
2.5 Hanle measurement . . . . .	24
<b>3 Experimental methods</b>	<b>27</b>
3.1 Fabrication . . . . .	27
3.1.1 Photolithography . . . . .	27
3.1.2 Deposition techniques . . . . .	28
3.1.3 Organic layer coating . . . . .	30
3.1.4 Reactive ion beam etching . . . . .	31
3.2 Characterisation . . . . .	32
3.2.1 Optical microscopy . . . . .	32
3.2.2 Atomic force microscopy . . . . .	33
3.2.3 Scanning electron microscopy . . . . .	33
3.2.4 Electrical measurements . . . . .	33

<b>4</b>	<b>Device fabrication and characterisation</b>	<b>37</b>
4.1	Organic solvent compatibility . . . . .	37
4.1.1	Magnetic tunnel junctions . . . . .	37
4.2	P3HT thickness . . . . .	38
4.3	Photoresist optimisation . . . . .	39
4.4	Back-gated O-FET . . . . .	40
4.5	Top-gated O-FET . . . . .	41
4.5.1	Electrical characterisation . . . . .	43
<b>5</b>	<b>Results &amp; discussion</b>	<b>45</b>
5.1	Organic solvent compatibility . . . . .	45
5.2	P3HT thickness . . . . .	48
5.3	Photoresist optimisation . . . . .	48
5.4	Back-gated O-FET . . . . .	53
5.4.1	Lift-off photolithography . . . . .	53
5.4.2	Electrical characterisation . . . . .	54
5.5	Top-gated O-FET . . . . .	60
5.5.1	Device fabrication procedure . . . . .	60
5.5.2	Electrical characterisation . . . . .	68
<b>6</b>	<b>Conclusion</b>	<b>71</b>
6.1	Recommendations . . . . .	71
6.1.1	Minor recommendations . . . . .	72
	<b>Acknowledgements</b>	<b>75</b>
	<b>List of Acronyms</b>	<b>77</b>
	<b>Bibliography</b>	<b>79</b>
<b>A</b>	<b>Fabrication recipes</b>	<b>85</b>
A.1	Top-gated organic field-effect transistor . . . . .	85
A.1.1	Preparation . . . . .	85
A.1.2	Magnetic electrodes . . . . .	85
A.1.3	Contact pads . . . . .	87
A.1.4	Organic layers . . . . .	87
A.1.5	Gate etching . . . . .	88
A.1.6	Organic etching . . . . .	89
A.2	P3HT solution preparation . . . . .	89

# Chapter 1

## Introduction

In this chapter, an introduction will be given into the field of spintronics and the use of organic materials in spintronic applications. Some key subjects will be examined more in-depth in Chapter 2. A description of the fabrication equipment and measurement equipment that is used in this work is given in Chapter 3, while the actual experiments are described in Chapter 4. The results of those experiments are reported and discussed in Chapter 5. Finally, the conclusion and recommendations can be found in Chapter 6.

### 1.1 Spintronics

Ordinary electronic devices such as computer chips use only the inherent charge of an electron to convey information. Spintronics, short for spin-based electronics, aims to use the quantum mechanical property of electron spin as an information carrier. There are many potential advantages to this, such as lower power consumption, reduction of chip volumes and decreased volatility without sacrificing performance.

Spin is a purely quantum mechanical property of particles, which takes the shape of an intrinsic angular momentum<sup>1</sup>. For electrons, the spin can have a value of either  $+\frac{1}{2}\hbar$  or  $-\frac{1}{2}\hbar$ . These are often called spin-up and spin-down. For more information on the basics of spin, see Griffiths[1], Chapter 4.

#### 1.1.1 Ferromagnetism

In an ordinary non-magnetic metal, the electronic structure of the metal is not dependent on the spin of the electrons. Such a case is shown for face-centered cubic (fcc) copper (Cu) in Figure 1.1(a). However, in a magnetic metal, each unit cell has a net spin. These spins tend to align due to exchange interaction. In this case, the electronic structure of the metal is spin-dependent, with one spin sub-band having more energy than the other due to exchange-splitting. This results in a shift of the DOS, and thus a different majority and minority spin population. See for example the case of hexagonal close-packed (hcp) cobalt (Co) in Figure 1.1(b). In this case, the majority population is spin-up, while the minority population is spin-down. This is in contrast to the spin population at the Fermi level, where more electrons are spin-down. However, due to the exact character of the bands contributing to the DOS at the Fermi level, these spin-down electrons are heavier and do not contribute as much to transport effects. This is further complicated by the existence of interface effects, and the interplay between the cobalt and any other material in contact with it. These effects are more thoroughly discussed in Section 2.3.

---

<sup>1</sup> However, you cannot describe this as a classical model where the particle spins around some axis. Doing so for electrons will result in rotation speeds much larger than the speed of light.

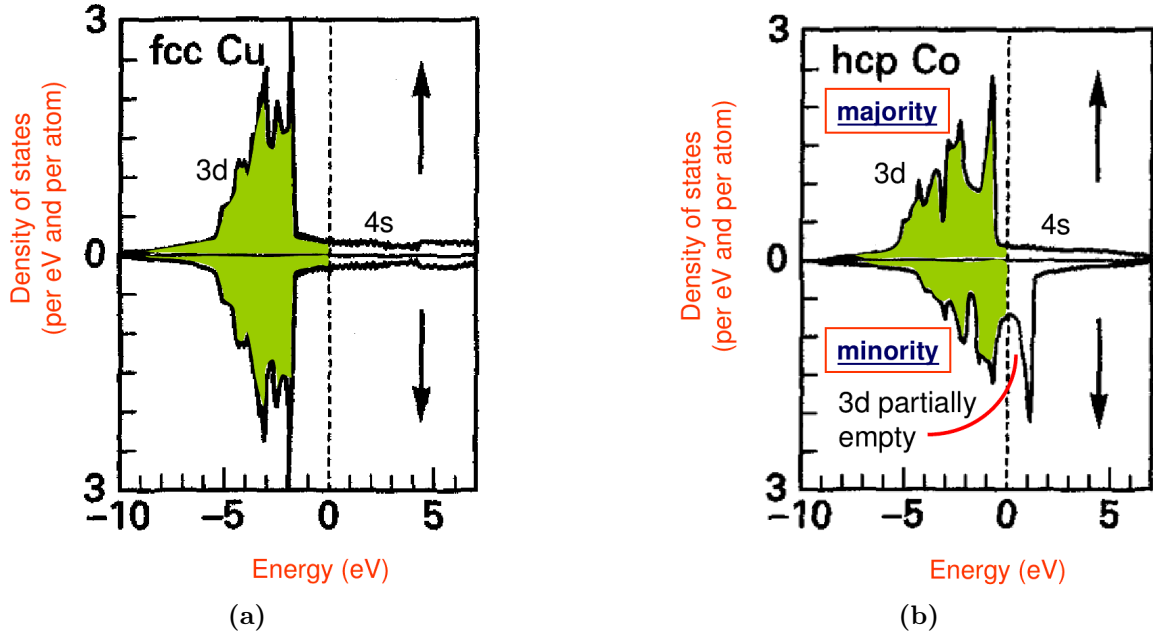


**Figure 1.1** – (a) is the spin-separated DOS for fcc Cu. The Fermi level is indicated by the dotted line. The top graph (spin up) and the bottom graph (spin down) are identical, indicating a complete lack of spin polarisation in this case. (b) For hcp Co, the DOS is spin-dependent. This results in a majority spin-up population and a minority spin-down population. Note that majority and minority refer to the total electron population, and not to the DOS at the Fermi level. [2]

Since by far the largest contribution to any transport phenomena is caused by electrons at or near the Fermi level, the notion of minority and majority spin is not always useful to describe spin phenomena. A natural way to mathematically define the spin polarisation (SP) is:

$$SP = \frac{N_{\uparrow} - N_{\downarrow}}{N_{\uparrow} + N_{\downarrow}} \quad (1.1)$$

where  $N_{\uparrow(\downarrow)}$  is the DOS of the spin population at the Fermi level[3]. However, this does not take into account any other effects that influence the current, such as the effective mass of the electrons at the Fermi level.

Although ferromagnetic metals exhibit a non-zero spin polarisation, this is only strictly true for single magnetic domains of such materials. In the demagnetised case, there are many domains which have arbitrary orientation, resulting in a net zero spin polarisation. However, by applying a large enough magnetic field (i.e. a field well above the coercive field  $H_c$  of the ferromagnet), these magnetic domains can be aligned, resulting in a net spin polarisation throughout the material.

Magnetoresistance (MR) is the term used to describe the change in resistance of a structure of thin ferromagnetic materials separated by a non-magnetic material. The non-magnetic material is used to decouple the magnetic layers, such that their magnetisation can be switched independently. MR is a function of the relative magnetic orientations. Such an effect was already measured by Lord Kelvin in 1851 for single magnetic materials, now called anisotropic magnetoresistance (AMR). The first experimental results involving magnetic multilayers have been confirmed in the 1960s, but the first practically useful effect was only discovered in 1988 independently by Albert Fert and Peter Grünberg. They discovered the effect of giant magnetoresistance (GMR) in structures of multilayers of Fe and Cr, and measured MR values of up to 80% between the case of anti-parallel magnetic alignment and parallel magnetic alignment. The

Nobel Prize in Physics 2007 was awarded to them for this discovery. In general, MR is defined as:

$$MR = \frac{R_{AP} - R_P}{R_P} \quad (1.2)$$

Thus, a positive MR is defined as a lower resistance in the parallel configuration compared to the anti-parallel configuration.

### Giant magnetoresistance

The most-often used explanation for GMR is the two-current model, developed by sir N.F. Mott[2]. As shown in Figure 1.1(b), ferromagnetic metals have a spin polarisation. Although Figure 1.1(b) seems to suggest that a current through a ferromagnet is mostly minority-polarised, it is actually the other way around. The 3d-band crosses the Fermi level for minority-polarised electrons. Thus, there are many states available to scatter into, both for 3d-character minority electrons and for 4s-character minority electrons. On the other hand, there are no majority-polarised 3d-states available, and spin-flip scattering is rare. Thus, the majority-polarised electrons have few possibilities for scattering, and experience a lower resistance in the ferromagnet compared to the minority-polarised electrons. The net result of this is that the current through a ferromagnet is majority-polarised.

To measure a GMR structure, a current is sourced in-plane through the layers. This current is spin-polarised according to the local magnetic orientation, with the majority spin having a lower resistance than the minority spin. If the metallic layer in between the ferromagnetic layers is thin enough, the electrons can also scatter completely through this layer, rather than just scatter within the ferromagnetic layer. This is shown in Figure 1.2. When both ferromagnetic layers are aligned parallel, the majority spin population in one layer ("spin-right" in Figure 1.2) will also be the majority spin population in the other layer. Equally, the minority spin population in one will also be the minority spin population in the other. The two-current model hinges on the assumption that there are few scattering processes that will flip the electron spin state. Then, the total current can be modelled as a sum of the majority current and the minority current. The final result is a much lower resistance of the GMR stack for parallel alignment of the ferromagnetic layers, when compared to anti-parallel alignment of the ferromagnetic layers. The GMR can also be measured when a current is sourced perpendicular through the layers. In that case, the effect is mostly due to spin-dependent scattering at the interfaces of the magnetic and non-magnetic metals.

GMR was the first spintronic effect to have found practical use outside of a laboratory. It is predominantly used in read heads for magnetic storage drives, which are found in nearly every computer nowadays. Such use allows the read heads to be much smaller than previously, requiring less power to operate and increasing the amount of data that can be stored on a hard disk. Further applications of such effects could be magnetic random access memories, which are non-volatile and radiation-resistant alternatives for use in computer memory.

### Tunneling magnetoresistance

The second major effect that contributed to the field of spintronics is tunneling magnetoresistance (TMR). The major difference between GMR and TMR is that the spacer layer in TMR experiments is an insulator or semiconductor instead of a non-magnetic metal. While the physics dictating GMR is predominantly the spin-dependent scattering of electrons, in TMR this effect is of no significance, and the MR values are solely due to spin-dependent tunneling phenomena across the non-magnetic layer. Tunneling is a purely quantum mechanical process which occurs because the wave function of electrons has a non-zero value immediately outside the metal, as

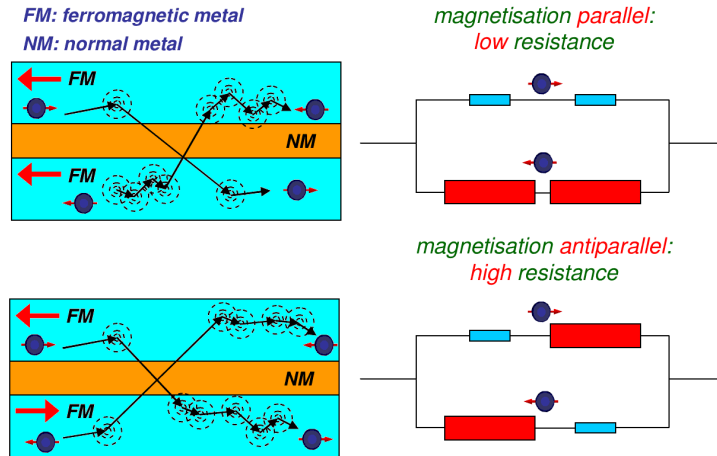


**Figure 1.2** – A schematic view of the scattering process in GMR, and the resistances experienced by the two currents in the parallel and anti-parallel alignment cases. [2]

shown in Figure 1.3. Thus, if the barrier is suitably thin, an electron can go through, even though it has a lower energy than the barrier height itself.

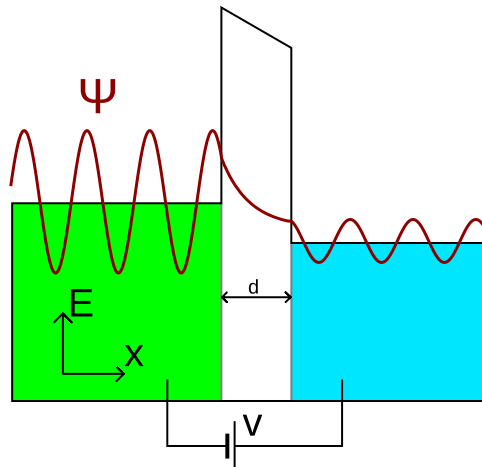


**Figure 1.3** – Schematic of quantum mechanical tunneling across a barrier. An electron that starts out in the left electrode with a wave function  $\Psi$  has a non-zero chance to end up in the right electrode. The energy is sketched on the y-axis,  $x$  is the horizontal distance,  $d$  is the thickness of the tunnel barrier, and  $V$  is the potential applied between the left and right electrodes.

In the simplest TMR case, any interface effects and barrier effects on the spin-dependent tunneling current are ignored. In a laboratory experiment, a vacuum barrier can be used to achieve this. Experiments show that even surface effects are minor in such a set-up[4,5]. The conductance can then be written in what is known as Julliere's model[6], which assumes that spin is conserved during the tunneling process. This results in a two-current model very similar to the one used to evaluate GMR. When both electrodes are magnetised parallel, the majority spin electrons will tunnel into the majority states, and minority spin electrons will tunnel into minority states, resulting in a large conductance as shown in Figure 1.4(a). However, when the electrodes are magnetised anti-parallel, the majority spin electrons in one electrode can only go to minority states of the other electrode, resulting in a much lower conductance, see Figure 1.4(b). In many cases, the effect of the barrier material and interface between the ferro-

magnet and insulator cannot be ignored[7,8], and the barrier material can radically influence the spin-dependence of the tunneling current[9]. This will be explored in more detail in Chapter 2.

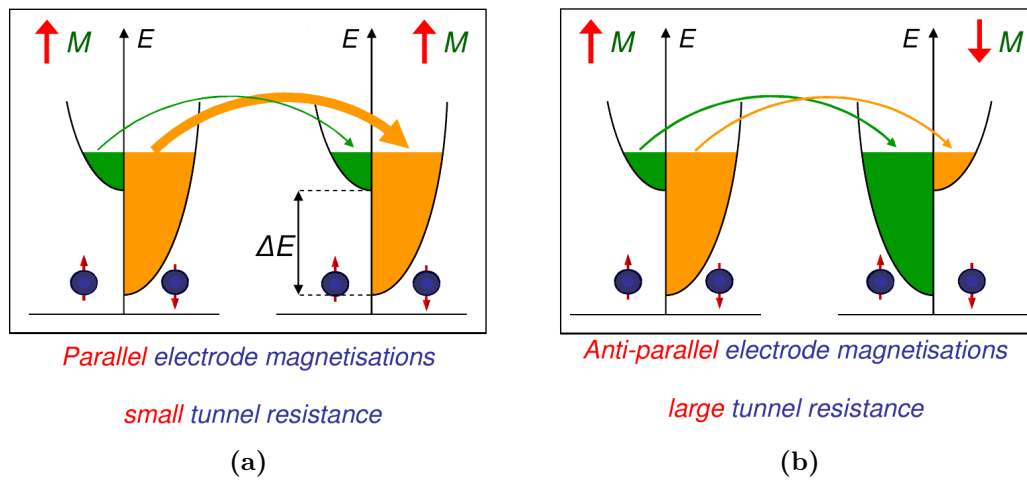


**Figure 1.4** – In a TMR experiment, (a) shows the situation where the electrodes are magnetised parallel to each other. (b) occurs when the electrodes are magnetised anti-parallel. [2]

## Coercivity

It is critical for any MR application that the magnetisation of each ferromagnetic layer can be switched independently. Every magnetic material has a specific hysteresis loop, as shown in Figure 1.5(a). A ferromagnetic material will align itself to the external magnetic field if that field is strong enough. In that case, it is in the saturation magnetisation regime, where the magnetisation of the material cannot be increased further. If the external field is turned off, a remnant magnetisation will typically remain. When the magnetising field is switched into the opposite direction, the ferromagnetic layer will not immediately follow. It takes a specific coercive field before the ferromagnetic layer will suddenly switch its internal magnetisation to align with the external field. This coercive field, or coercivity, is specific for the material and geometry. A 'hard' ferromagnetic material is one that has a large coercivity. It will not easily change its own magnetisation to align with an external field. In contrast, a 'soft' ferromagnetic material has a small coercivity, and easily changes its magnetisation in response to an external field.

By making a TMR stack out of two different ferromagnetic layers with different coercivities, control can be obtained over the type of alignment of the two layers (parallel or anti-parallel). When starting at a large negative H-field, both materials will be aligned parallel. However, the soft ferromagnetic layer will switch almost immediately after the H-field turns positive, while the hard ferromagnet will not yet switch. Thus, there's a region where the alignment is anti-parallel. Only when the H-field further increases beyond the coercive field of the hard ferromagnet, will the alignment be parallel again. Thus, when sweeping the magnetising field from negative to positive and back to negative, the resistance behaves as shown in Figure 1.5(b).

Another viable way to achieve the required differences in the hysteresis loop is by biasing one of the ferromagnetic layers using an anti-ferromagnetic layer on top[2]. Uncompensated spins at the AFM/FM interface impose a net exchange bias on the ferromagnetic layer, shifting its hysteresis loop. This enables the anti-parallel alignment case even when the two ferromagnetic layers have the same coercivity. Due to the stability of this method, it is more often used in practical applications compared to having two different ferromagnetic materials.

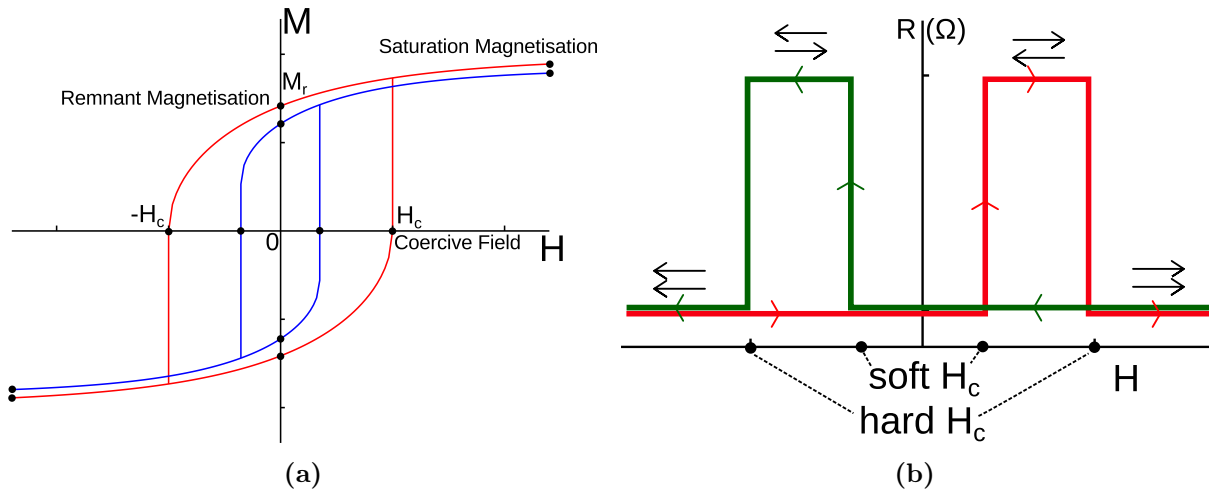


**Figure 1.5** – (a) shows two basic hysteresis loops for a ferromagnetic material. The width of the loop determines the coercivity, and thus the ease with which the magnetisation can be switched. The blue loop shows a so-called soft ferromagnet, and the red loop indicates a so-called hard ferromagnet. (b) shows the behaviour of the MR in a typical magnetising field sweep. The red line shows the MR when the field is swept from negative values to positive values. The green line shows the MR when the field is swept back to negative values.

### 1.1.2 Semiconductor spintronics

The use of semiconductors in spintronic devices has the goal of using the electron spin in addition to its charge for the carriage of information[10]. Nearly all of today’s electronics make extensive use of semiconductors in the transistors that make up their logic circuits, and spintronics has great potential in this field[11]. One example is a spin-based field-effect transistor[12], where the relative magnetisation of the source and drain can be controlled. This adds a memory effect to the transistor, allowing it to double as programmable electronics. Because the contacts maintain their relative magnetisation even without an external field, such a device can have a very low power consumption.

However, there is a rather big practical problem that prevents the creation of a simple spintronic transistor. In the very basic two-current model, the spin-dependent resistance of the ferromagnetic source and drain contacts are much smaller than the spin-independent resistance of the semiconductor, as shown schematically in Figure 1.6. Therefore, the majority current is nearly equal to the minority current. This problem is commonly called the conductivity mismatch[13]. There are three main ways to solve it. The first is to ensure that the ferromagnet resistance is comparable to the semiconductor resistance[14], most often by using semiconducting magnetic materials. The second way is to ensure that there is 100% spin polarisation in the ferromagnet. There are so-called half-metals that have this property. One example is lanthanum strontium manganite ( $\text{La}_{0.7}\text{Sr}_{0.3}\text{MnO}_3$ ) (LSMO)[15]. The third, and easiest, way to solve this is by adding another spin-dependent resistance that is of comparable size to the semiconductor resistance. This is most often accomplished by using a tunnel barrier between the ferromagnet and the semiconductor, since the tunneling current is spin-dependent due to the existence of a majority and minority spin population at the ferromagnet Fermi level[16]. Not only does this solve the conductivity mismatch problem, numerous experiments and theoretical calculations also indicate that the exact nature of the tunnel barrier has a strong influence in the tunneling characteristics[5,9]. Thus, many aspects of a spintronic device can be tweaked by proper choice of materials and precise growth mechanism of the tunnel barrier. This will be investigated in more detail in Section 2.3.

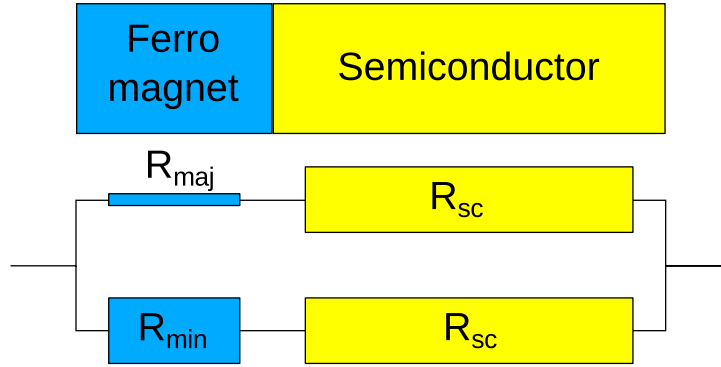


**Figure 1.6** – A simple two-current view of spin injection into a semiconductor. Because the semiconductor resistance is spin-independent and much larger than the ferromagnet resistance, there is hardly any difference in conductance for majority spin electrons when compared to minority spin electrons. This is known as the conductivity mismatch problem.

A quintessential proposed spintronic device incorporating semiconductors is a spin-based field-effect transistor. Such a device was already proposed in 1990[12]. For the proper working of a spin field-effect transistor, it is essential to have strict control over the spin transport properties inside the semiconductor, and over the spin injection and detection process. Every material has a characteristic spin relaxation rate  $T_1$  and spin decoherence rate  $T_2$ , further explained in Section 2.3. In the presence of a magnetic field, every spin also has a Larmor frequency, which is the frequency of precession of the spin around the external magnetic field. By varying the external magnetic field, the Larmor frequency can be varied relative to the material-dependent spin relaxation rate. These two combine to an effective spin lifetime, and can thus be used to control the spin polarisation in a semiconductor.

The spin accumulation in a material is defined as the energetic splitting between the majority and the minority spin populations. This splitting of the chemical potential is caused by the spin polarisation of the injected carriers. Although spin polarisation and spin relaxation are difficult to measure, spin accumulation can be measured by a simple voltage measurement across the tunnel barrier between the ferromagnetic electrode and the semiconductor. By correlating the Larmor frequency with the spin-dependent chemical potential inside the semiconductor, the spin relaxation (and spin lifetime) value can be determined[17]. Such a measurement is called a Hanle measurement, and is explained in more detail in Section 1.3.1 and Section 2.5. It is often difficult to determine if the measured signal originates from the spin or from some other magnetic effect. The use of a very thin ytterbium layer has been shown to reduce the spin signal, allowing the determination of the size of other effects relative to the spin accumulation effect[18].

## 1.2 Organic semiconductors

A certain class of semiconductor materials are organic semiconductors. Unlike the group IV or group III-V semiconductors, these are molecular or polymeric materials composed mainly of light elements such as hydrogen, carbon, nitrogen, and sulfur atoms. Their advantages are low cost, room-temperature processing, potential in making very small (single-molecule) transistors[19], compatibility with flexible substrates[20], and useful optical properties. Typical examples of their use include commercial organic light emitting diodes[21,22] for current and next-generation displays, and organic photovoltaics for photoelectrical energy conversion.

### 1.2.1 Molecular orbitals

For organic materials, the molecular orbitals are strongly determined by the atomic orbitals of carbon, which is the backbone of such materials. Often, organic molecules are planar in nature, leading to  $sp^2$ -hybridisation that contributes to the internal bonds. Such bonds are called  $\sigma$ -bonds. The remaining  $p_z$ -orbitals combine to form  $\pi$ -orbitals, and are usually the highest energy filled molecular orbitals. Thus, these are the electronic states most involved in transport properties. In the simple case of ethylene ( $C_2H_4$ ), there are two distinct possibilities for these  $p_z$ -orbitals to combine. The first, so-called bonding state, contains the  $p_z$ -orbitals in-phase, with a lowered energy. The second, so-called anti-bonding state, is composed of the out-of-phase combination, with a higher energy. Since each  $p_z$ -orbital has one electron, the ground state of ethylene puts both electrons in the bonding-orbital, see Figure 1.7. This lower state is called the highest occupied molecular orbital (HOMO), while the anti-bonding state is the lowest unoccupied molecular orbital (LUMO).

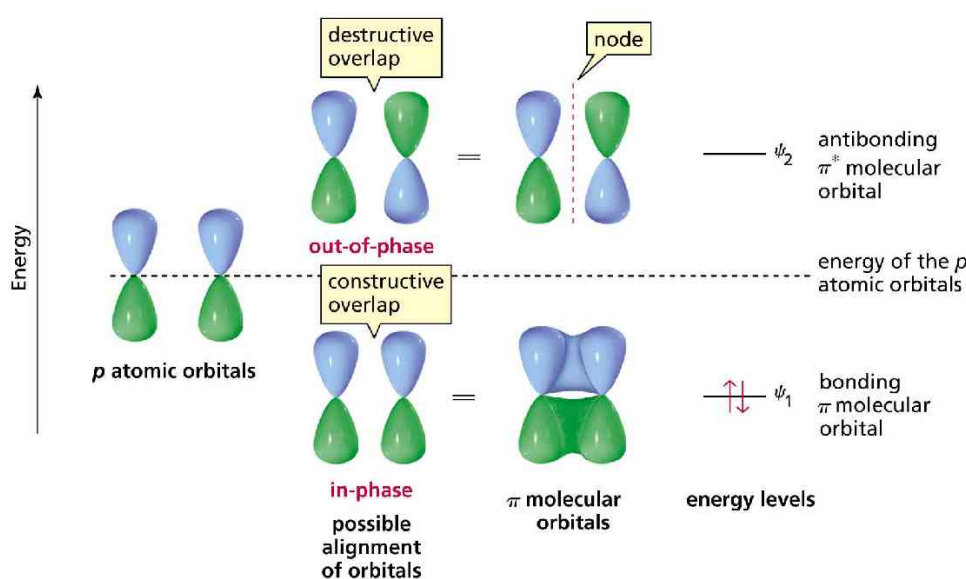


**Figure 1.7** – A schematic diagram showing how two atomic  $p_z$ -orbitals can combine. One combination leads to a higher energy (anti-bonding) and the other leads to a lower energy (bonding). [23]

This method of constructing molecular  $\pi$ -orbitals out of atomic  $p_z$ -orbitals can straightforwardly be extended to larger organic molecules. For example, hexatriene gets a set of six distinct energy levels<sup>2</sup> as shown in Figure 1.8. It is clear that the electrons that are most loosely bound to the organic molecule are in orbitals spread out over the entire molecule. In the case of organic polymers, this can result in highly delocalised electrons contributing to the conductance, even when taking into account that the effective conjugation length is almost always less than the chain length, due to torsion of the molecular chain.

### 1.2.2 Charge transport

In general, the  $\pi$ -bond between two carbon atoms can be of bonding or anti-bonding character. The bonding character has no node in the orbital, and the anti-bonding character does have a node. Thus, electrons tend to gather at bonding sites and stay away from anti-bonding sites. The net effect is that the electrons will change the geometry of the organic molecule away from a

<sup>2</sup> As long as we ignore second-order effects such as fine structure.

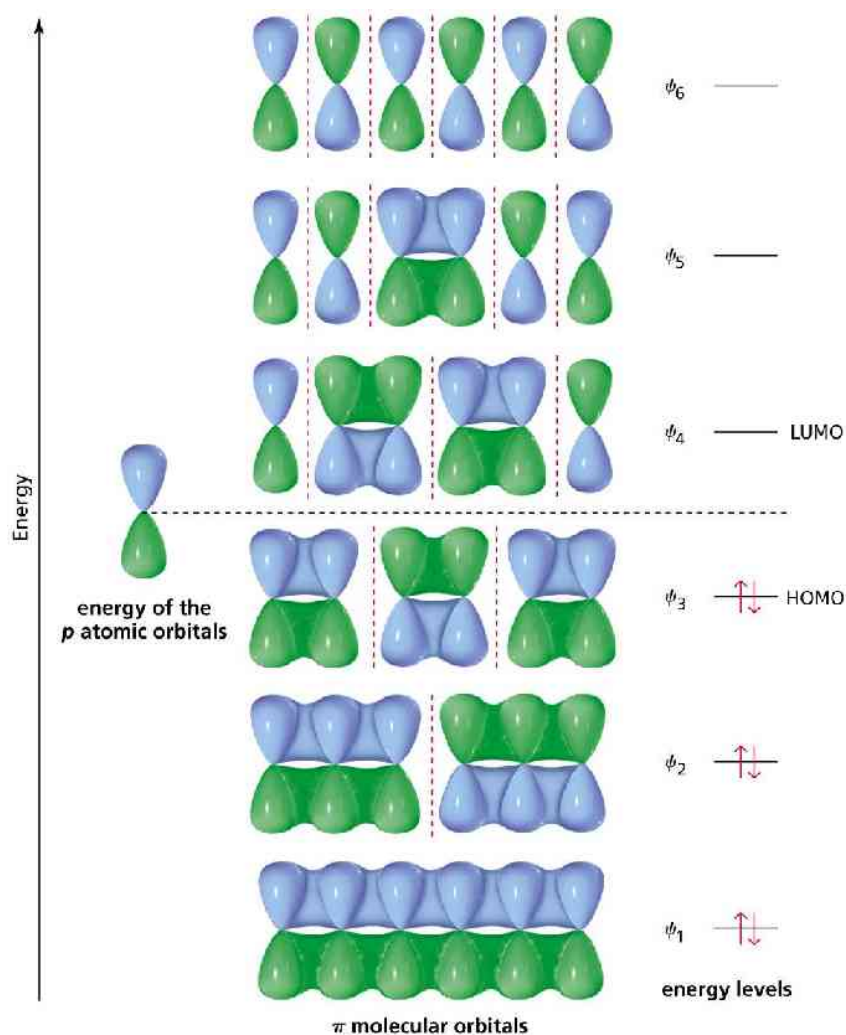


**Figure 1.8** – The energy levels of hexatriene, together with their occupation in the ground state. [23]

perfect situation where all bonds have the same length. In the case of simple linear hydrocarbons, this results in alternately long and short bonds, such that the HOMO has bonding character on the short bonds, and anti-bonding character on the long bonds, resulting in a lowered HOMO energy. This mechanism is the same as seen in Peierls distortion of 1-D atomic lattices.

Although the HOMO and LUMO levels of a single organic molecule are sharply defined, this is not the case for the bulk material. This broadening of the energy levels occurs for multiple reasons. For polymers, the main reason is the variations in HOMO and LUMO energies in each individual piece of the material, mostly due to different lengths of the chains. Also of importance is the variation in the strength of interaction between different parts of the organic material, both for polymers and for single-molecule materials. This is called inhomogeneous broadening. These variations lead to a broadening of the HOMO and LUMO energy levels, which is most often described as a Gaussian distribution with a standard deviation on the order of 50-100 meV[24].

Electron transport in organic semiconductors happens because of overlap of the molecular orbitals. Because of their strong overlap, the occupied  $\sigma$ -orbitals are much lower in energy than the  $\pi$ -orbitals. Thus, the  $\pi$ -orbitals form the HOMO and LUMO energies, and these contribute most to electron transport. The amount of overlap that these orbitals have with

orbitals of neighbouring molecules is crucial to the details of the electron transport, and differs significantly between different organic molecules, different packing configurations and different temperatures. This is further explained in Section 2.1.

### 1.2.3 Spintronics using organic materials

Just like normal semiconductors, organic semiconductors can be used in novel spintronic applications. There are some very appealing potential advantages to this approach. In normal semiconductors, spin-orbit coupling between the electrons and the lattice atoms plays a major role in spin relaxation and spin decoherence. However, since organic semiconductors are mostly composed of the light elements hydrogen and carbon, the spin-orbit coupling is expected to be small[25], since it scales with the fourth power of the atomic number  $Z$ [26]. This should considerably improve the spin relaxation rate. Values of 10  $\mu\text{s}$  have been measured optically[27], multiple orders of magnitude higher than similar measurements in inorganic semiconductors.

A second effect that influences spin relaxation is the hyperfine interaction. In the widely used inorganic semiconductor silicon (Si), this effect is not significant. Especially since silicon has zero nuclear spin for 95% of its stable isotopes ( $^{28}\text{Si}$  and  $^{30}\text{Si}$ )<sup>3</sup>. Although this is also the case for organic semiconductors, where the most abundant carbon-isotope ( $^{12}\text{C}$ ) has zero nuclear spin, hyperfine interactions are still among the dominant spin relaxation mechanism in organic semiconductors[28,29]. This has three reasons: First of all, the relative weakness of spin-orbit coupling in organic semiconductors automatically increase the significance of other effects. Secondly, carbon atoms only make up part of the nuclei of the organic semiconductor. Of the other nuclei, hydrogen is most abundant and has a nuclear spin of  $\frac{1}{2}\hbar$ . Thirdly, electrons are often highly delocalised in inorganic semiconductors, with their wave functions being spread out over  $10^5$ - $10^6$  atoms. This will average out the effects of the hyperfine field, reducing the net interaction. By contrast, electrons in organic semiconductors can be very localised, especially if transport occurs in the hopping regime. In that case, the hyperfine field is averaged over only a few tens or hundreds of atoms, increasing the effective interaction. Of course, all these problems are negated if an isotopically purified carbon material is used, such as graphene or carbon nanotubes[30]. Another major advantage of using organic semiconductors in spintronic applications is the wide array of possible molecules to use. Many different materials have been tried, such as  $\text{C}_{60}$ [31,32],  $\text{Alq}_3$ [33], poly(3-hexylthiophene) (P3HT)[34], and many others[35].

As with inorganic semiconductors, interface effects are also very important in organic semiconductors. Given the even greater mismatch in conductivity compared to ferromagnetic/semiconductor structures, it is vital to find a good solution. In the work done during this master thesis, a tunnel barrier is used to provide a spin-dependent resistance of equal magnitude to the resistance in the organic semiconductor. For this, aluminium oxide ( $\text{AlO}_x$ ) is used on top of a cobalt ferromagnetic layer. It is possible to use magnetic molecules directly on a ferromagnet, but especially in that case, interface effects are of paramount importance[36]. Previous experiments using  $\text{C}_{60}$  show a critical organic layer thickness of 12 nm, above which the MR completely disappeared, attributed to boundary effects between disordered bulk and small ordered grains of  $\text{C}_{60}$ [37], since hyperfine interactions are small in purely carbon-based molecules.

A big problem is the lack of useful methods to directly image the spin polarisation in organic semiconductors. Optical techniques often don't work[38], and the MR may be prone to artefacts not directly resulting from the use of organic semiconductors. Some magnetic methods, such as the spin-induced magneto-optic Kerr effect, are also not useful in organic spintronics, owing to

---

<sup>3</sup> Hyperfine interaction in inorganic semiconductors is only significant if the material has a sizeable nuclear spin, such as GaAs (both gallium and arsenic have nuclear spin  $\frac{3}{2}\hbar$  for all stable isotopes), or in confined systems such as quantum dots.

the low spin-orbit coupling in such systems.

### 1.2.4 P3HT

Although there are many different organic semiconducting materials available, this work will focus on using poly(3-hexylthiophene) (P3HT). This conductive polymer consists of a thiophene conjugated backbone, with an hexyl group ( $C_6H_{13}$ ) attached at position 3, as shown in Figure 1.9. At room temperature, this material is a solid. For spin-coating, it is dissolved in 1,2-dichlorobenzene, into which it has a solubility of  $14.7 \text{ mg ml}^{-1}$ [39]. See Chapter 4 and Chapter 5 for more information on how this solvent was selected.

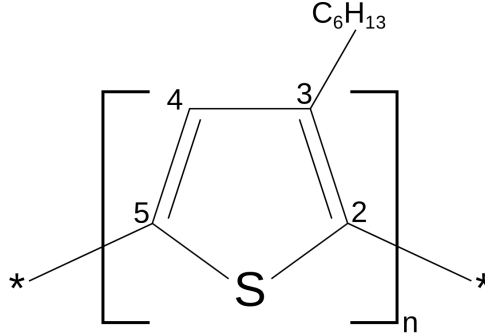


**Figure 1.9** – P3HT is composed of a thiophene polymer backbone with an hexyl group attached to the 3-position of every thiophene ring.

The backbone of P3HT forms long polymer chains, and this combination results in two different types of P3HT polymers due to the way the hexyl groups are attached on each monomer. The first, where the hexyl groups are randomly attached to positions 3 or 4 in Figure 1.9, is called regiorandom (RRa-P3HT). This results in a spaghetti-like layer, where the polymers and hexyl groups have no real ordering. The second type happens when the hexyl groups are all attached to position 3, and this is called regioregular (RR-P3HT). In this case, the polymers form something of a lamellae structure. This ordering means that spin-scattering is less likely in regioregular P3HT, and room temperature MR has been reported for this, whereas it was not detected for regiorandom P3HT[34]. This increased ordering also increases the conductivity of the polymer, improving the spin diffusion length and carrier mobility.

Intrinsic P3HT is an insulator, with a band gap of approximately  $1.6 \text{ eV}$ [34]. The ionisation potential is approximately  $4.6 \text{ eV}$ [40]. In applications, conduction can be induced through doping[41] or gating the material. In this work, gating is used. This has some advantages over doping, mostly a higher controllability and easier manufacturing processes. Actual values of the mobility and conductivity are highly dependent on the structure of the P3HT layer, with values reported between  $10^{-5}$ - $10^{-1} \text{ cm}^2 \text{ V}^{-1} \text{ s}^{-1}$ [42,43]. A spin diffusion length of  $80 \text{ nm}$  has been reported[35]. The spin diffusion length is very dependent on the exact ferromagnetic materials used in the structure, and their interface with the organic material[44]. Furthermore, such values are almost always indirectly estimated from the strength of MR effects as a function of the layer thickness.

The dominant charge carrier is mostly determined by the ease with which electrons or holes can be injected into the material. For P3HT, the ionisation energy is relatively low (it is easy to remove an electron from the material) while the electron affinity is also low (it is difficult to add an electron). This results in p-type dominated conduction through the P3HT. The subject of charge transport in organic materials will be more thoroughly discussed in Section 2.1.

The main reason for using P3HT in this work is the potential for high mobilities[45]. If the

crystalline ordering of the polymer chains is good, there is a great deal of  $\pi$ -orbital overlap. This is likely to yield a high mobility, up to  $0.3 \text{ cm}^2 \text{ V}^{-1} \text{ s}^{-1}$ [46]. Previous measurements using P3HT in a spin-valve structure has yielded a value of 62 nm for the spin coherence length[47]. Again, this value is indirectly estimated from the MR dependence on the thickness, which can be due to multiple effect besides spin relaxation. Despite such experimental work, spin accumulation and detection in organic systems has not yet been experimentally realised, and the details on how spintronic applications work in such materials are still largely unknown. Thus, there is much to be learned from using this material.

### 1.2.5 Organic field-effect transistor

The field-effect transistor was first invented in 1947 by William Shockley, and the more historically significant metal-oxide-semiconductor field-effect transistor was first invented in 1960 by Dawon Kahng and Martin Atalla. A field-effect transistor allows control over the current that flows from the source to the drain by applying a voltage to the gate contact. For details on this process, see Section 2.2.

In the fabrication of field-effect transistors, there are four geometries that are often used, see Figure 1.10. Each of these geometries have advantages and disadvantages, both in the fabrication process and in device characteristics. For this work, a bottom-contacted device is used. The main reason for this choice is the requirement of well-defined magnetic contacts covered with a tunnel barrier, combined with the difficulty of getting a sharp metal/organic interface when depositing metal on top of an organic material.

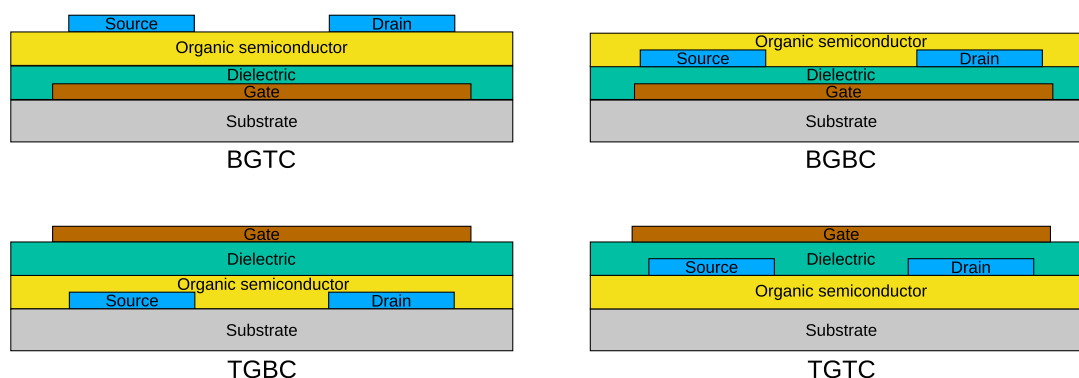


**Figure 1.10** – The geometries which are often used for field-effect transistors are, from top left clockwise: bottom-gated top-contacted; bottom-gated bottom-contacted; top-gated top-contacted; and top-gated bottom-contacted. Image adapted from Figure 2.1 of [48].

Both bottom-contacted geometries were used in this work. The bottom-gated geometry is especially simple to produce, since the substrate can double as the gate electrode if a properly doped semiconductor substrate with a thermal oxidation layer is picked, see Chapter 4. Such a device is called a back-gated O-FET device in this work. The top-gated geometry is more laborious in fabrication, requiring extra deposition of the dielectric layer, patterning of the gate, and an organic etching step to uncover the contact pads to the bottom electrodes. However, it moves the conduction channel of the device to the organic semiconductor/dielectric interface, rather than placing it at the substrate/organic semiconductor interface. For spin injection purposes, this geometry is expected to yield better results, since the spin-polarised current is predominantly injected through the well-defined top of the electrode, rather than through the poorly defined sides.

## 1.3 Spin measurement methods

There are many techniques for measuring spin properties of magnetic and non-magnetic materials. One of these techniques is electron spin resonance. When using electron spin resonance, a magnetic field is applied to a material, and the unpaired spins inside the material are excited by electromagnetic energy. Since the unpaired electrons have two energy levels due to Zeeman splitting, the absorption spectrum yields information about these energy levels. The details of these signals yield information about the interaction of the spin with the local environment. A related technique is muon spin resonance, where spin-polarised muons are injected into a material[49,50]. However, this requires a large muon production facility, increasing the practical difficulty of such experiments.

Optically, photons can be used to determine or alter the spin polarisation state of an ensemble of electrons. By carefully controlling the frequency of the input photons, and measuring the frequency and origin of the output, the available energetic states for spin-polarised electrons can be determined, for example using a two-photon photoemission experiment[33,51].

### 1.3.1 Magneto-transport methods

Purely electrical methods also exist to determine properties of spin-polarised systems. One of the easiest is the MR itself, since its existence is a simple way to determine if a current is spin-polarised. However, for direct measurements of spin coherence lengths, this method is not very suitable, since the decay of the MR with thickness is not only dependent on the spin coherence length. Furthermore, MR can be caused by other effects, such as local Hall effects in the stray fields of the contacts or Lorentz MR.

Additionally, by injecting a spin-polarised current into a material and measuring the voltage drop across a nearby ferromagnetic electrode that has no current flow through it, the difference in chemical potential of the spin-up and spin-down currents can be determined. By using a magnetic field, the spin polarisation can be predictably lowered, with an equivalent lowering of the chemical potential difference. Thus, the spin lifetime can be determined, as it will be related to the Larmor frequency of the magnetic field that is used. Such a measurement is called a Hanle measurement. For more information, see Section 2.5. Although these measurements have been done to determine spin lifetime in both silicon[17] and gallium-arsenide[52], such measurements have not yet been done for organic semiconductors. Furthermore, doubts exist as to the precise origin of this signal in three-terminal Hanle experiments[53], since the current injecting electrode has also been used as the voltage measurement electrode in these experiments.

Another method to measure the spin polarisation of a current is Tedrow-Meservey spin polarised tunneling[54]. For this technique, a superconducting contact is used. When a strong magnetic field is applied, Zeeman splitting shifts the DOS sub-bands for majority and minority spin in the superconductor. If spin-relaxation processes are not present, the occupation level of each sub-band in the superconductor will reflect the spin polarised tunneling current. This can be determined by measuring the differential conductance across the tunnel barrier, see Figure 1.11. By measuring the relative heights of peaks  $\sigma_1$  through  $\sigma_4$ , the spin polarisation can be determined. Often, aluminium thin-film layers are used as the superconducting contact in this technique. Aluminium is a prime choice because of weak spin-orbit coupling, low cost, and it is compatible with  $\text{AlO}_x$ , which is often used as the tunnel barrier material.

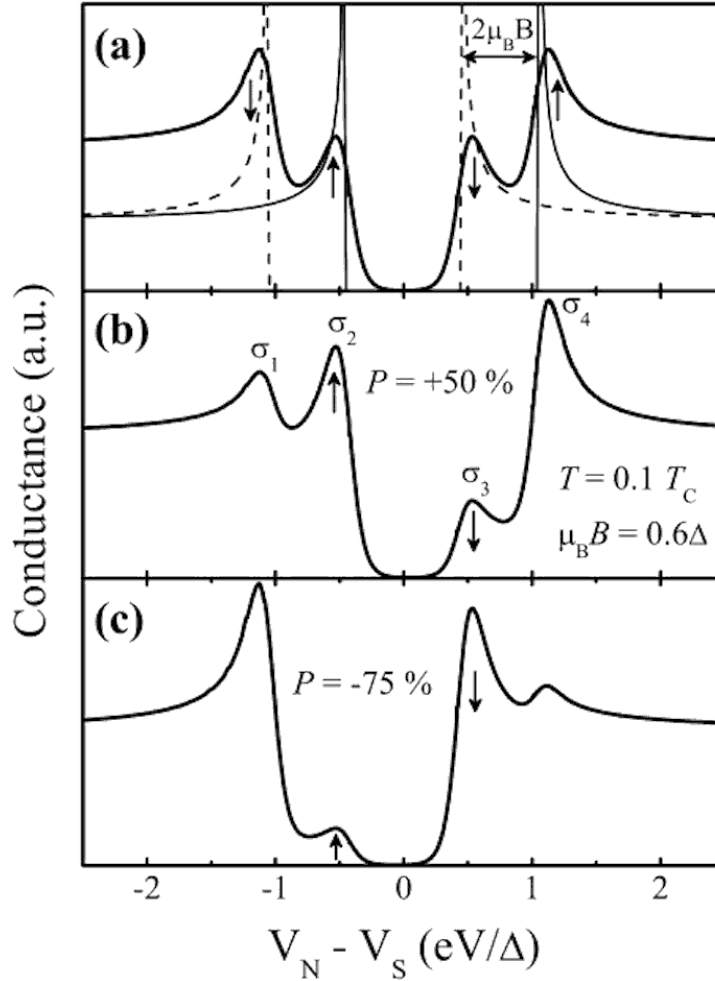


**Figure 1.11** – (a) shows the Zeeman-split conductance of a ferromagnetic/insulator/superconductor junction, where the tunnel current is not spin polarised. The thin solid and dashed lines show the spin-up and spin-down contributions to this conductance respectively. (b) shows the case of 50% spin-up polarisation, while (c) shows 75% spin-down polarisation. [55]

## 1.4 Motivation

Organic spintronics is a relatively young field. It holds many promises for novel applications, as well as improving on existing applications. Using organic materials holds the additional promise of lowering the cost of such devices, as well as adding flexibility to the mix of possibilities. These materials are also predicted to have a very long spin coherence time, due to low spin-orbit coupling and low hyperfine interactions. However, many properties of such materials are not yet thoroughly understood. The advancement of the field of organic spintronics thus hinges on developing a fundamental understanding of spin behaviour in all kinds of organic materials. Only when the basics are understood, can practical applications be effectively developed.

One of these properties is spin lifetime. It has been measured both optically and electrically in inorganic semiconductors, although the electrical measurements based on the Hanle effect are still controversial in their exact interpretation[53]. In organic semiconductors, measurement of spin lifetime is much more difficult, since most methods make use of the spin-orbit interaction present in inorganic semiconductors. Since this interaction is especially low for organic materials, other methods of measuring spin lifetime must be developed. In addition to optical methods,

muon spin resonance is also used, but require large experimental setups[50]. Thus, the goal of this work, to develop a method to measure spin lifetime in an organic semiconductor by electrical means, is very much relevant. It will allow comparison of the optical values obtained through totally different means, as well as increase our understanding of such systems and the interpretation of the data gained through these measurements.

This work strives to reach that goal by first developing a transistor based on the organic material poly(3-hexylthiophene). Since photolithography will be employed in its fabrication, it is unlikely that accurate spin lifetime measurements can be obtained, due to the inherent tunnel barrier influence in three-terminal configurations. However, the fabrication of this device will develop the practical knowledge to create high-quality electronic structures using this organic semiconductor, which should smooth the way for creation of a four-terminal configuration by electron-beam lithography which is to be used in measuring spin lifetime.



# Chapter 2

## Theory

### 2.1 Charge transport in organic materials

As is already explained in Section 1.2.2, organic molecules exhibit HOMO and LUMO levels. If an extra electron is added to the organic molecule as charge carrier, it must necessarily go in the LUMO. For a  $\pi$ -conjugated molecule, the LUMO has exactly one extra node compared to the HOMO. Thus, it has anti-bonding character exactly where the HOMO has bonding character, and vice versa. This extra electron will push apart the short bonds, since it has anti-bonding character there, and pull together the long bonds, since it has bonding character there. Thus, the addition of an electron to an organic molecule will induce geometrical relaxation to accommodate it. This process can be quantified in the reorganisation energy, which is the energy required to change the molecule in order to best accommodate the new electron. This energy is usually larger for smaller molecules, since electrons are more localised compared to large molecules. Also important is the time needed for the molecule to change into its new shape. This is of the order of  $10^{-14}$  s, i.e. the timescale of molecular vibrations, which also involve the displacement of the nuclei.

The details of the charge transport process through organic materials is highly dependent on the exact geometry of the material. Especially important is the overlap of  $\pi$ -orbitals between neighbouring molecules or polymers. If the overlap of the molecular orbitals is large, electrons will be delocalised across many molecules. This will effectively create an electronic band structure similar to that found in normal semiconductors. The most important parameter for this process is the transfer integral, defined as

$$t = \langle \Psi_1 | H | \Psi_2 \rangle \quad (2.1)$$

where  $\Psi_1$  and  $\Psi_2$  denote the molecular orbitals of neighbouring molecules, and  $H$  describes the local Hamiltonian.

There are two regimes of electron transport in organic semiconductors. The first is the so-called hopping regime. In this regime, an electron is localised on one organic molecule, and has the possibility to hop from there to another organic molecule. This hopping requires the electron to overcome a considerable potential barrier, resulting in a low mobility. The average dwell time of an electron in the hopping regime on a single molecule is longer than the relaxation time, so the molecule will change its geometry, resulting in an additional energy barrier since the geometry must be changed back when the electron leaves. The second regime is the band regime. This happens when the transfer integral (and thus the orbital overlap) is large enough for electrons to be delocalised across many molecules. It is possible to relate the residence time and the band width of the organic semiconductor by using the time/energy uncertainty principle, which gives  $\tau \approx \frac{\hbar}{W}$  where  $\tau$  is the residence time and  $W$  is the full effective band width. This full effective

band width is approximately four times the transfer integral  $t$ . Thus, if the  $\pi$ -orbital overlap is high enough (i.e. the transfer integral is large enough), the residence time of an electron will drop below the relaxation time. Then, the organic molecule does not have time to change its geometry, and band-like electron transport occurs. The typical band width at which this occurs is 0.1-0.2 eV.

Band-like transport in an organic semiconductor is strongly dependent on a high  $\pi$ -orbital overlap. When the temperature of even a highly ordered organic crystal increases, the individual molecules will vibrate relative to each other, reducing the orbital overlap and thus the transfer integral. The result is a switch from band-like transport to hopping transport at increasing temperature, reducing the mobility for organic semiconductors. Besides temperature, there are many other factors which influence the mobility of charge carriers in an organic material, see for example [24].

## 2.2 Organic field-effect transistor

Although no definitive model for the transport inside an organic field-effect transistor has yet been published, review articles are available which explain the workings in detail[56,57,58]. An organic field-effect transistor behaves much the same as a normal thin-film field-effect transistor. It is in essence an interfacial device, where a gate induces an accumulation or depletion region, depending on the polarity of the gate and the dominant charge carrier type of the organic semiconductor. Although high MR values have been demonstrated using n-type organic semiconductors[59], most organic materials, including P3HT, are p-type conductors<sup>4</sup>. Thus, the device is in accumulation mode when the gate voltage is negative. In that case, the HOMO and LUMO levels bend upward at the interface between the organic and the dielectric material, and a 2D charge transport region forms near this interface. This transport region is often only as thick as a single molecular layer. When the gate voltage is positive, the device is in depletion mode, meaning that the charge carriers are pushed away from the interface, and no transport region is created. Normally, a field-effect transistor is operated in a *common source configuration*, where the source is grounded and the gate and drain voltages are defined with respect to the grounded source, see Figure 2.1. Holes, injected at the source electrode in case of a negative drain voltage, move through the transport region to the drain electrode. Because of the existence of low-energy trap sites in the organic semiconductor, a threshold voltage exists. This threshold voltage is the minimum gate voltage required to induce more charge than can be held by the deep trapping sites, and is thus the minimum gate voltage required to guarantee that charges are available for conduction.

The source-drain current is then determined by the gate voltage and by the drain voltage. At a low drain voltage compared to the gate voltage, the device is in the linear regime, where the source-drain current increases linearly with increasing drain voltage. When the source-drain voltage is significantly higher than the source-gate voltage, the charge accumulation channel is destroyed near the drain contact. This results in a saturation of the current, as shown in Figure 2.2. The equations describing the drain current are split into the linear regime and the

---

<sup>4</sup> In the context of organic semiconductors, p-type and n-type are fundamentally different concepts from the same terms as used in normal semiconductors. Here, they refer to the ease with which carriers can be injected, rather than the ease with which already-present carriers can be moved. Thus, it is not only material-dependent, but also electrode- and interface-dependent.

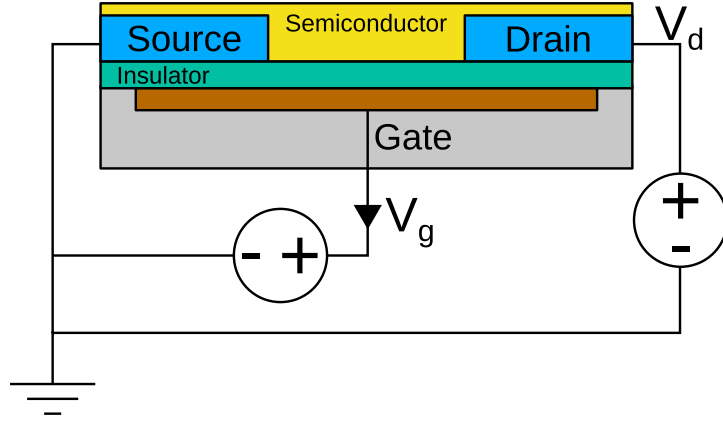


**Figure 2.1** – The conventional wiring of a field-effect transistor during electrical characterisation measurements. This configuration is called a *common source configuration*. Adapted from Figure 2 of [58].

saturation regime.

$$I_D^{lin} = \frac{W}{L} C_i \mu (V_G - V_T) V_D \quad V_D \ll (V_G - V_T) \quad (2.2)$$

$$I_D^{sat} = \frac{W}{2L} C_i \mu (V_G - V_T)^2 \quad V_D > (V_G - V_T) \quad (2.3)$$

When measuring the source-drain current at a fixed high drain voltage while varying the gate voltage, the resulting transfer curve can be used to determine the mobility of the charge carriers in the organic material. By plotting the gate voltage versus the square root of the source-drain current, the mobility and threshold voltage can be determined:

$$\mu = \frac{2L}{WC_i} A^2 \quad (2.4)$$

$$V_T = -\frac{B}{A} \quad (2.5)$$

Here, A is the slope of the linear best-fit and B is the x-axis intercept of that fit[56].

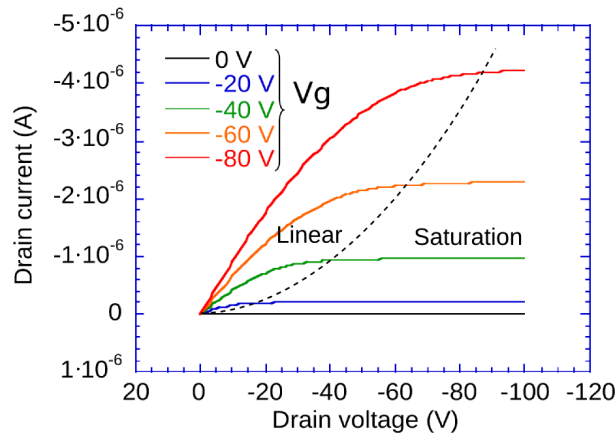


**Figure 2.2** – The IV curves resulting from Equations (2.2) and (2.3). Source: Michel de Jong.

## Space-charge limited current

When the injection of charge carriers into a field-effect transistor is limited by the electrostatic potential of the charge carriers already present in the channel, the behaviour of the device is characterised by a space-charge limited current. In this case, the amount of charge carriers is not constant over the length of the channel, but is larger closer to the injecting electrode. At low voltages and in the absence of traps, the current density can be described as

$$J = \frac{9}{8} \epsilon_0 \epsilon_r \mu \frac{V^2}{L^3} \quad (2.6)$$

as long as diffusion contributions are neglected[24]. In this equation,  $\epsilon_r$  is the dielectric constant of the organic material, and  $L$  is the distance between the electrodes. In an experimental setting, the mobility can be extracted from a fit to Equation (2.6) if the measured current is related to the current density in a well defined way - that is, if the dimensions of the conduction channel are known - and if the dielectric constant of the organic material is known.

## 2.3 Spin transport

The conductivity mismatch problem when attempting spin injection from a ferromagnetic material to a semiconductor or organic semiconductor (explained in Section 1.1.2), can be solved in multiple ways. The method used during this research is the addition of a spin-dependent resistance in the shape of a tunnel barrier. In that case, the two-current model is adjusted to Figure 2.3, and a large difference is observed when the relative alignment of two ferromagnetic layers is changed.

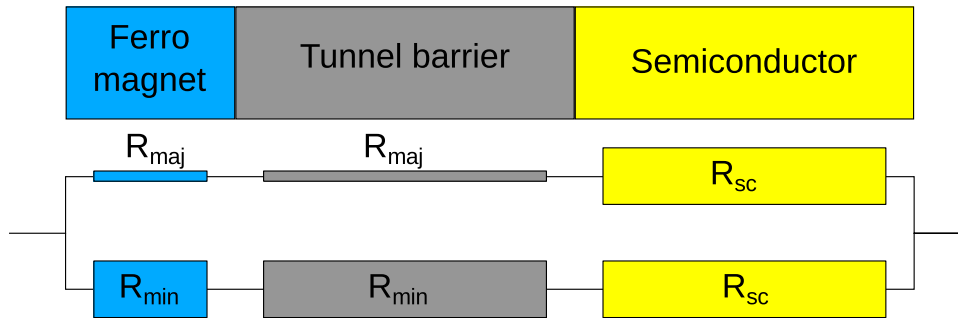


**Figure 2.3** – The conductivity mismatch problem when injecting a current from a metallic contact into a semiconductor can be solved by adding a spin-dependent resistance in the shape of a tunnel barrier to the electrode. If the resistance of this tunnel barrier is of the same order of magnitude as the resistance of the semiconductor, a clear difference in conductance is obtained between majority and minority spin electrons.

Even though a tunnel barrier is not by itself magnetic, the resistance is still spin-dependent, mostly because of interactions at the interface with the spin-dependent DOS of the ferromagnetic layer. Because the DOS of the minority spin is much lower than the DOS of the majority spin, and because the main process by which the current penetrates through the barrier is quantum mechanical tunneling, the rate of tunneling will be much higher for the majority spin than for the minority spin. However, this assumes that the precise energy states available in the barrier do not influence the tunneling process at all. In practice, the details of the DOS of both the ferromagnetic layer and the tunnel barrier can strongly influence the final spin-dependent tunneling behaviour.

As an example, consider an interface between bcc iron (Fe) and magnesium-oxide (MgO)[9]. The band structure of Fe is shown in Figure 2.4(a). In the  $\Delta$ -direction, the  $\Delta_1$  energy band for the majority spin population crosses the Fermi level, which means that these electrons are available for tunneling. However, the same energy band for the minority spin population lies fully above the Fermi level. By itself, this does not make bcc Fe a half-metal, since there are other energy bands for the minority spin population that do cross the Fermi level.

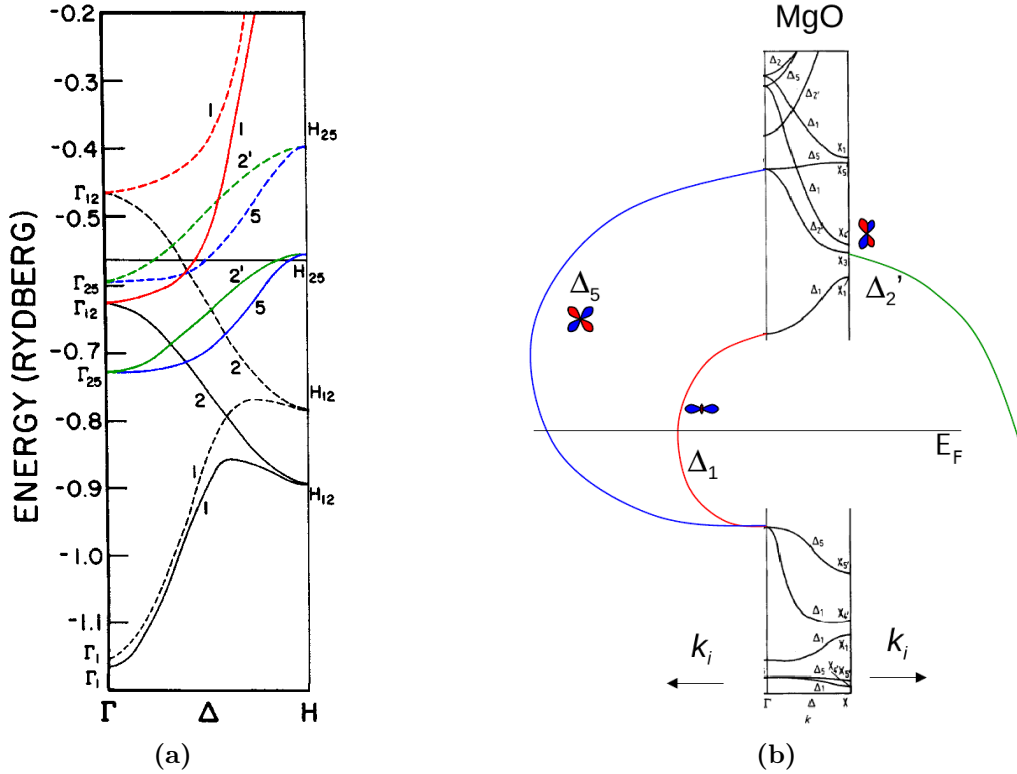


**Figure 2.4** – (a) shows the energy bands for the  $\Delta$  direction in Fe. The solid and dashed lines show the energy bands for majority spin and minority spin respectively. (b) shows the energy bands for MgO in the same direction, in addition to the evanescent states at the band gap. Shown in red is the  $\Delta_1$  energy band, in green the  $\Delta_{2'}$  energy band and in blue the  $\Delta_5$  energy band. The horizontal solid line in both graphs indicate the Fermi level. Sources: (a) is adapted from [60] and (b) is adapted by Michel de Jong from [61].

However, when combining bcc Fe with MgO as a tunnel barrier, this half-metallic behaviour of the  $\Delta_1$  energy band is amplified by the band structure of MgO. Shown in Figure 2.4(b), the MgO layer will dampen the  $\Delta_1$  states much less than the other states in the  $\Delta$ -direction. This is due to the imaginary  $k$ -value of the evanescent states, which is much smaller for the  $\Delta_1$  energy bands than it is for the  $\Delta_{2'}$  and  $\Delta_5$  energy bands. Thus, the  $\Delta_1$  state will be less damped inside the MgO than the  $\Delta_{2'}$  and  $\Delta_5$  states.

The final result is that in addition to the half-metallic behaviour of bcc Fe for the  $\Delta_1$  energy band, the spin-dependence of the tunneling process is further strengthened by the lower dampening of the fully polarised  $\Delta_1$  states, in comparison to the mixed  $\Delta_{2'}$  and  $\Delta_5$  states. It is clear that the details of the DOS of both the ferromagnetic layer and the tunneling layer can contribute significantly to the spin-dependence of the tunnel resistance, and thus to the MR value that can be obtained. Experiments have achieved MR values exceeding 100% using this method[62]. It is possible to change the sign of the MR by proper selection of the tunnel barrier, such that minority electrons have a higher tunneling probability than majority electrons[7].

### 2.3.1 Spin scattering

Spin scattering refers to the process whereby an electron can change its spin state. The decay of the spin state is separated into two parts. The spin relaxation rate  $T_1$  is the longitudinal decay rate, in the direction of the quantisation axis. During spin relaxation, the quantisation axis of the spin of a single electron is changed by scattering interactions. During normal scattering processes, spin is preserved. However, if there is a transfer of angular momentum during scattering, then the spin of the electron can change. The spin decoherence rate  $T_2$  is the transverse decay rate, defined perpendicular to the quantisation axis. Since spin is a quantum mechanical process, it is impossible to know both the quantisation axis and the transverse axis moments. This is typically pictured as a spin which precesses around the quantisation axis. Spin decoherence is the loss of the phase relation between an ensemble of spins which are precessing around the same quantisation axis.

There are several relevant mechanisms by which spin relaxation can occur. The first is the Elliott-Yafet mechanism, which describes the spin mixing of the Bloch states due to spin-orbit interactions. When such spin mixing is present, normal scattering processes can cause spin flipping, and thus spin relaxation. A second process is phonon interaction with the spin states via spin-orbit coupling. Since the spin-orbit interaction is due to the movement of the electron through the electrical field generated by the lattice atoms, lattice movements (phonons) can induce spin relaxation via spin-orbit coupling. Other mechanisms include the D'yakonov-Perel mechanism, which deals with the contributions to the spin-orbit coupling due to inversion asymmetry (further explained below), and the Bir-Aronov-Pikus mechanism, which describes electron-hole exchange scattering of the spins in p-type semiconductors. For further information, see Chapter 3 of [63].

Hyperfine interactions play mostly a role in spin decoherence, although spin relaxation mechanisms also inevitably induce spin decoherence. During hyperfine interactions, the spin of the electron will interact with the nuclear magnetic field, caused by the nuclear spin of the lattice atoms. These interactions will induce spin decoherence by randomising the phase of the spin.

### 2.3.2 Spin-orbit coupling

Spin-orbit coupling is a relativistic effect. Because electrons move through a lattice of atoms at a certain speed, general relativity states that the length of the lattice will contract. This means that the charge density due to the nuclei will increase. Thus, in the rest frame of the electron, it experiences a higher electric field from the nuclei than it would if it were at rest. In the rest frame of the lattice, this is seen as a magnetic interaction term called spin-orbit coupling, also shown in Figure 2.5.

In addition to the normal spin-orbit interactions in a lattice, there are special types of spin-orbit coupling, called Rashba and Dresselhaus spin-orbit coupling. Rashba spin-orbit coupling refers to the coupling between the moving electrons and the electrical field created at an interface between two materials, or at the surface of a metal. Just like in ordinary spin-orbit coupling, the observed density of the charges at the interface from the electron point of view is dependent on the speed of the electron. Since charge accumulation at a dielectric interface is easily controlled by a gate voltage, Rashba spin-orbit coupling can be used to control the effective spin-orbit coupling to the spin-polarised electrons by pure electrical means, without the aid of a magnetic field[64].

The second type is Dresselhaus spin-orbit coupling. This effect originates from a lack of inversion symmetry in the atomic lattice. In general, electrons with the same spin travelling in opposite directions do not have the same energy, unless inversion symmetry is present in the material. If that is present, then  $\epsilon_{k\uparrow} = \epsilon_{-k\uparrow}$ . Inversion symmetry is defined as the operation

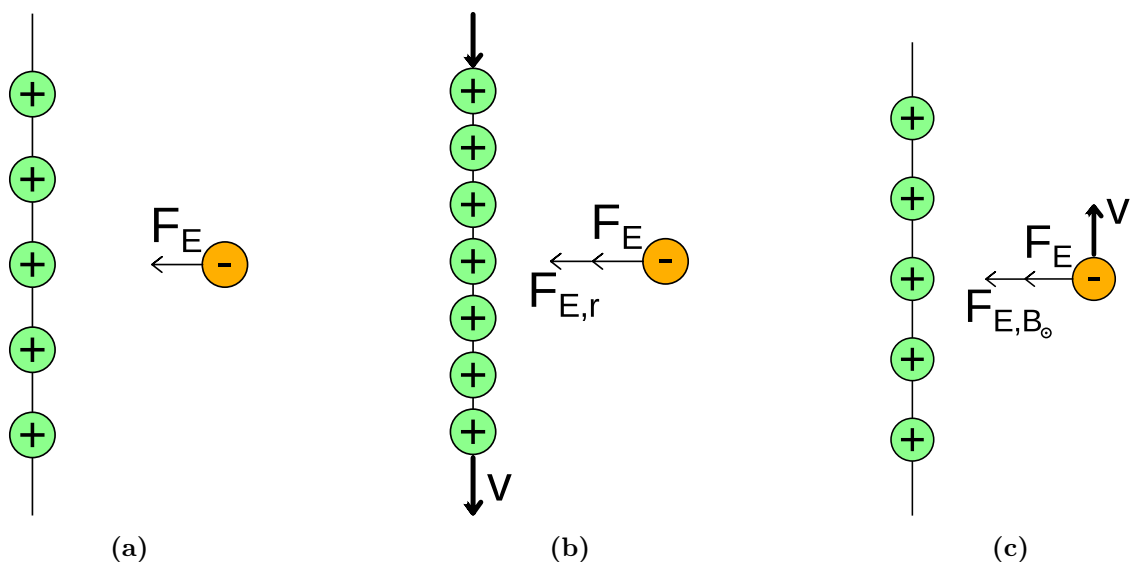


**Figure 2.5** – (a) shows a stationary charge (orange) with a stationary infinite line of nuclei (green). Only an electrical force  $F_E$  acts on the charge due to the electrical field of the nuclei. (b) shows the case where the line of nuclei move relative to the charge, from the point of view of the charge. Due to Lorentz contraction, the density of nuclei increases. This means there is an extra force  $F_{E,r}$  due to relativity that is acting on the particle. (c) shows the same movement, but now from the point of view of the nuclei. The extra force term is still present (no physics has changed), but can now be ascribed to a magnetic field pointing out of the paper.

where every coordinate of an atom with respect to the centre of inversion is multiplied by  $-1$ , but there is no net change in the lattice structure. For example, the crystal structure of NaCl has inversion symmetry. On the other hand, materials which crystallise in the zinc-blende structure such as GaAs do not have inversion symmetry. In that case, the material can be seen as stacks of layers with a small potential step in between, resulting in a spin-orbit coupling term. This spin-orbit coupling term is completely due to the lack of inversion symmetry, and is called Dresselhaus spin-orbit coupling. For a more mathematical approach, see Chapter 2 of [63].

## 2.4 Spin transport in organic materials

Most of the spin relaxation and spin decoherence mechanisms that are important in inorganic semiconductors are no longer applicable to organic semiconductors. The spin-orbit coupling in organic materials is relatively low due to the low atomic mass of the elements in the organic molecules or polymers, as well as due to the low speed of the electrons. Especially in the hopping regime, the electrons tend to stay on one molecular site for a relatively long time, reducing the effect of spin-orbit coupling. However, there is experimental evidence that spin-orbit interactions are still a sizeable source of spin relaxation in certain organic materials[65,66]. This mainly happens during the actual hopping, since electrons can temporarily move relatively fast during that process. Probing this exact process is relatively easy, since the hopping rate is directly related to the temperature of the material[67].

In organic materials, hyperfine interaction is among the dominant mechanisms for spin decoherence[28,29]. Although  $^{12}\text{C}$  has zero nuclear spin,  $^1\text{H}$  does not. It is possible to tune the hyperfine field inside a conjugated polymer by deuteration of the backbone or the side groups[68]. This technique could even allow for the mapping of the charge carrier wave inside such materials.

Spin polarised charge injection from a metallic contact into an organic material is not a

singular process. Rather, it is a combination of multiple processes, such as thermionic charge transfer and tunneling charge transfer through the layer[69,70]. In these injection processes, the interface between the metallic layer and the organic layer is often of paramount importance[33], and this requires careful design of the fabrication process due to significant interdiffusion of metal when deposited on organic materials.

## 2.5 Hanle measurement

As is explained in Section 1.3.1, the Hanle experiment utilises the spin precession of an ensemble of spins in an external magnetic field. Shown schematically in Figure 2.6, a magnetic field  $B_{\perp}$  is oriented perpendicular to the spin injection interface. This causes spin precession, thereby reducing the spin accumulation and lowering the chemical potential difference  $\Delta\mu$  that can be measured across the interface. Since the spins precess in the magnetic field at the Larmor frequency

$$\omega_L = g\mu_B \frac{B}{\hbar} \quad (2.7)$$

the decay of the chemical potential difference is related to this Larmor frequency. This decay follows a Lorentzian shape

$$\Delta\mu(B) = \frac{\Delta\mu(0)}{1 + (\omega_L\tau)^2} \quad (2.8)$$

where  $\tau$  is the spin lifetime of the spin ensemble inside the semiconductor. Thus, by determining the Larmor frequency  $\omega_L$  at half the maximum value (the FWHM) of the resulting curve, the spin lifetime can be calculated as  $\tau = \frac{1}{\omega_L}$ . Due to several approximations which are made, such as the absence of artificial broadening due to stray fields, this approach is likely to yield a lower limit of the spin lifetime. This measurement has been done in both silicon[17] and gallium-arsenide[52]. However, due to results by [53], a three-terminal device may not be sufficient to separate the spin-signal from other signals. Thus, a four-terminal device may be needed, where the terminals are separated by approximately the spin diffusion length  $L_{SD}$  or less. Such a device is shown in Figure 2.7. In this figure, the red blob above the inner current injection electrode signifies the extent of the spin coherence due to diffusion. The inner voltage sensing electrode must be very close to the inner current injection electrode, or no spin polarisation is left at the sensing electrode.

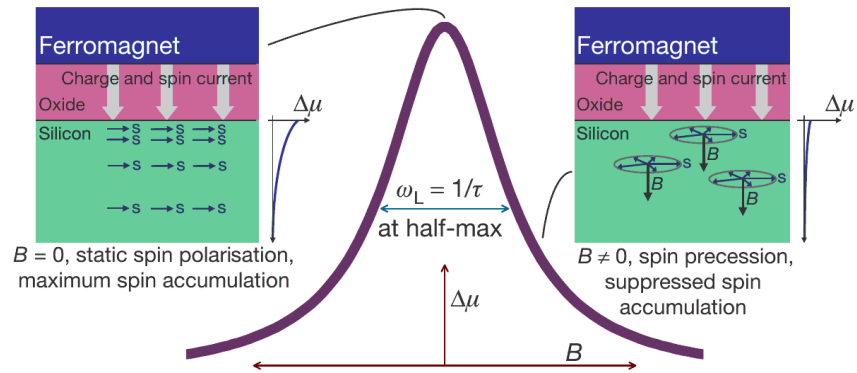


**Figure 2.6** – A schematic overview of a Hanle measurement. At zero field, the spin accumulation is at a maximum. By applying a magnetic field  $B_{\perp}$ , the spin accumulation is reduced by precession. [17]

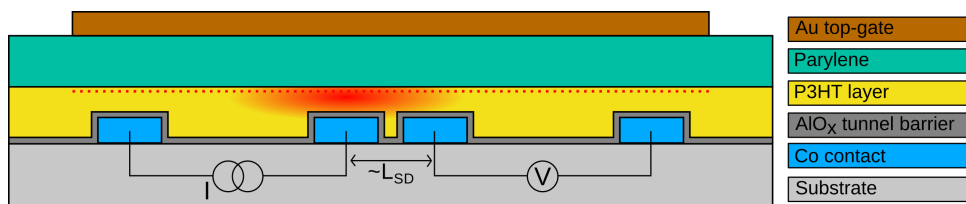


**Figure 2.7** – A schematic of the geometry of a four-terminal device for Hanle measurements.



## Chapter 3

# Experimental methods

In experimental research such as presented in this report, there are a wide variety of techniques available to fabricate and characterise samples. In this chapter, the main techniques which are used in this work will be presented. With it, the toolbox will be build which is used for the device fabrication and characterisation in Chapter 4, and with which the experimental results in Chapter 5 have been obtained.

### 3.1 Fabrication

Fabrication techniques can be divided in supporting techniques and deposition techniques. The supporting techniques such as photolithography are only meant as a tool during the fabrication process, while deposition techniques actually apply the layers of material that will be in the final device.

#### 3.1.1 Photolithography

The staple fabrication technique for electronic devices is photolithography. This technique uses a photoactive layer to apply a pattern to the substrate. First, a photoresist is applied to the surface, usually by spin-coating. Then, it is exposed to UV-light while pressed against a mask. This mask contains transparent and dark regions (usually made by depositing chrome). The precise behaviour of the photoresist is dependent on its type. In general, two types can be discerned, namely positive photoresist and negative photoresist. Positive photoresist is insoluble in the developer<sup>5</sup>, but will become soluble when it is exposed to UV light. Negative resist is by itself soluble in the developer, but becomes insoluble when exposed to UV light. Thus, positive resist remains on the substrate where the mask was dark, while negative resist will only remain where the mask was transparent, creating a negative image of the mask. The basic steps are shown in Figure 3.1(a).

The major advantage is that even intricate patterns can be created relatively quickly through the use of a mask. There are also many different photoresists available, with different characteristics and uses. The disadvantage is that a new mask must be made for each new pattern, and that the resolution is limited. Using the tools available in the MESA+ cleanroom, it is difficult to obtain features of 1  $\mu\text{m}$  or less in the photoresist layer. It is however possible to create features such as a pronounced negative slope (undercut) of the resist wall, useful in lift-off processes. In this work, an image reversal photoresist is used for precisely this reason. This resist works by introducing a reversal bake step after initial exposure. The reversal bake changes the exposed

---

<sup>5</sup> There are many different solvents that can be used as developer. For this work, OPD4262 was used in all cases.

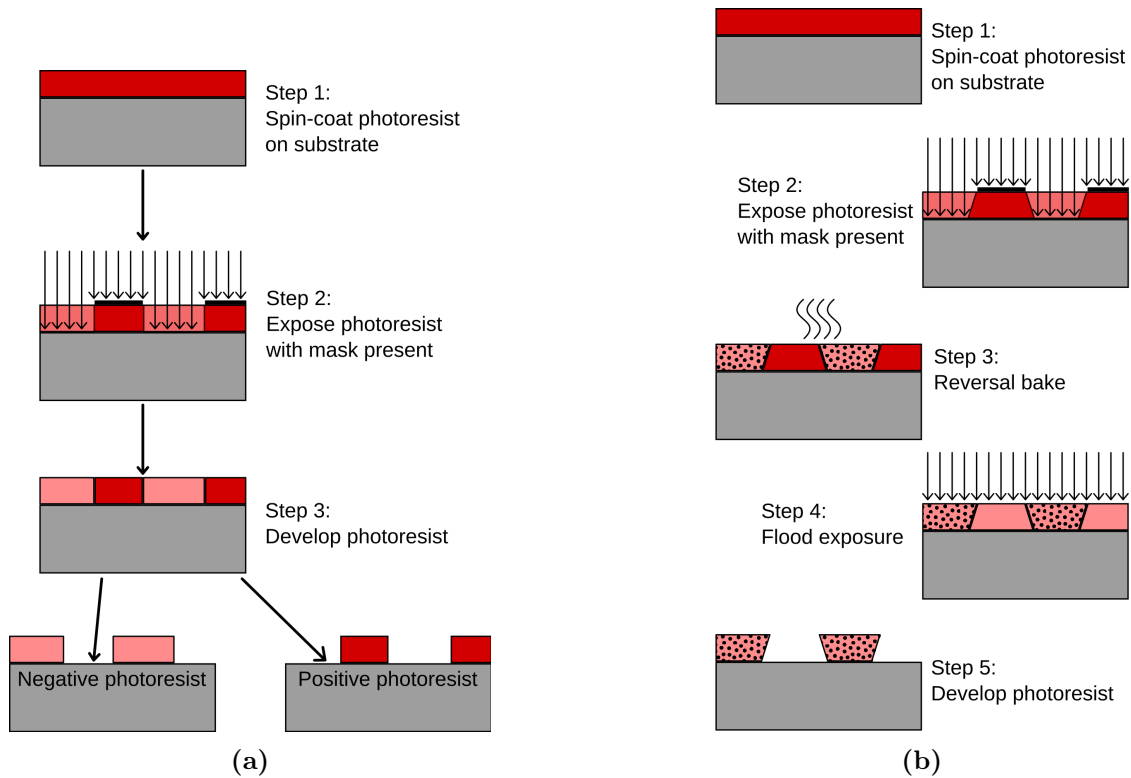


**Figure 3.1** – (a) shows the basic steps for getting a pattern in normal photoresist, either negative or positive. For image reversal photoresist as shown in (b), a reversal bake must be added.

(and soluble) photoresist to a fully inert state, where it is neither photoactive nor soluble in the developer. A subsequent flood exposure ensures that the rest of the photoresist becomes soluble and will wash away in the developer. Thus, such a resist is usable as both a positive and a negative resist, depending on whether the reversal bake and flood exposure are carried out or not. The basic steps for this type of photoresist are shown in Figure 3.1(b).

Photoresist is used in combination with other techniques. For example, it can be used as an etch-mask, to prevent certain areas of the underlying material from being etched away, thus transferring the photoresist pattern onto the underlying substrate. It can also be used as a lift-off mask, where a material is deposited on top of the photoresist. A lift-off step is then required to remove the photoresist and the metal on top with it. Thus, the only metallic regions that remain is where the photoresist was not present on the substrate. Especially for lift-off, the exact shape of the photoresist is important. Ideally, a good undercut as shown in Figure 3.1(b) of the photoresist wall is desired to ensure clean lift-off and a sharp definition of the remaining metal regions without ridges. Because of that, extensive optimisation has been performed on the photoresist as a part of this work, see Section 4.3.

### 3.1.2 Deposition techniques

There are many different techniques for growing thin metallic layers onto samples. In this work, only physical vapour deposition techniques were used. These rely on the deposition of vaporised metal atoms and clusters of atoms onto a substrate in vacuum. The deposition characteristics differ between them, with kinetic energy of the metal atoms, temperature of the substrate, directionality (if any) of the source, and vacuum level in the deposition chamber all being important. In this work, two main techniques were used. These techniques are electron-beam

physical vapour deposition (EBPVD) and magnetron sputtering.

EBPVD is a highly directional technique, and is done in an ultra-high vacuum (UHV) deposition system with a base pressure lower than  $10^{-9}$  mbar<sup>6</sup>. At these pressures, the mean free path of a gas molecule is of the order of 40 km, which means that there are hardly any interactions between two particles of the evaporated material. This has the advantage that the deposition of material evaporated by the electron beam is highly directional, making this technique very suitable for obtaining high-quality lift-off when combined with a photoresist that exhibits an undercut. In the MESA+ cleanroom, EBPVD can be done using an M600 deposition system by DCA instruments, hereafter called "the DCA", shown in Figure 3.2. This system is not only capable of EBPVD in UHV, but also of molecular beam epitaxy of both metallic and organic compounds, although with some severe limitations on the exact organic materials that can be used. This system has two electron guns, with different crucibles of material available for each. The sample holder is mounted in the top of the main vacuum chamber, and the sample is hanging up-side down. The crucible is far below the sample holder, and at an angle to the holder, see Figure 3.3. Thus, deposition is directed from the crucible to the sample holder.

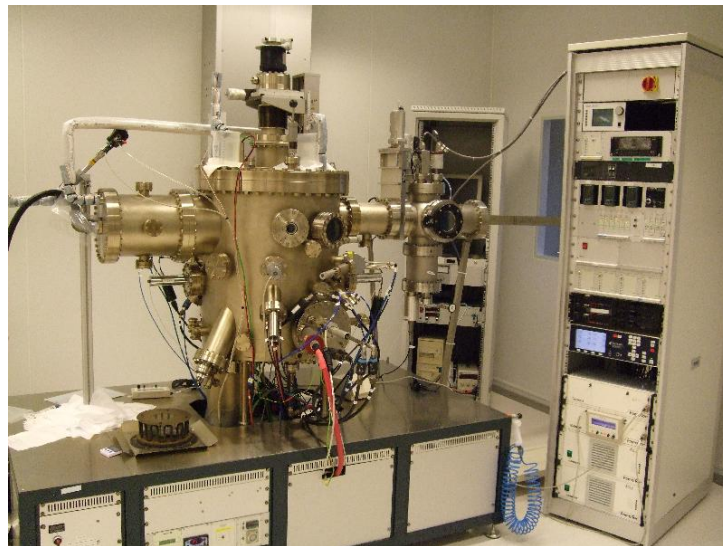


**Figure 3.2** – The DCA instruments M600 deposition system, proprietary of the NanoElectronics group, in the MESA+ cleanroom.

A load-lock system which is integrated into the DCA can also be used for in-situ oxidation of metallic layers. In this process, the loadlock is filled with  $O_2$  gas, using a mass-flow controller. The pressure is regulated by the position of the gatevalve separating the loadlock from the turbomolecular pump. A DC power source is used to generate a plasma of atomic oxygen, which is capable of diffusing into metallic layers. The approximate oxidation times for aluminium thin films are reported in Appendix A.7 of [71]. It is important to select a correct oxidation time. When the time is too short, a pure aluminium layer remains. When the time is too long, an antiferromagnetic layer of cobalt-oxide forms. Both are detrimental to the spin tunneling capabilities of the electrode[8].

Magnetron sputtering is the second major deposition technique used in this work. In magnetron sputtering, a target material is bombarded with ions, which in turn knock loose atoms or clusters of atoms of that target material. These particles then deposit on the substrate elsewhere in the vacuum chamber. Although multiple sputter-deposition machines are available in

---

<sup>6</sup> EBPVD can be performed at much rougher vacuum levels. However, the use of an ultra-high vacuum (UHV) chamber is beneficial because it provides very clean conditions for the deposition.

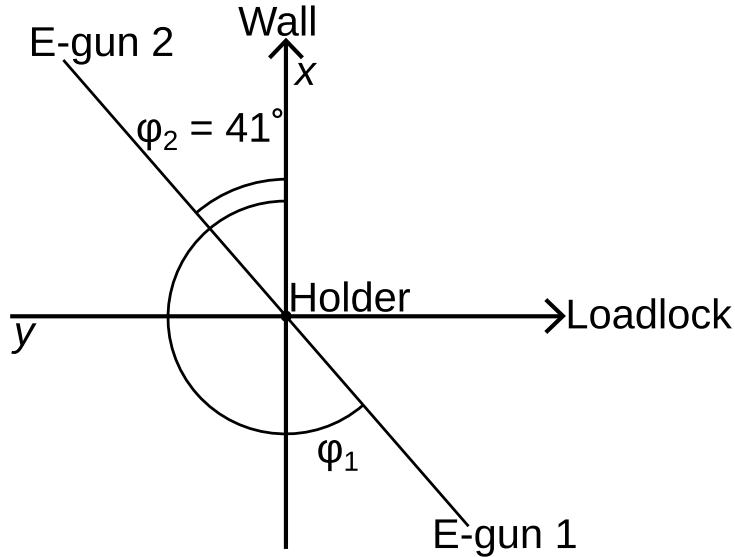


**Figure 3.3** – The orientation of the EBPVD crucibles with respect to the sample holder in the M600 deposition system by DCA instruments. Using a standard spherical coordinate system, the line from holder to wall is defined as  $x$ , and the line from holder to loadlock is defined as  $-y$ . The polar angles for both E-guns, as well as the azimuthal angle for E-gun 1, were not determined. The  $z$ -direction is not shown in this top-down view.

the MESA+ cleanroom, only the "Sputterke" was used in this work, shown in Figure 3.4. This magnetron sputtering machine is a simple one, offering only Ar as the sputtering gas, and only three different target materials per run, but it has a fast process time. Magnets are used to confine the Ar ions close to the target, increasing deposition rates. The base pressure of this machine is below  $10^{-7}$  mbar, and the process pressure is approximately  $6.6 \times 10^{-3}$  mbar. At this process pressure, the mean free path of gas molecules is several cm. This means that the target material is not deposited directionally onto the substrate, but rather comes in from almost all angles. Thus, sputtering is not useful if high-quality lift-off is desired without ridges at the metal-area edges, even if a photoresist with a good undercut is used.

### 3.1.3 Organic layer coating

In the development of organic spintronic applications, it is very important to get high-quality organic layers. In this work, two organic materials have been used. P3HT is used as the active layer for the transistor structures, while parylene is used as gate dielectric to separate the metallic top-gate from the P3HT below. If a sharp interface between a metallic material and an organic material is desired, then deposition of the organic needs to happen after the deposition of the metal. If this order is switched, significant interdiffusion of the metal into the organic material will occur during deposition, leading to a much rougher interface.

In general, organic materials and especially polymers cannot be deposited in UHV systems, because of high vapour pressures or unacceptable contamination of the vacuum chamber<sup>7</sup>. A very good technique for applying organic layers is spin-coating, since that is available for a wide variety of materials. Spin-coating is done by applying a droplet of the material in solution onto the middle of the substrate, and spinning the substrate at high rpm. This results in uniform polycrystalline layers, with the thickness of the layer being dependent on solvent characteristics, rotational speed and rotational time. Thus, it is relatively easy to adjust the process to obtain a

<sup>7</sup> Small organic molecules such as Alq3 or C<sub>60</sub> can be deposited in UHV.



**Figure 3.4** – One of the magnetron sputtering systems available in the MESA+ cleanroom. This particular system is nicknamed "Sputterke". Photo by MESA+ cleanroom staff.

specific film thickness. In this work, spin-coating is always done in dynamic mode, which means that a spread-out step at low rpm is added to the spin-coater recipe. The specific spin-coater recipe for coating P3HT is:

step	time	speed
1	10 s	500 rpm
2	45 s	6000 rpm

After spin-coating, a bake step is typically added to remove (part of) the solvent and improve the stability of the organic thin film. In the MESA+ cleanroom, wetbench 23 is specifically designated for processing polymers, and includes a spin-coater and a hotplate.

The coating of parylene cannot be done by spin-coating. Instead, it uses a dedicated system where a specific amount of precursor material ([2,2]paracyclophane) is vaporised in vacuum. The resulting dimeric gas is then pyrolysed at high temperature, before it is deposited in the deposition chamber at room temperature. Because of this room temperature deposition, the resulting parylene film is virtually free of stress. In the MESA+ cleanroom, such a system is available for the coating of Parylene C.

### 3.1.4 Reactive ion beam etching

Since the spin-coating of P3HT and the coating of parylene deposits these materials everywhere on the sample, reactive ion beam etching (RIBE) is used to pattern these layers. When using RIBE, a neutralised beam of oxygen atoms is accelerated towards the sample. This beam will preferentially etch organic materials due to the reactivity of the oxygen. Thus, by using a photoresist layer as an etch-mask, RIBE can be used to pattern the organic layers. In this work, an Oxford instruments Ionfab300Plus system is used, shown in Figure 3.5.

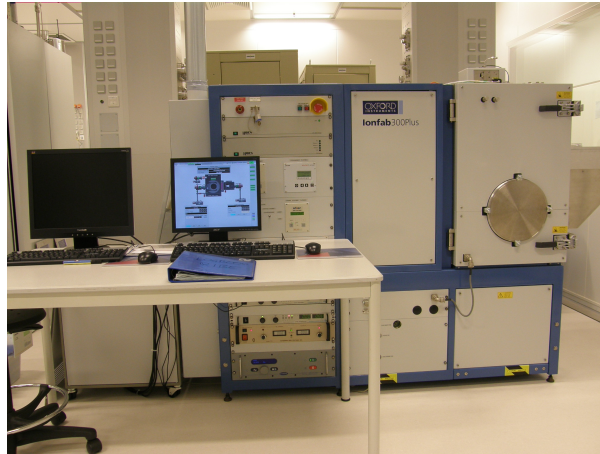


**Figure 3.5** – The Oxford Instruments i300 ion beam miller. This machine is used in this work for reactive ion beam etching. Photo by MESA+ cleanroom staff.

## 3.2 Characterisation

There are many different techniques available for examining the results of the fabrication process. These techniques range from the extremely simple, such as basic optical microscopy, to the highly advanced, such as scanning electron microscopy.

### 3.2.1 Optical microscopy

Optical microscopy techniques are numerous, ranging from the very simple to the highly complex. In this work, optical microscopy was only used for basic inspection of samples. The standard bright-field imaging was used for inspecting whether dirt is present on samples, inspecting whether the development of a photoresist layer is completed to satisfaction, or inspecting the result of gold or organic etching. Dark field microscopy was also used, and is especially useful for getting a first impression of surface quality after deposition. In dark field microscopy, the directly illuminating beam is excluded from the image, and only light that is scattered by the sample is collected, as is shown schematically in Figure 3.6. This greatly improves the contrast of the image, and imperfections such as etch marks show up very brightly in dark field images.

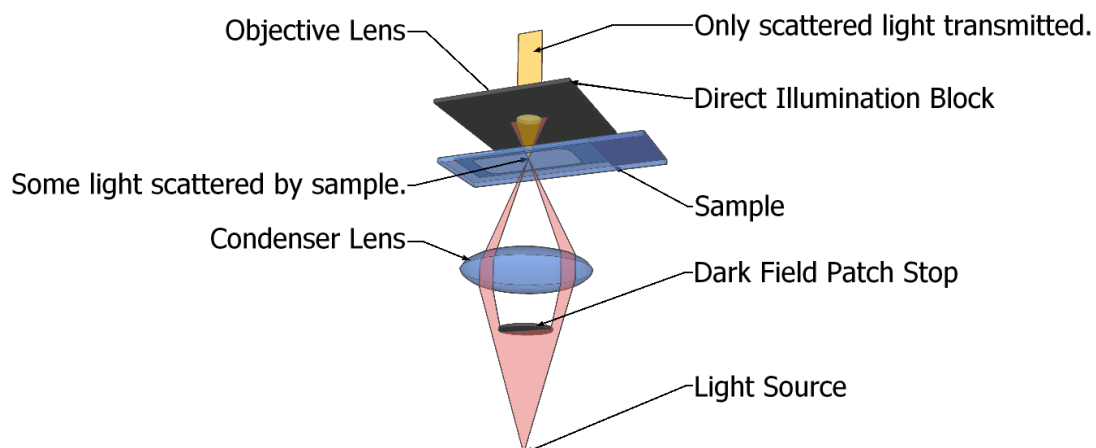


**Figure 3.6** – A schematic drawing of the working principle of a dark field microscope. The direct beam is excluded from the final image, and only scattered light is recorded. [72]

### 3.2.2 Atomic force microscopy

An atomic force microscope utilises a small cantilever with a very sharp tip. In tapping mode, this cantilever is brought in oscillation using a piezoelectric element, and is brought close to a surface. By measuring the change of the oscillation amplitude and phase of this cantilever as a function of its height, a topographical map of the surface can be made, see Figure 3.7(a). This technique is especially sensitive in the  $z$ -direction, allowing clear imaging of height differences as low as a few nm. In this project, an ambient-air VEECO Dimension 3100 AFM was used, see Figure 3.7(b). By making surface scans, the surface roughness could be determined for many different materials. Step heights were also determined, often at the edge of a small scratch applied by a metal tweezer. This method is especially useful for determining the thickness of organic layers such as parylene or P3HT, since these materials are easily scratched away without damaging the SiO<sub>2</sub> substrate beneath the organic layers.

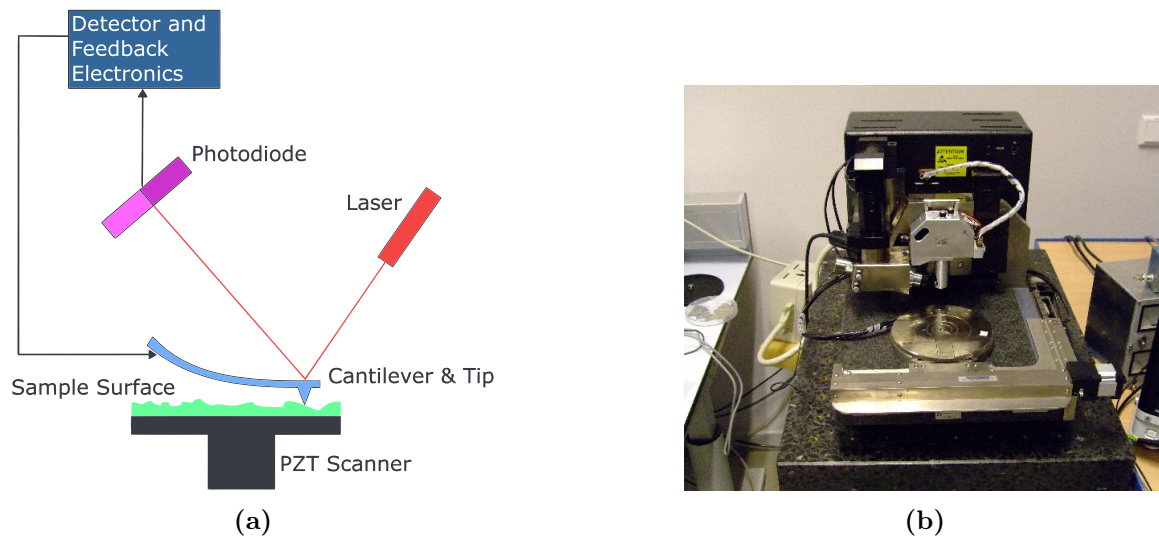


**Figure 3.7** – (a) is the schematic view of an AFM. In the AFM used in this work, the piezo-electric tube is attached to the cantilever, rather than to the sample holder. (b) is a photograph of the VEECO Dimension 3100 AFM used for all experiments reported in this work.

### 3.2.3 Scanning electron microscopy

A scanning electron microscope utilises a beam of accelerated electrons and their reflection and scattering off a surface to image that surface. Because the wavelength of an electron is much shorter than that of a photon, the resolution is orders of magnitude above that of optical microscopy, reaching sub-nm in high-resolution SEM machines. A disadvantage of this technique is that samples should be electrically conducting to get a good signal to noise ratio. In an insulating sample, electrostatic charge builds up and deteriorates the image by creating artifacts. SEM images were most often used in this work to gauge the profile of a photoresist layer. For this purpose, a substrate with photoresist coating was broken in two pieces, and the photoresist was imaged from the side, at the broken interface. A photograph of the SEM machine is shown in Figure 3.8.

### 3.2.4 Electrical measurements

In general, electrical characterisation of the devices was done using a combination of two Keithley source-meters. The use of two source-meters is necessary, because the gate voltage and drain

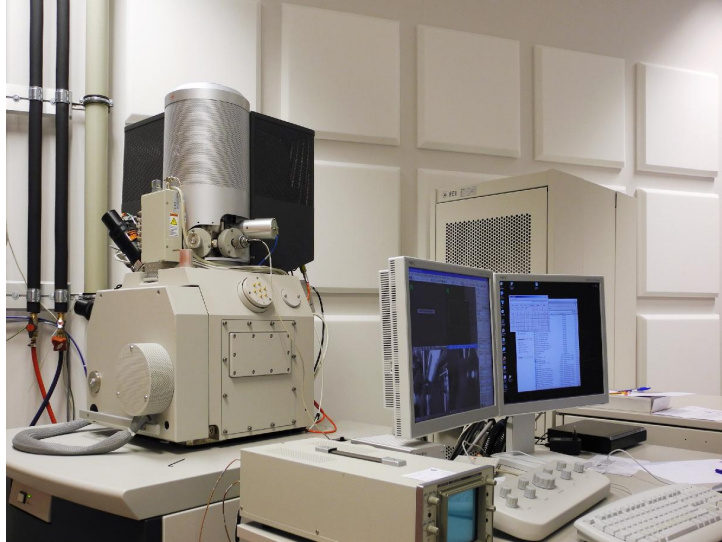


**Figure 3.8** – A photograph of the Nova 600 dual FIB system available in MESA+ NanoLab. It is a dual system, capable of imaging using accelerated electrons, and of etching using a focussed ion beam. The focussed ion beam capabilities were not used in this work. Due to the complexity of the machine, operator assistance is necessary. Photograph by MESA+ staff.

voltage need to be separately controllable when measuring IV and transfer curves of a transistor. Two types of source-meters were used, namely Keithley 2400 and Keithley 2401. The only difference between these is the maximum voltage. The Keithley 2400 can provide up to 200 V. The Keithley 2401 is only useful for low-voltage measurements, up to 20 V. Both devices are capable of a four-point measurement, both with a current bias and with a voltage bias, see Figure 3.9. When setting a voltage bias in a four-point measurement, the Keithley source-meter couples the sense input to the output in such a way that the desired voltage bias is measured on the sense, while the source outputs the current required to maintain that voltage bias as long as it is within the compliance. The major advantage of a four-point measurement compared to a two-point measurement is the exclusion of the lead resistances from the measurement results. Especially when the impedance of the test device is low, lead resistances can contribute significantly to the measurement errors.

### **Bruker**

The Bruker system is a combination of a Bruker magnet with an Oxford Instruments cryostat. Electronics such as a Keithley 2400 can be attached as desired. This makes it a useful system that can perform magneto-transport and electrical measurements at low temperature (down to 4 K), in an inert He-atmosphere, and inside a maximum magnetic field of 1 T. Because of this, the system is very useful for spin transport measurements. Since there are twelve contacts available inside the system, it is also useful for transistor measurements using four-point configurations. A photo of this system is shown in Figure 3.10(a), and the sample holder is shown in Figure 3.10(b).

### **Probe stations**

Probe stations are general-purpose measurement tools. They can be used to quickly measure many different structures, due to the ability to quickly change the position of any of the four probes. All that is needed are contact pads on the structure. The probes can be connected to any external apparatus, such as a Keithley 2400 source-meter.

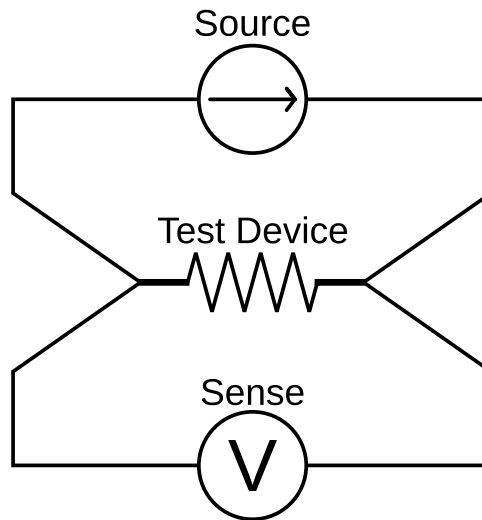


**Figure 3.9** – Schematics of a four-point measurement. The source is always a current source, while voltage can be measured across the sense output.

In this work, two probe stations were used intermittently for electrical measurements. The first one is a Janis ST-500 probe station with separate electronics, located in the NanoElectronics laboratory. Because this machine is heavily used by many members of the NanoElectronics group, the Cascade Summit 11000 probe station, belonging to the Semiconductor Components group, was also used. Both stations were only used for room-temperature measurements at atmospheric pressure, although they have capabilities for measurements at different temperatures.

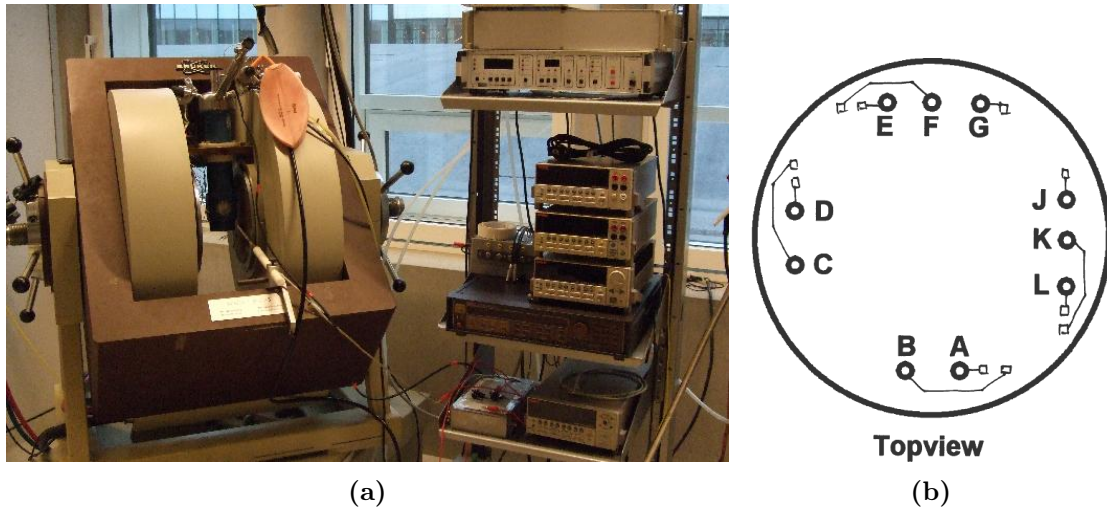


**Figure 3.10** – (a) is photograph of the Bruker system. A PC is attached which has a general-purpose measurement program, allowing for a wide variety of measurements. (b) is a schematic of the sample holder for the Bruker system. There are twelve contacts available.

## Chapter 4

# Device fabrication and characterisation

As is explained in Section 1.4, the goal of this project is to create a working organic spintronic device that can be used to probe spin accumulation, and through that spin lifetime. Such a device is envisioned to be a hybrid device, where the active layer is an organic material (P3HT), and the spin injection and detection electrodes are ferromagnetic cobalt with an  $\text{AlO}_x$  tunneling barrier.

### 4.1 Organic solvent compatibility

Since P3HT is used as the organic material in these devices, two different fabrication techniques must be used. P3HT cannot be evaporated onto the substrate in UHV. An easy method of depositing a thin film of P3HT is to spin-coat it onto a substrate. Given the difficulty in growing good metallic layers on organic materials without significant inter-diffusion and contamination of the organic layer, all ferromagnetic electrodes should already be deposited on the substrate, and the P3HT thin film must be spin-coated on top. Since P3HT by itself is solid, it must be dissolved. Numerous suitable solvents exist, such as 1,2-dichlorobenzene and bromobenzene. However, the ability of the ferromagnetic electrodes to inject a spin-polarised current is crucial to the goal of measuring spin accumulation effects. Thus, these solvents for P3HT were tested for any adverse effects on the  $\text{Co}/\text{AlO}_x$  electrodes.

#### 4.1.1 Magnetic tunnel junctions

The test used to determine the influence (if any) of the organic solvent on the capabilities of a  $\text{Co}/\text{AlO}_x$  electrode to inject a spin-polarised current, is the fabrication of magnetic tunnel junctions. To do this, EBPVD was used in the DCA, see Section 3.1.2. Using a shadow mask as shown in Figure 4.1, two 11 mm by 11 mm samples could be grown in-situ. The magnetic tunnel junction is shown schematically in Figure 4.2. For these tests, both samples were removed from the DCA system after depositing and oxidising the  $\text{AlO}_x$  tunnel barrier, and one sample was exposed to a solvent for 5 min. The other sample acted as a reference, grown in exactly the same conditions and with the same layer thicknesses as the sample exposed to a solvent.

These magnetic tunnel junctions were characterised by first taking an  $IV$  measurement across the junction. This  $IV$  measurement was done either in the Bruker system, or in the probe-station. In either case, a four-point measurement was done as shown in Figure 4.3. For this  $IV$  measurement, the voltage was typically swept between  $-400$  mV and  $+400$  mV, starting and ending at zero, while the current was recorded. For a magnetic tunnel junction of good quality, a distinct non-linear  $IV$  profile is expected, corresponding to the tunneling behaviour of the junction. Only if the  $IV$  curves show such behaviour, is an MR curve measured in the

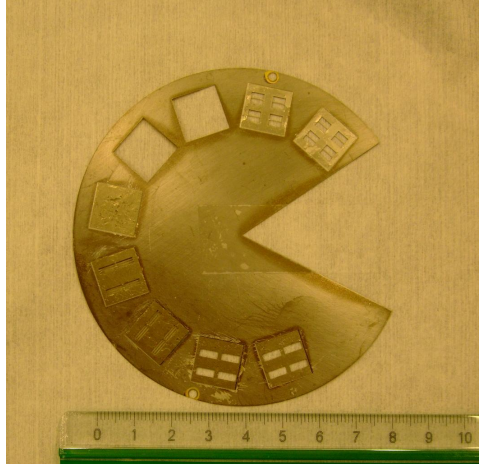


**Figure 4.1** – Photograph of the shadow mask used in fabricating magnetic tunnel junctions. The scale shown in the bottom is in cm.

Bruker system. The MR curves are measured by setting a 20 mV bias and measuring the current while sweeping the magnetic field between a high positive field and a high negative field. This should, in theory, result in a curve like Figure 1.5(b). The direction of the magnetic field is not varied, and is pointed parallel to the long axis of the NiFe top contacts.

## 4.2 P3HT thickness

When P3HT is gated, a conduction channel forms at the interface between P3HT and the dielectric material. Although the conduction is limited to a very narrow region near the interface, the total thickness of the P3HT is still very important. This is especially the case in the top-gated design, shown in Figure 4.4. In this design, the conduction channel is separated from the ferromagnetic electrodes by the P3HT thickness. Thus, to get spin-polarised electrons into this channel, they need to overcome the barrier presented by the poorly-conducting P3HT. This means that the thickness of the P3HT must be chosen carefully. If it is too thin, no continuous layer is expected. If it is too thick, it may not be possible to polarise the spins of the charge carriers in the conduction channel. In practice, the thickness of P3HT is chosen to be similar to the ferromagnetic electrode thickness.

The easiest way to vary the thickness is by varying the rotational speed of the spin-coater used to apply the P3HT thin film. Other methods, such as adjusting the concentration of P3HT in the solvent, require more work. The calibration was done on silicon substrates, with a thermally grown  $\text{SiO}_2$  layer approximately 320 nm thick. In all cases, the solution was kept at a concentration of  $10 \text{ mg ml}^{-1}$ . The full cleanroom procedure followed for spin-coating is attached to this report as Appendix A.1, step 11. During calibration, only the speed of the final spin step was adjusted, all other parameters in the recipe were kept constant. The thickness was measured by AFM by measuring the step edge of a channel scratched in the organic layer using a metal tweezer. If the scratching of the channel significantly influences the layer thickness close by, this should also result in a significant change in surface roughness close to the channel. Thus, the surface roughness near the scratch and far away from the channel must both be measured.

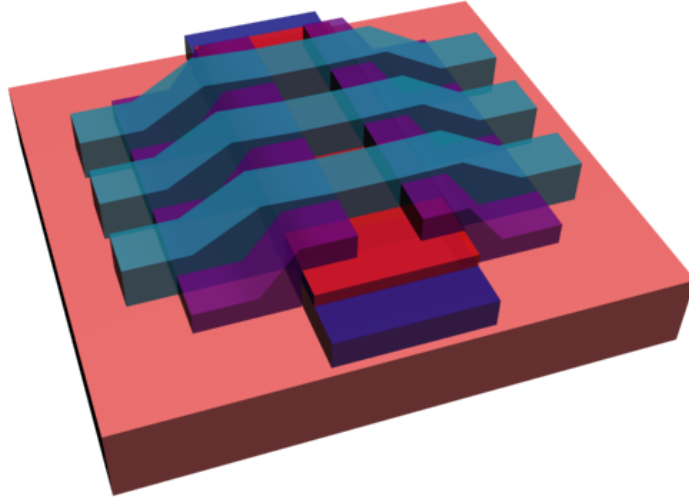


**Figure 4.2** – Schematic view of magnetic tunnel junctions. The bottom substrate is sapphire (pink), with cobalt (blue), AlO<sub>x</sub> tunnel barrier (red), AlO<sub>x</sub> (purple), and NiFe (cyan). An aluminium capping layer on top of the NiFe is not shown. The two consecutive layers of AlO<sub>x</sub> are grown in different ways. For the first layer, aluminium is deposited, which is then oxidised in an oxygen-plasma environment. For the second layer, AlO<sub>x</sub> is deposited straight from a crucible. [73]

### 4.3 Photoresist optimisation

For the magnetic O-FET devices, it is very important to have cleanly defined ferromagnetic electrodes without ridges at the edge of the electrodes. If the edges of the electrodes shown in Figure 4.4 do have ridges, they will penetrate through the P3HT layer, and will alter the injection process of the charge carriers to go primarily via these ridges, rather than via the bulk of the electrode. This will adversely affect the spin coherence of the injected current, hampering spin-accumulation measurements.

Such ridges often appear as a by-product of the photoresist used in a lift-off patterning technique. Typical photoresist will have slanted walls, such as shown in Figure 4.5(a). This means the walls get covered with metal during deposition, and the metal on these walls will not always detach cleanly from the metal on the substrate during the lift-off process. This results in ridges at the edge of the electrodes. However, if a directional deposition technique is used such as EBPVD in the DCA, and if the photoresist has an inversely slanted wall such as shown in Figure 4.5(b). then there will be no metal layer that needs to be detached during lift-off, and ridges are very unlikely to appear.

The precise shape of the photoresist is very dependent on the parameters of the recipe. For this work, image reversal resists Ti09 and Ti35 were used. The two main parameters that determine the shape of this resist after development are the initial exposure dose and the development time, shown schematically in Figure 4.6. The initial UV exposure dose determines the final attainable shape. This initial dose can easily be changed in the mask-aligners used in the MESA+ cleanroom. Since development was done by hand in OPD4262 developer, the development time could easily be varied between different samples. The measurement of the photoresist profile was done using the SEM, by looking at the cross-section of a sample that was broken across the photoresist structure.

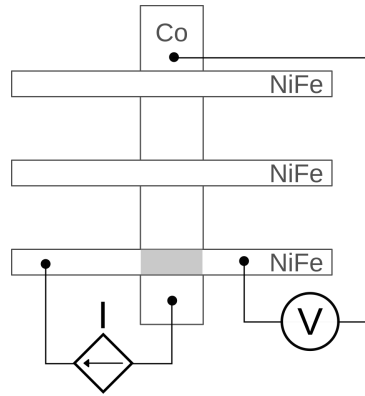


**Figure 4.3** – Schematic view of probe placement on an  $IV$  measurement of the magnetic tunnel junctions. The grey area signifies the tunnel junction area.

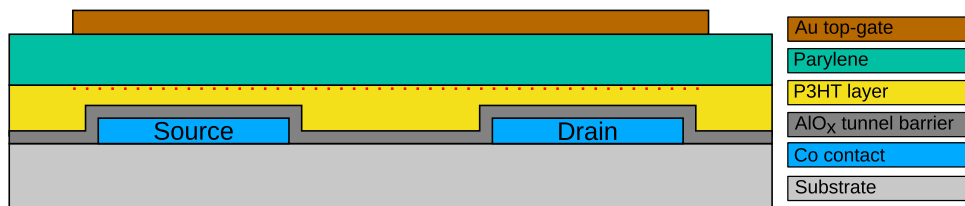


**Figure 4.4** – The schematic view of an organic top-gated field-effect transistor. The red dotted line indicates the position of the gate-induced conduction channel. The distance between the ferromagnetic contacts and this channel forms an injection barrier that must be overcome.

## 4.4 Back-gated O-FET

As a precursor step to the final top-gated device, a back-gated organic field-effect transistor was created and characterised. This geometry, shown in Figure 4.7, has both advantages and disadvantages compared to a top-gated geometry. One of the major advantages is the simplicity of fabrication. For a back-gated device, only a single photolithography step is necessary, eliminating difficult mask alignment of subsequent steps. The lithography mask pattern is shown in Figure 4.8. It also requires only a single coating step for the P3HT layer. Since the gate electrode was already present in the substrate and the P3HT is thin enough to be pierced directly by the wirebonder, no etching steps were necessary.

The substrate used was doped silicon with a thermally grown  $\text{SiO}_2$  layer of approximately 300-320 nm thick.  $\text{SiO}_2$  presents a large number of hydroxyl groups at the surface, and since the conduction channel induced by the gate is located near the interface between the  $\text{SiO}_2$  and P3HT, very low n-type conductivity is expected for these devices[24].

Furthermore, any other impurities at the substrate surface are expected to influence the conduction channel. An additional weakness of this back-gated design is the susceptibility to gate leakage. Many of the transistors tested showed an ohmic contact between the silicon substrate and the source or drain contact. This most likely happened when bonding aluminium wires to the contacts to probe the structures. Since the gate dielectric is only approximately 300 nm thick, it is quite easy to break through it with the ultrasonic wire bonder.

The fabrication of the back-gated devices was also used as a first test of the lift-off procedure which is to be used in the top-gated devices. For this lift-off, both Ti09 and Ti35 image reversal photoresist was used, combined with acetone and dimethyl sulfoxide (DMSO) as lift-off solvent. This variation in lift-off procedure is the primary cause for the variation in channel lengths observed in these devices. The success of the lift-off was determined by measuring the contacts

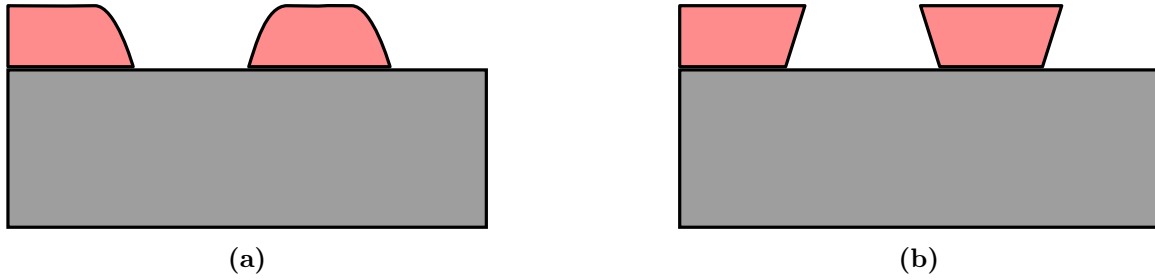


**Figure 4.5** – (a) is the profile of a typical positive photoresist. This edge profile is most problematic in lift-off applications where clearly defined edges without ridges are required. (b) shows the inverse slanted wall profile which can be obtained using image reversal photoresists.

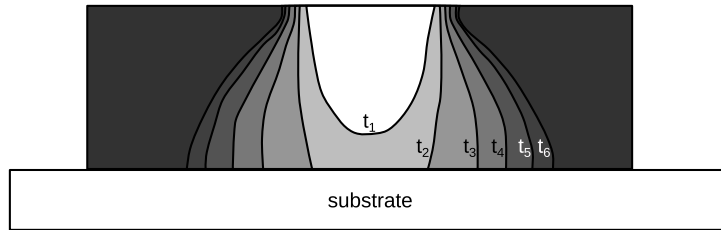


**Figure 4.6** – The shape of the image reversal photoresist Ti35 is most dependent on two parameters. In this figure, the influence of the development time  $t$  is shown. A good undercut only starts to form at longer development times. Here,  $t_1$  through  $t_6$  are from shortest development time to longest development time. Image adapted from [74].

under AFM. This readily shows if any ridges are present. Electrical characterisation of these devices was done using the Cascade Summit 11000 probe-station combined with a Keithley 4200 SCS<sup>8</sup> in the common source configuration shown in Figure 2.1.

Three distinct types of back-gated O-FET devices were made, each with a different doping of the Si back-gate. More minor variations in lift-off resist and P3HT anneal times were also incorporated, but not extensively measured. The three dopings are p-type (doped with boron,  $\rho = 5 - 10 \Omega \text{ cm}$ ), n-type (doped with phosphorus,  $\rho = 1 - 10 \Omega \text{ cm}$ ) and n++-type (highly doped with arsenic,  $\rho = 0.001 - 0.005 \Omega \text{ cm}$ ). For all transistors, an IV curve was measured by varying the drain voltage at fixed gate voltage, and repeating for different gate voltages. The current through the gate electrode was also measured. In a perfect device, the gate current should be zero.

## 4.5 Top-gated O-FET

The top-gated device geometry is the main project, since spin-accumulation measurements are anticipated to be possible on such a device with good spin-injection characteristics<sup>9</sup>. The full fabrication recipe for this device is found in Appendix A.1, and is shown schematically in Figure 4.9. For the first fabrication run, the recipe was simplified by depositing the electrodes and contact pads in one step, using a 5 nm Ti adhesion layer with a 40 nm Pt layer. Suitable patterns are available on the photolithographic mask.

Step 1 in Figure 4.9 is the deposition of the ferromagnetic electrodes using lift-off photolithography. For this, it is important to use image reversal photoresist with a good undercut,

<sup>8</sup> With many thanks to the Semiconductor Components research group for allowing access to their probestation.

<sup>9</sup> When using a back-gated geometry, current is mostly injected through the poorly-defined side of the electrode, rather than through the well defined tunnel barrier on top of the electrode.

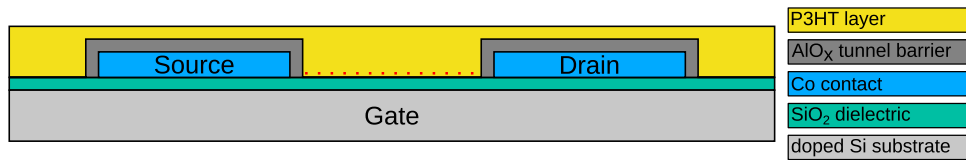


**Figure 4.7** – The schematic view of an organic back-gated field-effect transistor. The red dotted line indicates the position of the gate-induced conduction channel.

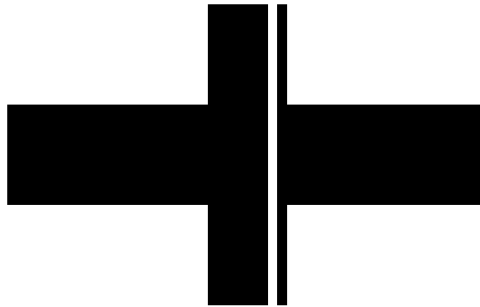


**Figure 4.8** – The lithography mask pattern unit cell used for the back-gated O-FET devices. Image reversal photoresist combined with lift-off was used, so the dark part of the mask is the part where the electrodes end up. The distance between the two electrodes was constant at  $9\ \mu\text{m}$  on the mask. The actual distance was dependent on the exact type and recipe for the photoresist.

followed by lift-off in acetone. The ferromagnetic electrodes are made by deposition of 10 nm of cobalt, followed by 2.5 nm of aluminium. Because of the effect of an oxygen plasma on the photoresist, oxidation of the aluminium layer must happen after lift-off. The thin native oxide layer that develops naturally on the aluminium is no issue, since the main purpose of the oxygen plasma is to oxidise the deeper layers of aluminium by diffusion of atomic oxygen. The use of a resist with a large undercut prevents ridges from forming. AFM measurements are used to verify the quality of the lift-off afterwards.

Step 2 in Figure 4.9 is the deposition of metal contact pads on top of the ferromagnetic electrodes. For this step, the use of image reversal photoresist with a good undercut is less critical, since ridges at the edge do not matter as much. However, using such a resist makes lift-off easier, by providing a clear way in for the acetone to dissolve the resist. Contact pads are deposited in Sputterke and consist of a 5 nm Ti adhesion layer with a 40 nm Pt layer on top. The lift-off is again done in acetone.

Steps 3 and 4 in Figure 4.9 show the spin-coating of the P3HT active layer and the coating of the parylene gate dielectric respectively. The P3HT thickness is chosen similar to the thickness of the ferromagnetic electrodes, and is primarily influenced by the spin-coating speed. The thickness of the parylene is determined by the amount of precursor material inserted into the crucible, using a calibration table provided with the machine. The thickness chosen for this device is 200 nm. Since these thicknesses tend to vary, it is important to add dummy samples of the same substrate, which can be used to measure the actual thickness using AFM or Dektak. These dummy samples can also be used for the calibration of the organic etch step later on.

Step 5 in Figure 4.9 shows the deposition of the top-gate layer. This is a double layer consisting of a 5 nm Cr adhesion layer with a 50 nm gold layer, both deposited in Sputterke. These layers are sputtered after a drop of photoresist is applied to the four alignment markers in the corners. After deposition, a short lift-off in acetone removes the photoresist, clearing the alignment markers to provide good visibility. Next, an etch-mask of positive photoresist is applied using the gate electrodes pattern. This mask protects the actual gate area when etching

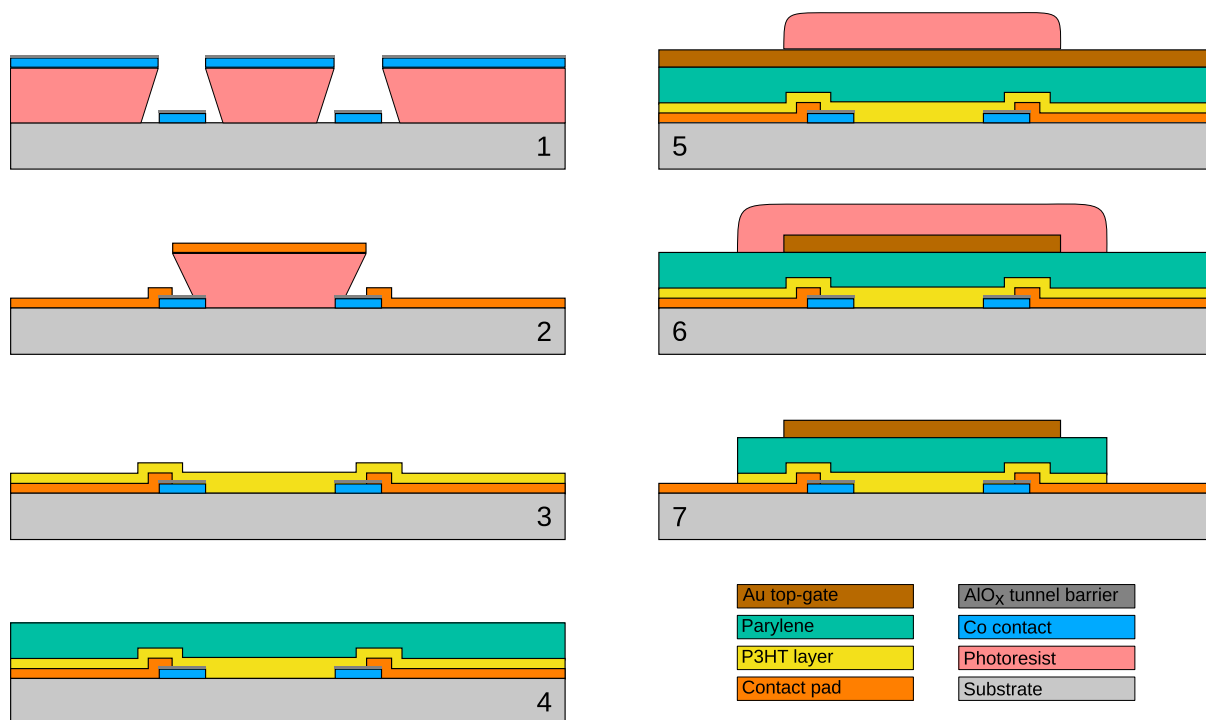


**Figure 4.9** – The schematic process for fabricating top-gated magnetic O-FET devices. The explanation of the different steps is given in the text of Section 4.5. The detailed fabrication recipe is attached as Appendix A.1.

the gold and chromium layers. Etching happens in gold etchant<sup>10</sup>, followed by chromium etchant. The etch rates for both etchants are approximately  $60 \text{ nm min}^{-1}$ , but vary significantly. Thus, it is important to add dummy samples to the gold sputtering step and coat these with photoresist, to test the etching speed, and adjust the etch time if necessary.

Step 6 in Figure 4.9 shows how, after gate etching and washing, a new photoresist pattern is applied. This pattern is designed to protect the ferromagnetic electrodes and the organic materials over these electrodes during the subsequent RIBE step. This etch step is necessary to expose the contact pads to the ferromagnetic electrodes, since bonding through the P3HT/parylene layer is very difficult with the wirebonder. During this etch-step, 5 sccm of Ar is directed into the neutraliser, and 10 sccm of O<sub>2</sub> is directed into the beam. This etching method is very selective towards organic materials, and reaches etching speeds of approximately  $60 \text{ nm min}^{-1}$ . Last, the samples are cleaned again to remove the photoresist used as etch-mask. This frees the top-gate contact pads for wirebonding, as is shown in step 7 of Figure 4.9.

#### 4.5.1 Electrical characterisation

After this fabrication process, the top-gated devices are ready for electrical characterisation. This is done in the Bruker system with two Keithley 2400 source-meters<sup>11</sup>. Figure 4.10 shows the wiring for a four-point measurement of the source-drain current, combined with a two-point measurement of the gate current. If a two-point measurement of the source-drain current is sufficient, the sense-wires on the second Keithley unit can be removed. For these measurements, only two of the five available electrodes were used. Care must be taken to use two adjacent electrodes in order to keep the channel length constant. A typical measurement of the IV

<sup>10</sup> A solution of 40 g KI, 10 g I<sub>2</sub>, and 400 ml DI water, available as a standard chemical in the MESA+ cleanroom.

<sup>11</sup> For low-voltage measurements <20 V, Keithley 2401 source-meters can be used instead without any problems.

characteristics sweeps the drain voltage from 0 V to the largest positive voltage, from there down to the largest negative voltage, and back to 0 V. To test the device stability, a constant drain voltage bias and gate voltage bias was applied, and both the gate current and the drain current was measured versus time. A third test, which was not done on the devices measured in this work, is to apply a constant drain voltage bias, and to sweep the gate voltage while measuring the drain current and the gate current.

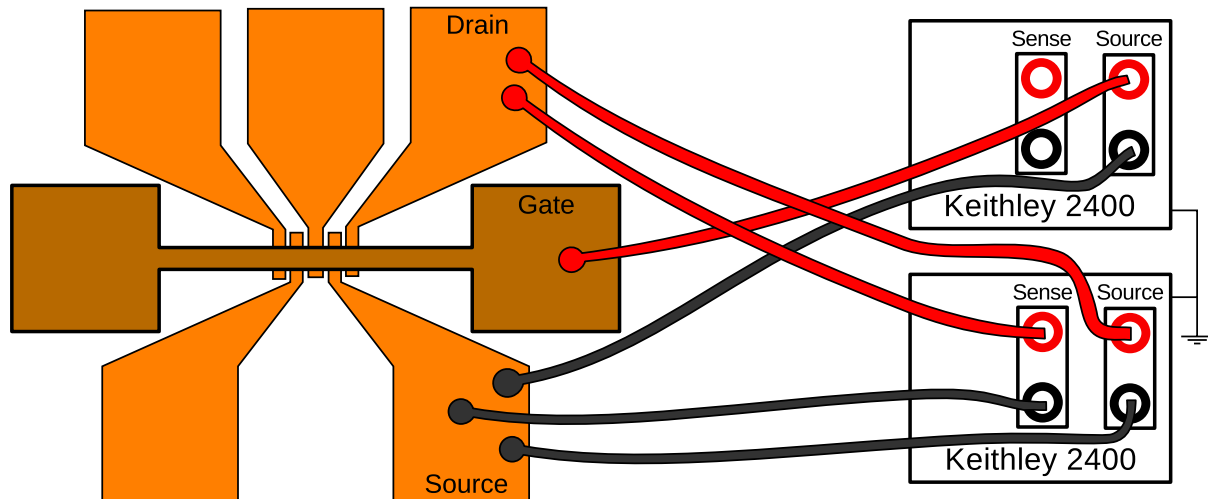


**Figure 4.10** – The wiring diagram for transistor measurements on top-gated magnetic O-FET devices. Measurements were performed in the Bruker system.

## Chapter 5

# Results & discussion

### 5.1 Organic solvent compatibility

The results of the measurements to determine the solvent compatibility described in Chapter 4 show clear MR behaviour for all substrates that exhibited non-linear  $IV$  curves. Due to some fault in the fabrication process, many of the grown samples showed linear  $IV$  behaviour, indicating a metallic contact between the bottom cobalt layer and the top permalloy layer. Such samples were not tested for any MR behaviour. This is very likely caused by the process of taking out the samples for solvent exposure after oxidation of the  $\text{AlO}_x$  tunnel barrier. Magnetic tunnel junctions grown in the usual way, without removal from the DCA system for solvent exposure, show higher tunnel resistance, clearly non-linear  $IV$  characteristics, and MR values of approximately 18%, see Figure 5.1. Two solvents were tested for their compatibility with  $\text{Co}/\text{AlO}_x$  electrodes. The MR curves for the bromobenzene test samples are shown in Figure 5.2. The MR curves for the 1,2-dichlorobenzene test samples are shown in Figure 5.3.

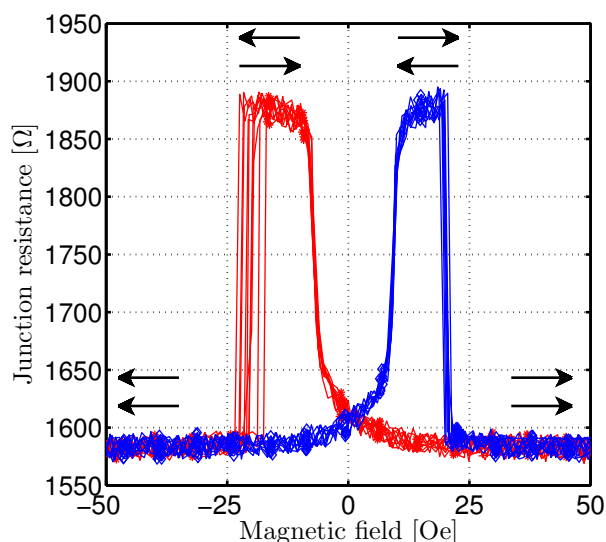


**Figure 5.1** – The resistance versus magnetic field for 10 magnetic field sweeps, measured on a standard magnetic tunnel junction which was not taken out of the DCA during fabrication. The blue curves show the sweep to positive magnetic field, while the red curves show the sweep to negative magnetic field. The arrows indicate the direction of magnetisation of the permalloy (top arrow) and the cobalt (bottom arrow). Interestingly, the coercivity of the cobalt layer is seen to drift slightly, especially on the sweep to negative magnetic fields. This is commonly called a training effect, and has to do with the reorganisation of magnetic domains in the cobalt layer.

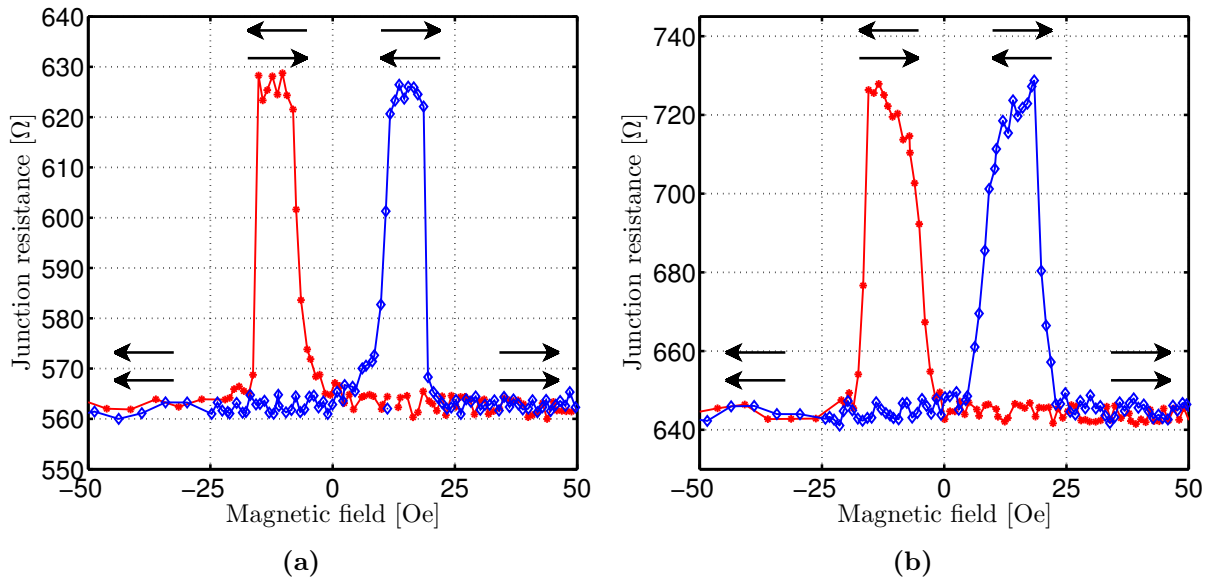


**Figure 5.2** – (a) shows the MR curve of the reference sample, and has an MR value of 11%. (b) shows the MR curve on the sample exposed to bromobenzene, with an MR value of 12%. The blue curves show the sweep to positive magnetic field, while the red curves show the sweep to negative magnetic field. The arrows indicate the direction of magnetisation of the permalloy (top arrow) and the cobalt (bottom arrow).

From these curves, we can conclude that neither of the two solvents influence the ability of the Co/AlO<sub>x</sub> electrode to inject a spin-polarised current, since there is no clear difference in MR values for exposed samples versus their accompanying reference samples. The selection of the solvent then depends on other properties, such as solubility of P3HT in the solvent, and the flash point and boiling point. The first property is important because the concentration of the solution is a good method to control the thickness of spin-coated P3HT. Diluting the concentration is expected to linearly decrease the final thickness, even at identical spin-coating rotational speeds. Bromobenzene has a clearly higher solubility compared to 1,2-dichlorobenzene (Table 1 of [39]). However, the desired thickness in this work is of the order of 10 nm, which is easily obtainable with low concentrations of P3HT. Since 1,2-dichlorobenzene has a higher boiling point of 180.5 °C, compared to 156 °C for bromobenzene, 1,2-dichlorobenzene was selected as the solvent for P3HT spin-coating. This higher boiling point is advantageous, since it offers more potential control over the evaporation rate of the spin-coated solution. This in turn can influence the crystallinity of the P3HT thin film, which is very important for obtaining good charge carrier mobilities in the final device.

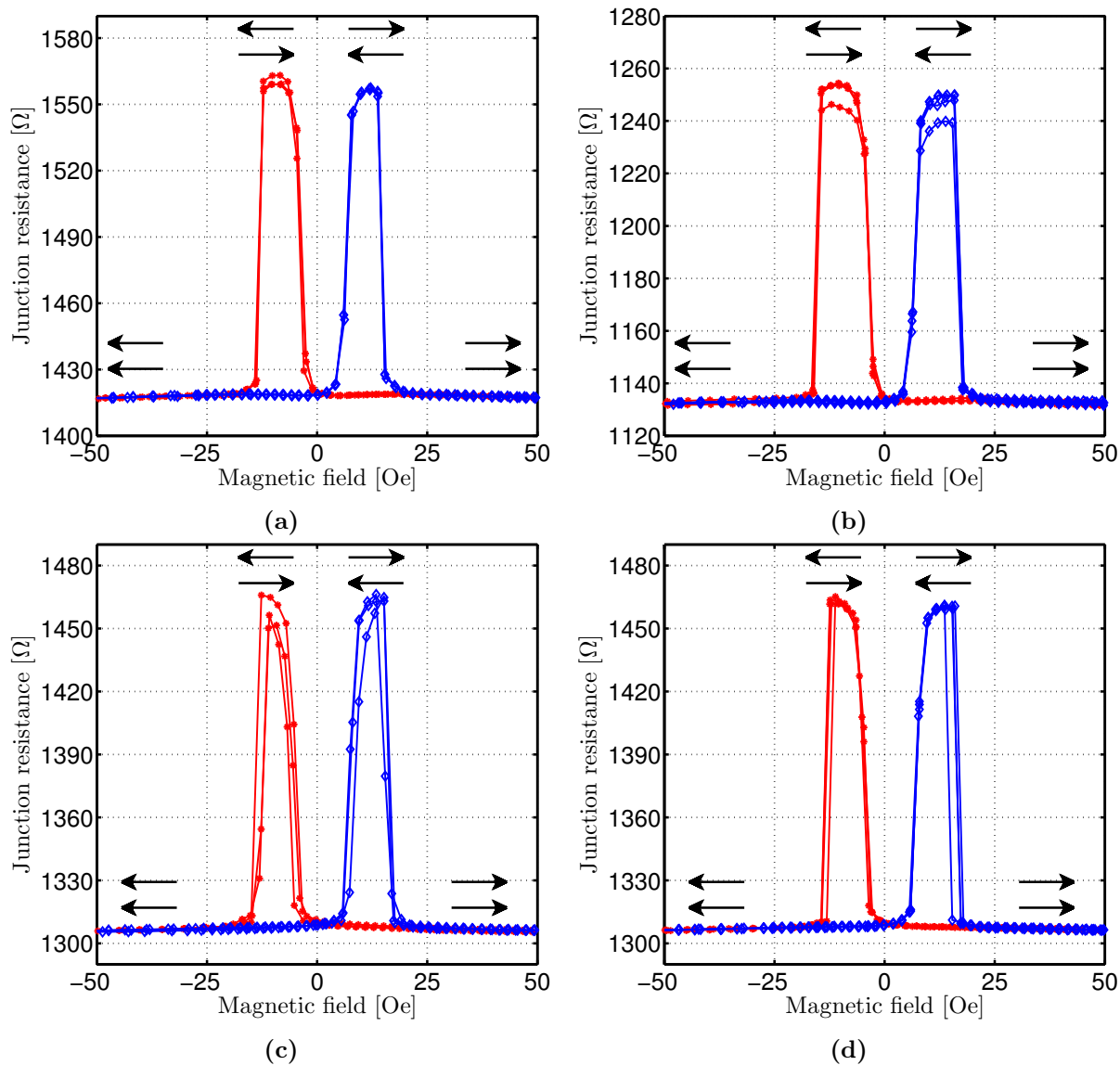


**Figure 5.3** – (a) and (b) show MR curves for two junctions on the reference sample, both showing a MR value of 10% according to Equation (1.2). (c) and (d) show MR curves for two junctions on the sample exposed to 1,2-dichlorobenzene. These actually show slightly higher MR values of 11% and 12% respectively. The blue curves show the sweep to positive magnetic field, while the red curves show the sweep to negative magnetic field. The arrows indicate the direction of magnetisation of the permalloy (top arrow) and the cobalt (bottom arrow). These measurements are done by Kai Wang at room temperature and contain multiple magnetic field sweeps.

## 5.2 P3HT thickness

From the P3HT spin-coated calibration substrates, the thickness as function of the spin-coating rotational speed was determined. This was done by scratching a channel into the P3HT layer using a metal tweezer. A light scratch is enough to fully remove the P3HT without damaging the SiO<sub>2</sub> substrate below. The step-edge of this channel was measured by AFM to determine the thickness, see Figure 5.4(a). The surface roughness was also determined, both close to the scratched channel and far away from it, see Figure 5.4(b).

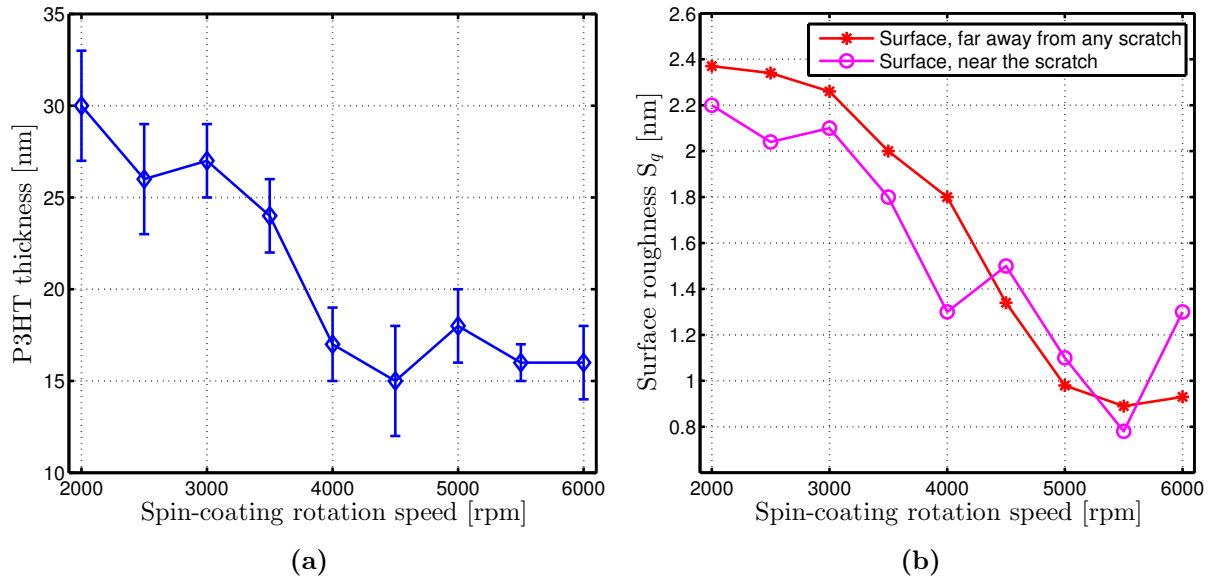


**Figure 5.4** – (a) shows the thickness of P3HT as a function of the rotational speed. (b) shows the roughness of the P3HT both close to the scratch and far away.

Clearly, the surface roughness improves for higher spin-coating speeds. The clear correlation between the surface roughness measured far away from any scratched channel and the surface roughness measured close to the channel indicates that the layer likely is not disturbed significantly near the channel. Thus, the thickness measurements are not influenced by the method of obtaining the channel. The concentration of 10 mg ml<sup>-1</sup> is sufficient to obtain layers approximately 10-15 nm thick, at the highest spin-coating rotational speed of 6000 rpm.

## 5.3 Photoresist optimisation

For the fabrication of high-quality magnetic electrodes using lift-off photolithography, it is important to have high-quality photoresist with a good undercut. The easiest method to determine the exact profile of a photoresist edge is to break the substrate the photoresist is spin-coated on, and to image the side using a scanning electron microscope.

The first photoresist which was investigated is the Ti09XR<sup>12</sup> image reversal photoresist. This resist normally spin-coats to a thickness of approximately 900 nm, making it useful for difficult alignment steps in the mask aligner, since the photoresist layer is thin and does not significantly reduce the sharpness of the underlying markers. The basic recipe for spin-coating this resist is shown in Table 5.1. Results with observed ridges in the back-gated O-FET devices prompted

<sup>12</sup> XR stands for eXtended Resolution, since techniques are available to obtain sub- $\mu\text{m}$  resolutions with this resist. However, that particular property was not used in this work.

SEM measurements of this resist, shown in Figure 5.5. Clearly, this photoresist does not have an undercut when patterned using this recipe. Since image reversal photoresist is expected to develop a more pronounced undercut at longer development times (see Figure 4.5), this was tested and imaged in the SEM. As shown in Figure 5.6, the width of the photoresist was slightly reduced at longer development times because more photoresist is removed from the edges of the layer. However, SEM images shown in Figure 5.7 show no formation of an undercut in the photoresist layer.

Step	Description
1	Apply Ti09 resist using 4000DYN recipe & 0.45 $\mu\text{m}$ filter
2	Bake for 50 s at 100 $^{\circ}\text{C}$
3	Expose for 4.5 s
4	Reversal bake for 60 s at 130 $^{\circ}\text{C}$
5	Flood exposure for 30 s
6	Development for 30 s

**Table 5.1** – Basic recipe for applying Ti09 photoresist.

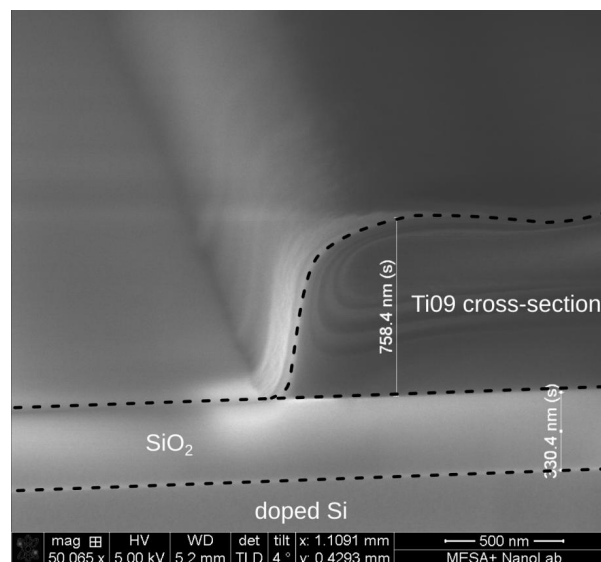


**Figure 5.5** – Scanning Electron Microscopy image of a Ti09 image reversal photoresist layer, with a 4.4 s first exposure time and a 30 s development time.

It is clear that no undercut is formed using the Ti09 photoresist. It is possible that this resist is simply too thin to develop a good undercut. For this reason, the thicker variant Ti35ES image reversal photoresist is tested. The basic recipe used for this resist is listed in Table 5.2. The SEM image of the Ti35 photoresist is shown in Figure 5.8. It shows a very pronounced undercut in the walls of the photoresist. However, the width of the strip is also clearly less than it should be according to the mask pattern. This photoresist was used for the fabrication of the  $n^{++}$ -substrate back-gated O-FET devices.

For the photolithographic mask used for top-gated O-FET devices, the width of the photoresist strips is 4  $\mu\text{m}$ , much less than the feature width for the back-gated O-FET devices. This resulted in the Ti35 photoresist being completely washed away when applied using the recipe in Table 5.2. To remedy this, shorter development times were tested, of which the SEM images are shown in Figure 5.9. The undercut is only formed when at least a 45 s development time is used.

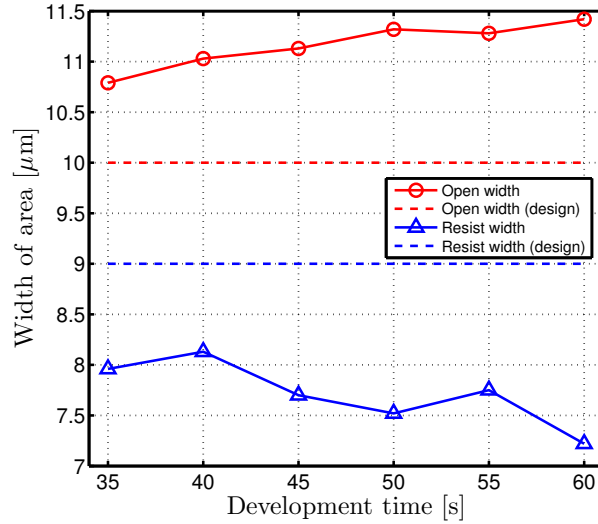


**Figure 5.6** – The width of the Ti09 photoresist strip structured using the back-gated mask. The open area is the width of the smallest electrode, see Figure 4.8.

Step	Description
1	Apply HMDS using 4000DYN recipe & 0.2 μm filter
2	Apply Ti35 using 4000DYN recipe & 0.45 μm filter
3	Bake for 120 s at 95 °C
4	Expose for 23 s
5	Leave at room temperature for >60 min to stabilise
6	Reversal bake for 120 s at 120 °C
7	Flood exposure for 60 s
8	Development for 70 s

**Table 5.2** – Basic recipe for applying Ti35 photoresist.

Although the undercut is less than it was in Figure 5.8, it is still sufficiently good for the lift-off of magnetic electrodes. Even at reduced development times, the width of the photoresist strip is still less than the width of the feature on the mask. This is not a big problem for our purpose, as long as this behaviour is taken into account in the design for any future masks. The effect of the first exposure time on the width of the photoresist strip was also tested. Although the width did increase at longer first exposure times, the undercut of the wall disappeared. Thus, this investigation was not continued any further. The first top-gated O-FET devices were fabricated using Ti35 resist with a 45 s development time. The rest of the recipe is identical to Table 5.2.

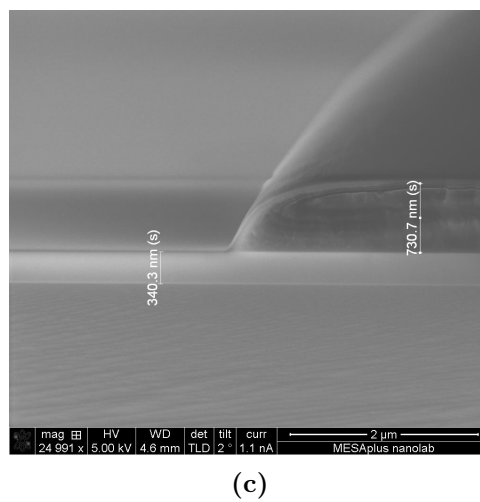
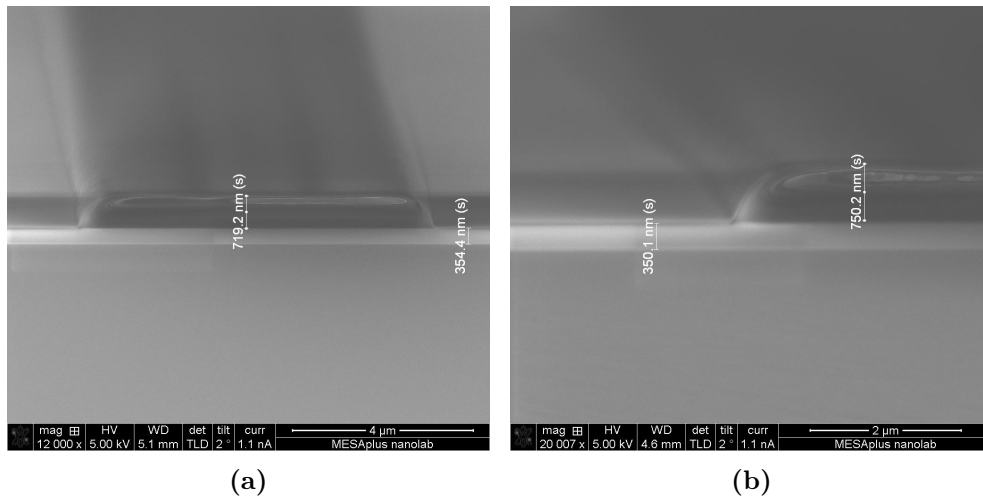


**Figure 5.7** – (a) is the SEM image of Ti09 photoresist with 40 s development time. (b) shows 50 s development time, while (c) is 60 s development time. All samples were made in the same batch. None of the photoresist layers show any undercut, even at very long development times.

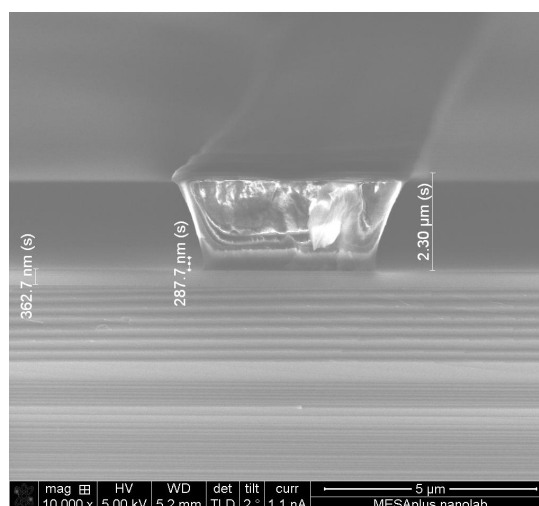
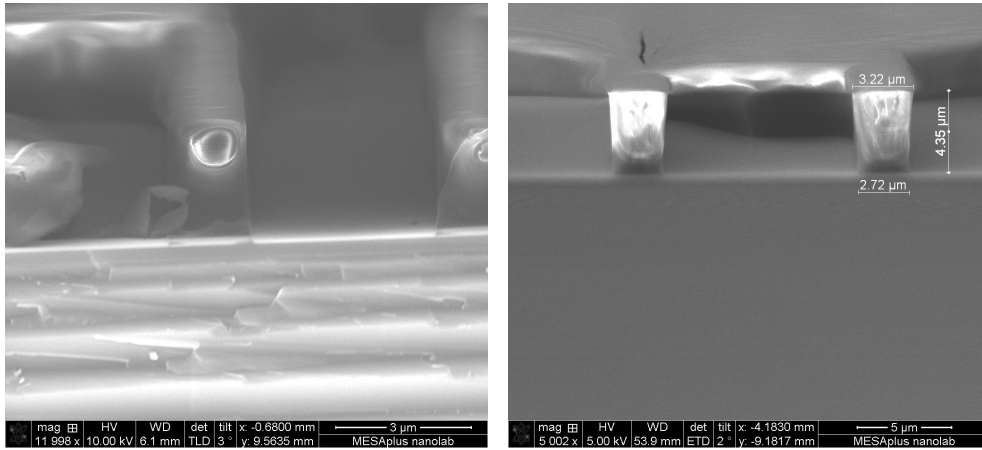
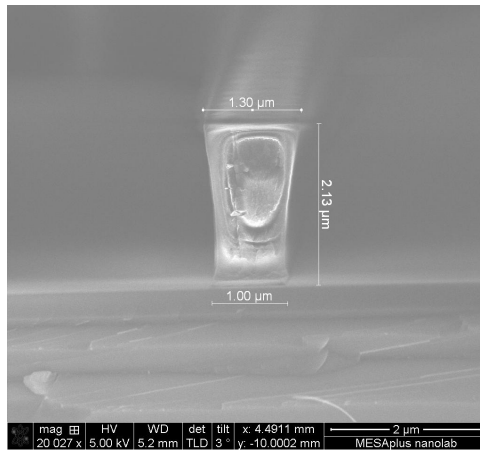


**Figure 5.8** – SEM image of the Ti35ES photoresist applied using the recipe in Table 5.2. The width of the mask feature was 9 μm, while the photoresist strip is only approximately 5 μm wide.



(a)

(b)



(c)

**Figure 5.9** – (a) is the SEM image of Ti35 photoresist with 35 s development time. (b) shows 40 s development time, while (c) is 45 s development time. Only at this development time does it show any clear undercut in the photoresist.

## 5.4 Back-gated O-FET

The work that was done on the back-gated O-FET devices can be divided in the fabrication part and the characterisation part.

### 5.4.1 Lift-off photolithography

The two ferromagnetic electrodes on the back-gated O-FET devices were made using lift-off photolithography. It is important, especially for the top-gated devices which are to be developed next, that this lift-off is successful and does not have ridges at the edge of the electrodes. For the back-gated devices, Ti09 image reversal photoresist was used. The first attempt on p-type Si/SiO<sub>2</sub> was successful, showing no ridges. AFM measurements of these electrodes are shown in Figure 5.10.

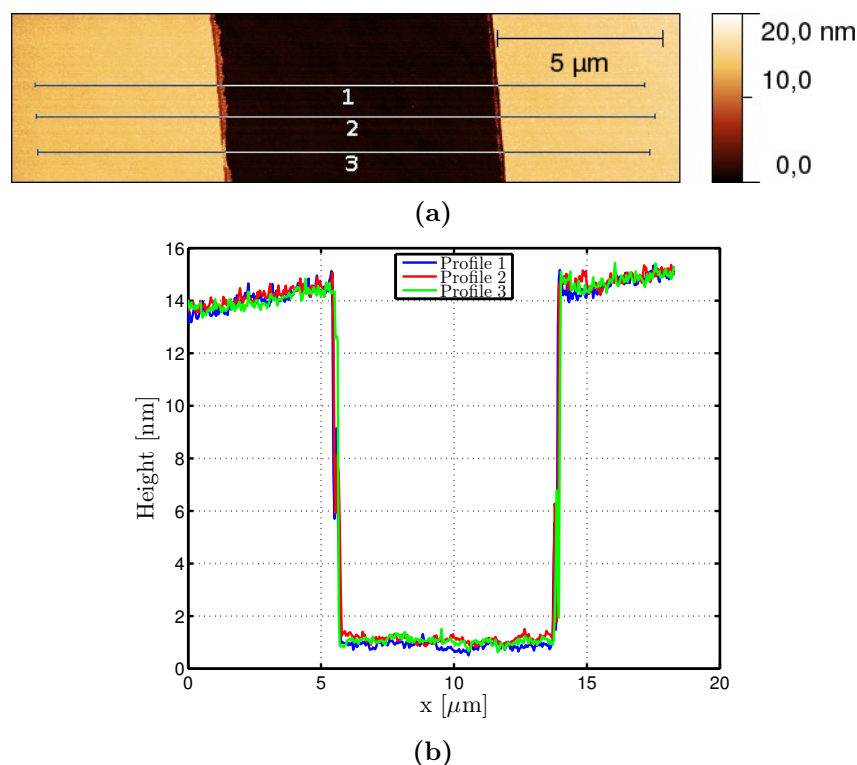


**Figure 5.10** – (a) shows the AFM height signal of the ferromagnetic electrodes on a p-type back-gated device. (b) shows the cross-sections of the channel, indicating no ridges at the edge of the contacts.

However, these results are considered lucky, since the next fabrication run (on n-type Si/SiO<sub>2</sub>) did clearly have ridges, as shown in Figure 5.11. Based on these results, a more thorough investigation of the photoresist shape was started, of which the results are discussed in Section 5.3.

Based on the results for the photoresist optimisation, the final fabrication of back-gated devices on n<sup>++</sup>-type Si/SiO<sub>2</sub> substrates was done using Ti35 image reversal resist, which exhibits a clear undercut. The AFM images are shown in Figure 5.12. These clearly show no ridges at the edge of the FM contacts, but they do show ridges just inside the channel. This is likely caused by the oxidation process. The foot of the resist has a very low contact angle with the substrate, and it is theorized that the resist at the edge of this foot hardens in the oxygen plasma environment, making it insoluble in the lift-off solvent. Indeed, measurements on the top-gated devices, where lift-off was done prior to oxidation, consistently do not show these ridges. After

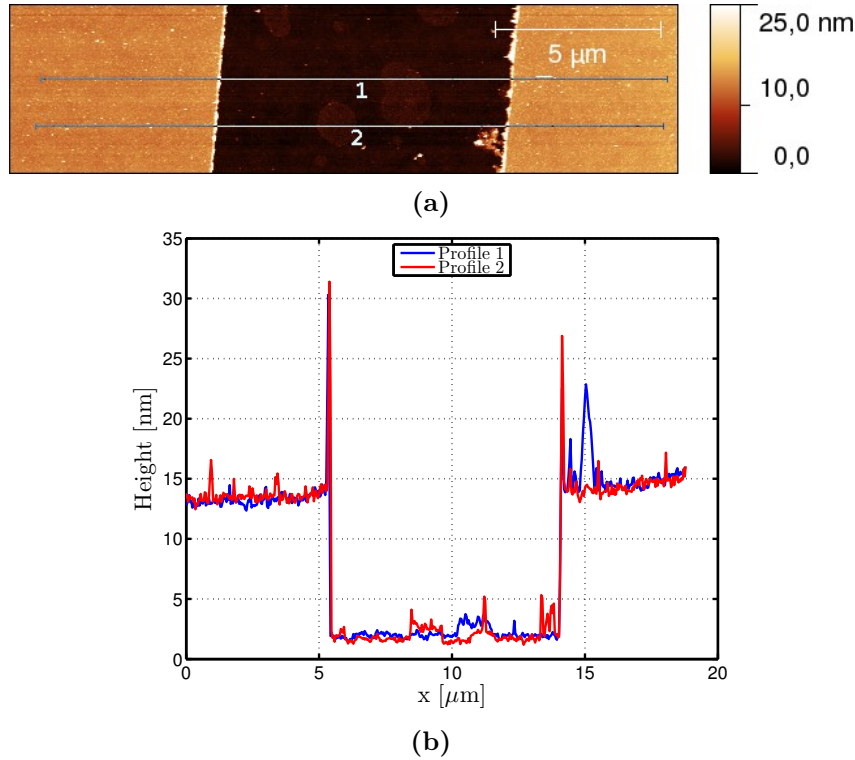


**Figure 5.11** – (a) shows the AFM height signal of the electrodes on an n-type back-gated device. (b) shows the cross-sections of the channel. This time, clear ridges are visible at the edges of the contacts.

fabrication of the magnetic electrodes using lift-off photolithography, the P3HT layer was spin-coated on top of the substrate. No further steps were necessary, as the P3HT is thin enough to directly pierce with the ultrasonic wire bonder.

#### 5.4.2 Electrical characterisation

The electrical characterisation of the back-gated O-FET devices was hampered by problems with gate leakage. Many of the structures showed high gate-drain currents, often easily hitting the compliance value of  $100\ \mu\text{A}$  set in the measurement equipment. These are likely caused by the ultrasonic wire bonder damaging the  $\text{SiO}_2$  layer during bonding.

For those structures that show no breakthrough of the gate, the resulting graphs for the p-type back-gated O-FET devices are plotted in Figure 5.13. These curves show significant gate action at negative gate voltages, but current suppression at positive gate voltages, indicating a preference to holes as charge carriers inside the P3HT. The graphs of the n-type back-gated devices are shown in Figure 5.14. From these curves, it is clear that there is a significant difference between individual transistors. For this sample, the gate leakage was significant, only approximately one order of magnitude below the source-drain current. When measuring the same structures again 13 days later, slight shifts are seen, but no major departure from previous behaviour is observed, indicating relatively good stability for the P3HT layer. Shown in Figure 5.15 are the results for the  $n^{++}$ -type back-gated devices. These show relatively low gate leakage currents, although there is still a significant spread in the  $IV$ -characteristics of individual transistors. Although the  $IV$ -characteristics show no sign of saturation, the current can no longer be described as purely a space-charge limited current, unlike the p-type back-gated O-FET shown in Figure 5.13(a).

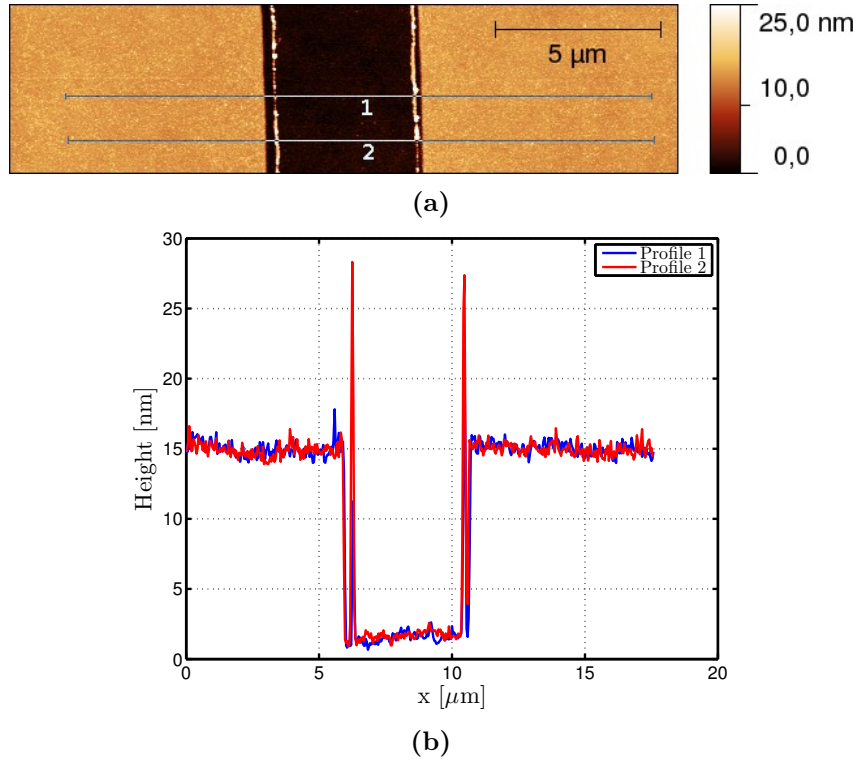


**Figure 5.12** – (a) shows the AFM height signal of an n++-type back-gated O-FET device after deposition and lift-off of the Co/ $\text{AlO}_x$  electrodes. There are clear ridges visible just inside the channel. (b) shows the cross-sections of the channel.

These devices cannot be directly compared, since not only the doping of the substrate was varied, but also the anneal times of the P3HT layer and the distance between the electrodes. The electrode distance changed because it is not only dependent on the mask that is used, but also on the precise photoresist and recipe for applying that photoresist. In Figure 5.6 the width of the photoresist strip in the back-gated pattern is shown as a function of the development time of the Ti09 resist. The result of these variations, and of the change in lift-off resist from Ti09 to Ti35, is that the channel length of the n++-type back-gated O-FETs is shorter (approximately  $5 \mu\text{m}$ ) than the n-type and p-type back-gated devices (both approximately  $9 \mu\text{m}$ ). The Ti35 resist used for the n++-type devices behaved very different during first exposure and development, resulting in more resist being stripped, and shorter channel lengths as a result.

An additional result obtained from these back-gated devices is the degree of planerisation of the P3HT on top of the ferromagnetic electrodes structure. Based on AFM measurements, shown in Figure 5.16, it is clear that the thickness of the P3HT inside the channel is the same as the thickness on top of the electrodes. Thus, the P3HT follows the surface topography quite accurately.

#### *IV* asymmetry

It is clear from all these graphs that a significant asymmetry exists for positive and negative drain voltages. There are two main reasons for this. The first reason is the fact that both gate and drain voltages are defined with respect to ground and that the source is grounded, as shown in Figure 2.1. This means that at a particular gate voltage (say  $V_g = -50 \text{ V}$ ), the electrical field inside the P3HT is much larger when the drain has opposite polarity (in this case when  $V_d = +60 \text{ V}$ ) compared to a drain voltage of the same polarity. This induces more charge

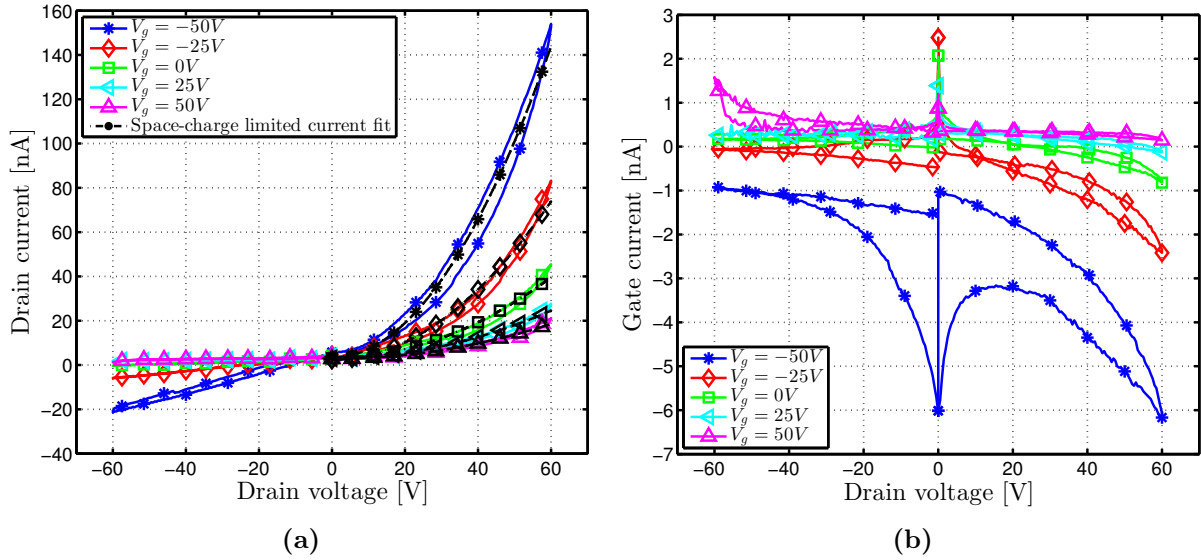


**Figure 5.13** – (a) shows  $IV$  curves (drain current versus drain voltage) of a p-type back-gated O-FET at different gate voltages. At positive drain voltages, a clear space-charge limited current is seen, with the black lines being a least-squares fit of Equation (2.6) to the data at positive  $V_d$ . (b) is the gate leakage versus drain voltage at different gate voltages, for the same device.

carriers, resulting in an increased current.

The second major contribution is the fact that the predominant charge carriers inside P3HT are positively charged holes, see Chapter 2. Thus, the conduction channel induced by the field-effect is much stronger at negative gate voltages. This, combined with the difference in electrical field strength at different polarities of the gate and drain electrodes, explains why the current is largest when both the drain voltage is positive and the gate voltage is negative.

### Space-charge limited current

It is clear from all the graphs that the  $IV$  curves for the back-gated O-FET devices do not exhibit any saturation. Rather, the current appears to behave quadratically when the drain voltage is positive, and linearly when the drain voltage is negative. For positive drain voltages, this behaviour is very similar to that of an organic light emitting diode. Fitting these parts of the data to Equation (2.6) shows a good match for the p-type back-gated O-FET devices. However, the match is poor for the n++-type back-gated O-FET devices, where the current increases faster than quadratically.

This space-charge limited current is more thoroughly explained in Section 2.2, and indicate that the current through the P3HT is mainly limited by the electrostatic repulsion of already present charge carriers, and that the gate voltage is only of secondary importance.

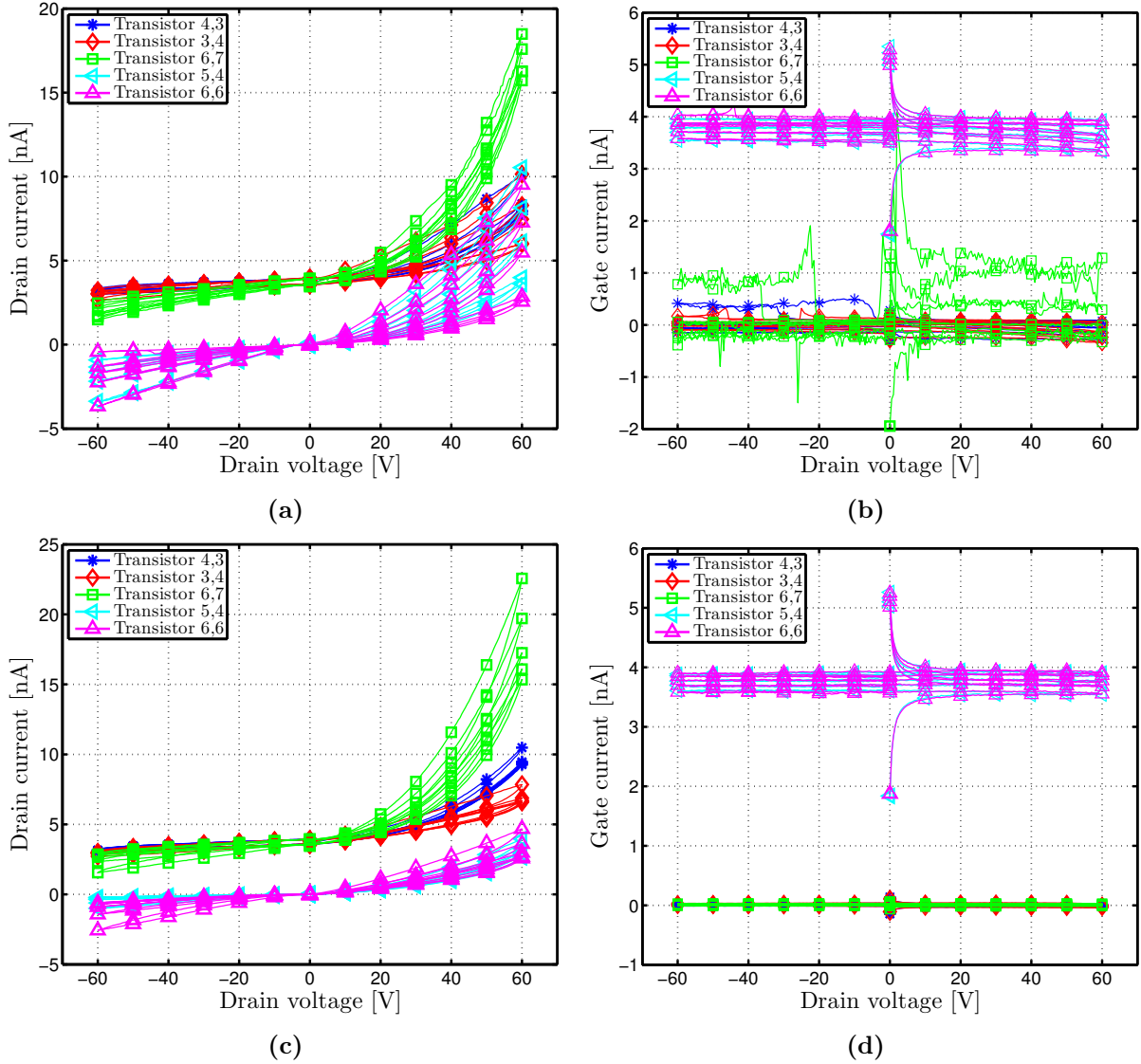


**Figure 5.14** – (a) shows  $IV$  curves of n-type back-gated O-FETs. Different devices on the same sample are plotted, with different gate voltages plotted in the same colour. (b) shows the gate leakage currents of the different transistor devices on the same n-type back-gated O-FETs. (c) and (d) are the  $IV$  curves and gate leakage currents of the same transistor structures measured in the same way 13 days later.

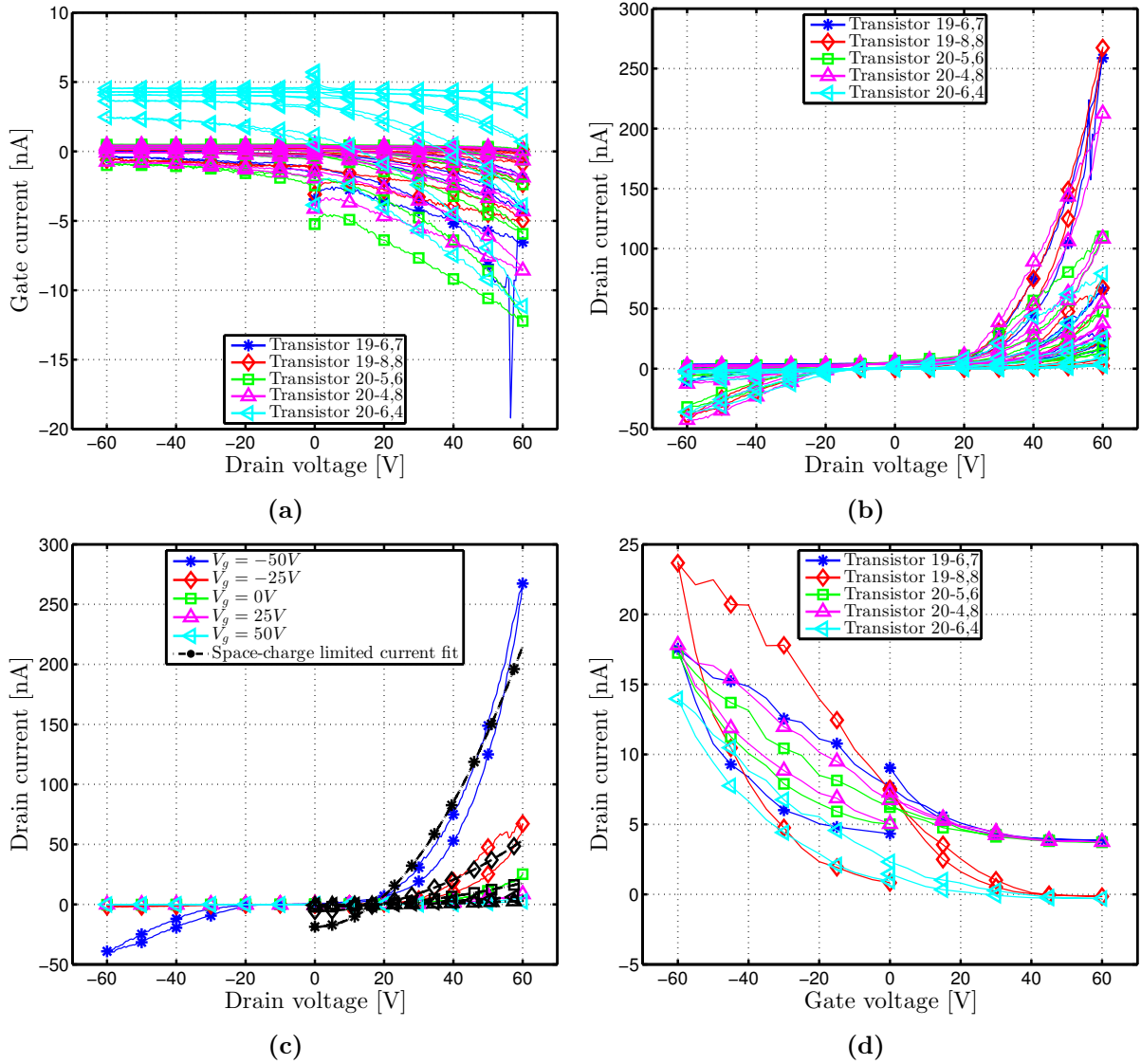


**Figure 5.15** – (a) are the gate leakage curves of five n++-type back-gated O-FETs. (b) shows the  $IV$  curves of the same five back-gated O-FETs. (c) shows the  $IV$  curves of the single best back-gated O-FET measured on highly doped n-type substrates. The space-charge limited current best fit (Equation (2.6)) is also plotted. (d) are the transfer curves of the same five back-gated O-FETs, measured at a drain bias of 20 V.

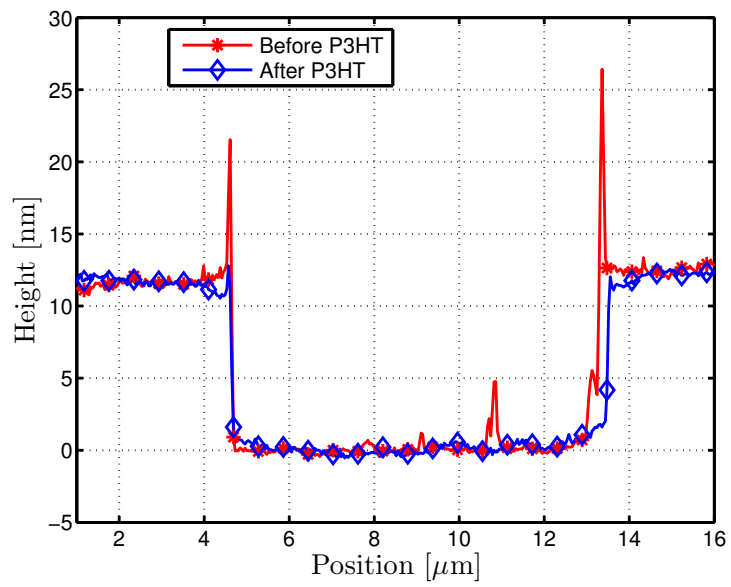


**Figure 5.16** – Comparison of AFM channel cross-sections before and after P3HT spin-coating. Measurements were made on an n-type Si/SiO<sub>2</sub> substrate using the back-gated geometry. Both cross-sections are zeroed inside the channel.

## 5.5 Top-gated O-FET

As with the back-gated O-FET devices, the results for the top-gated O-FET devices are separated into two parts. The fabrication process is the most important part, while only preliminary electrical characterisation measurements were performed.

### 5.5.1 Device fabrication procedure

The first top-gated O-FET devices are fabricated using a simplified version of the recipe described in Appendix A.1. For these devices, the electrodes and contact pads were both fabricated using a layer of 40 nm of Pt, deposited using the DCA, on top of a 5 nm Ti adhesion layer, deposited in Sputterke. These structures were patterned using Ti35 photoresist, and lift-off was done using DMSO as solvent. AFM measurements were made to investigate the quality of the lift-off, as shown in Figure 5.17. These AFM images show a clear plateau approximately 5 nm above the substrate, with ridges inside the channel.

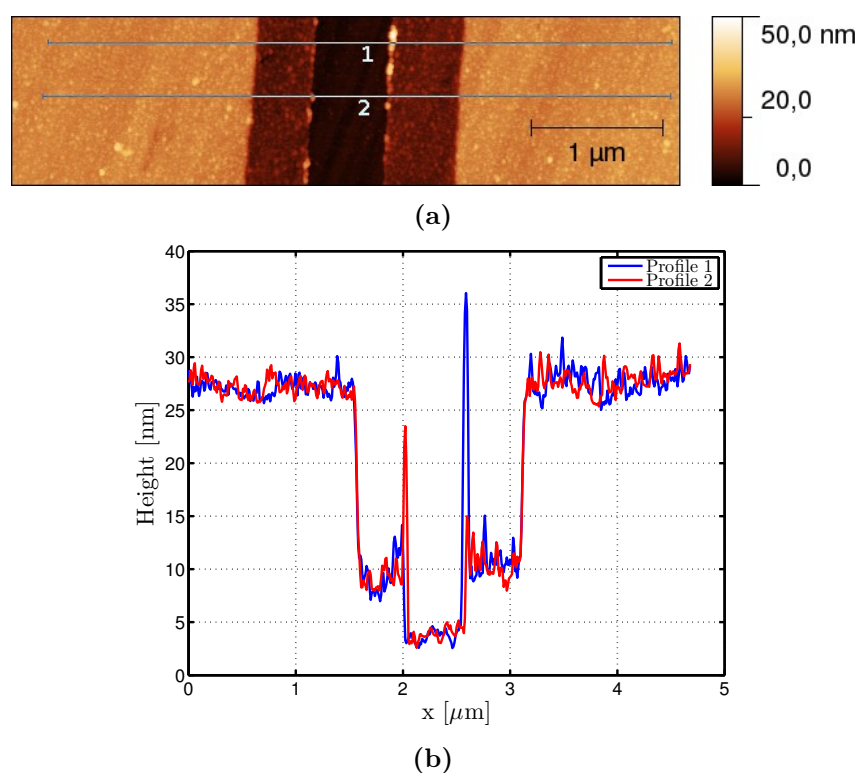


**Figure 5.17** – (a) is the AFM height signal of the top-gated O-FET devices with Pt electrodes. (b) shows the cross-sections of this channel. The electrodes are a double layer composed of a 5 nm Ti adhesion layer and a 40 nm (by DCA calibration) Pt layer.

This result is due to the two different methods used to grow the two layers. The DCA deposits the Pt directionally, which corresponds to the outer step edges. Because of the directionality of the deposition and the undercut of the Ti35 photoresist, no ridges form on this layer, see Figure 5.18(a). However, the Ti layer is deposited non-directionally in Sputterke, and coats the walls and foot of the photoresist in addition to the channels, see Figure 5.18(b). Because the contact angle of the photoresist with the substrate is very low, this results in the formation of ridges during lift-off.

After the deposition of the Pt electrodes and contact pads, P3HT was coated at 3000 rpm. According to Figure 5.4, this yields a final thickness of approximately 25-30 nm, in accordance

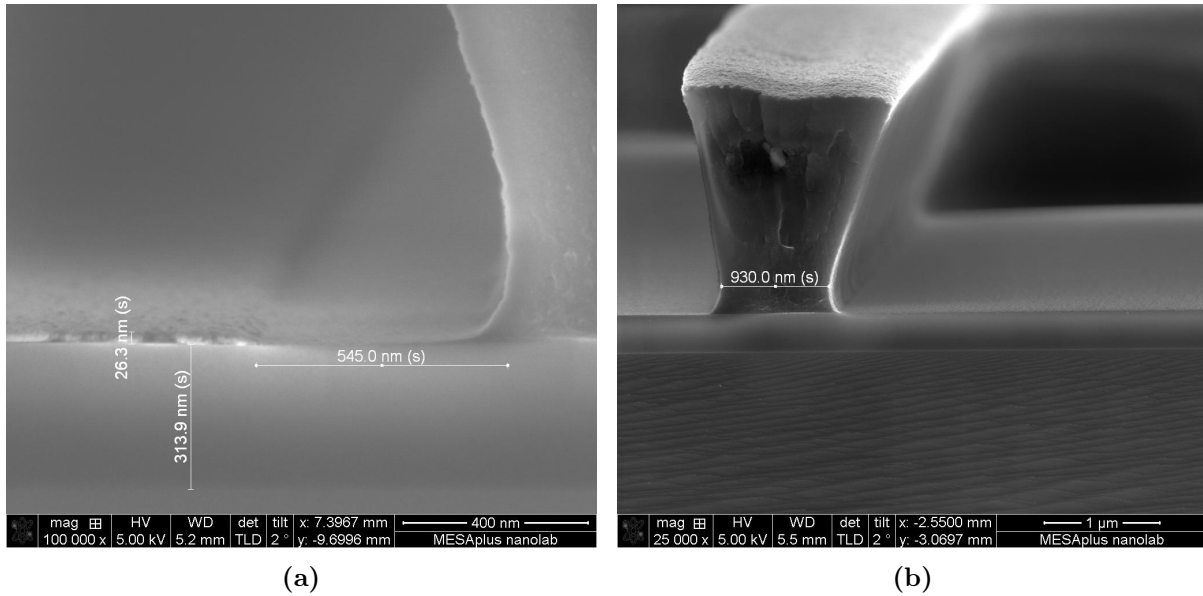


**Figure 5.18** – (a) is a SEM image of a Ti35 image reversal photoresist with a layer of Pt deposited using the DCA. (b) is a SEM image of a Ti35 image reversal photoresist with a 5 nm Ti layer deposited using Sputterke. The high contrast at the wall of the photoresist indicates that a metallic layer is present there as well.

with the thickness of the Pt electrodes measured in Figure 5.17. The samples were then annealed at 90 °C for 60 min, to ensure all the solvent has evaporated.

Next, a parylene layer was deposited on the samples in the parylene coater<sup>13</sup>. The amount of precursor material used was 320 mg, which should yield a layer thickness of approximately 200 nm. However, AFM measurements on the dummy substrates included indicate a parylene thickness of 270 nm. Thus, it is important to include dummy substrates for both P3HT spin-coating and parylene coating. These dummy substrates can be used to determine the thickness and to test the etch rate during the later RIBE step.

The Au top-gate on these devices is deposited using Sputterke, after coating of the parylene layer. Before depositing the gate layer, small drops of 907-17 photoresist were applied to the corners of the samples, to cover the markers. After depositing 5 nm of Cr adhesion layer and 50 nm of Au top-gate layer, lift-off of the markers was done in acetone at the highest ultrasonic power. This process ensured the markers were not covered with gold, which improved their visibility in the mask aligner. This made alignment of the photoresist for gate etching much easier. After 907-17 photoresist was applied using the gate electrode mask, etching was carried out using the standard gold-etch and chromium-etch chemicals available. The gold-etch etched faster than normal, with the layer being etched away in just 45 s. Cr etching was difficult because of the low contrast. It is hard to see if the Cr layer is completely etched, or if some is still remaining. Thus, it may be useful to investigate whether the Au layer has enough adhesion to the parylene by itself. If this is the case, then the Cr adhesion layer can be left out and this etching step becomes easier and quicker.

After gold etching, the photoresist that was used as an etch-mask was washed away, and new photoresist was applied. This new photoresist is used as an etch-mask for the organic etch step, and completely covers the gate electrodes. Previous results by Liang Du indicate an etch rate of  $1.07 \text{ nm s}^{-1}$  for parylene when using RIBE. Etching for 180 s on a dummy sample, followed by AFM measurements of the remaining thickness, indicate approximately 170 nm has been etched,

<sup>13</sup> Many thanks to Bojian Xu for operating the parylene coater.

giving an etch rate of  $0.95 \text{ nm s}^{-1}$ . The etch rate of P3HT in RIBE has not been tested, but it is assumed to be similar to the etch rate of parylene. The top-gate samples were etched for 5 min and 15 s in total. The completed device is shown in Figure 5.19.

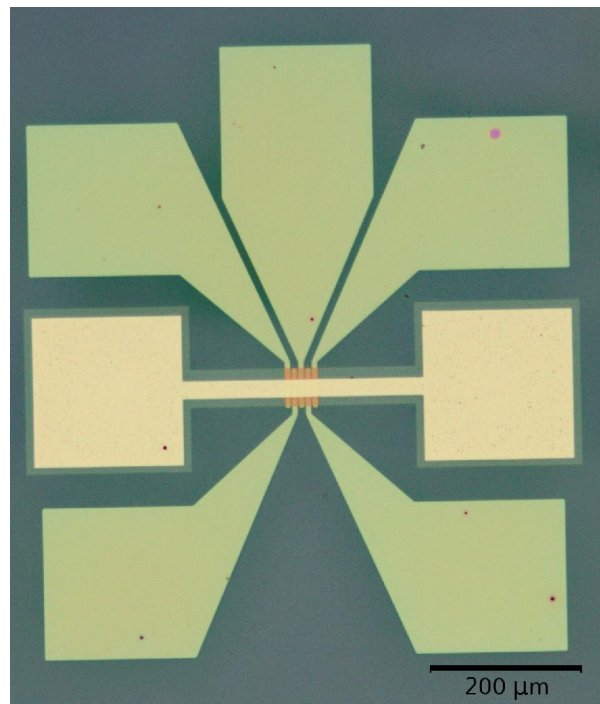


**Figure 5.19** – Microscopy image of a completed top-gated O-FET device. Each substrate of 11 mm by 11 mm contains 80 such devices.

However, AFM measurements (see Figure 5.20) indicate that the organic layer is not yet fully removed by the RIBE step. The top-right area of Figure 5.20(a) should be free of organic material, since that was not covered by photoresist during the RIBE step. The cross-sections shown in Figure 5.20(b) show that the RIBE step only removed approximately 30 nm of organic material. This gives problems with properly bonding wires to the contact pads for electrical measurements. It is possible that the etch rate in the RIBE machine is highly variable. In addition, the organic layer thickness is much larger than expected. This may be caused by non-uniform deposition of parylene or P3HT. Further experiments are needed to learn more.

### Ferromagnetic electrodes

Previous results on back-gated O-FET devices indicate ridges inside the channel after lift-off of  $\text{Co}/\text{AlO}_x$  deposited in the DCA, see Figure 5.12. Since the deposition of both cobalt and aluminium is highly directional, and Ti35 photoresist was used with a good undercut, these ridges are unexpected. A likely cause is the hardening of the Ti35 photoresist in the oxygen plasma used to oxidise the aluminium layer to  $\text{AlO}_x$ . The contact angle of this resist with the substrate is very low at the bottom, resulting in a thin area there, see Figure 5.18(a). If this resist hardens to the point where it is insoluble in DMSO or acetone, it could cause the ridges that are observed in AFM measurements.

To prevent this, the order of oxidation and lift-off was switched. Since oxidation is meant to oxidise the deeper aluminium, it is not a problem to take the samples out of the DCA for lift-off, before loading them again to do the oxidation. This resulted in very nice electrode edges and clear channels, as shown in Figure 5.21.

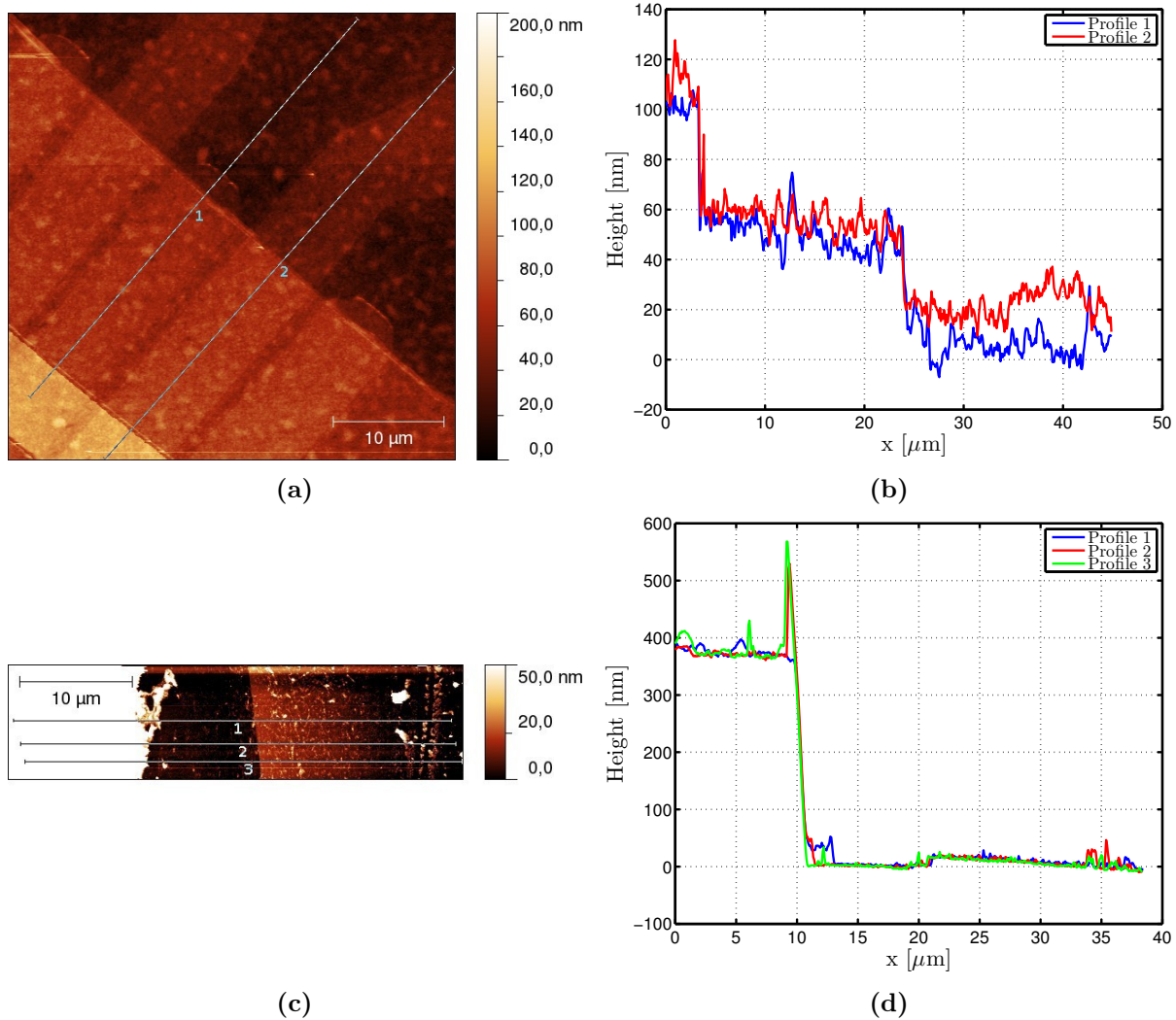
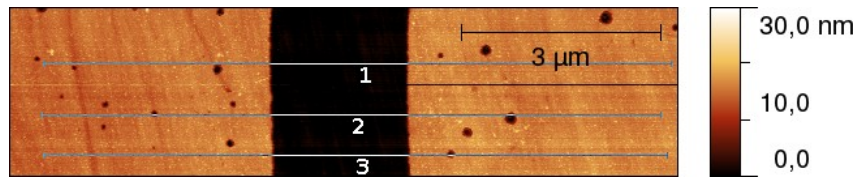


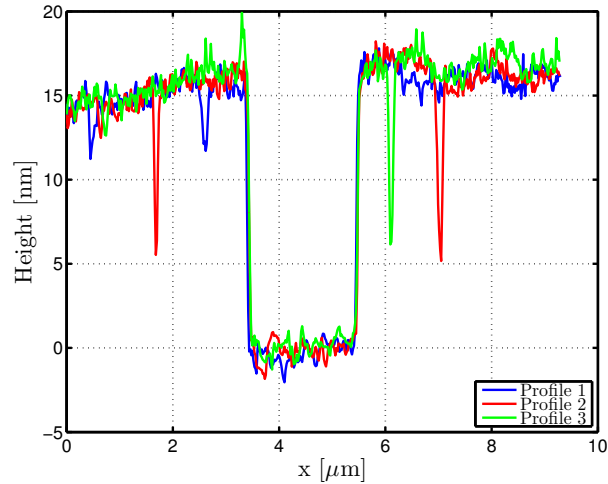
**Figure 5.20** – (a) is the AFM height signal of a top-gated structure using Pt for both contact pads and electrodes. Visible in the bottom-left is the gold top-gate electrode. (b) shows the cross-sections of the sample. (c) is the AFM height signal of a channel scratched over a Pt contact pad using a metal tweezer. The z-scale is adjusted to show the Pt contact pad clearly. (d) are the cross-sections of the sample, indicating a total organic layer thickness of approximately 370 nm.

A second problem became very apparent after contact pads were patterned on the samples, also using lift-off photolithography. After this second lift-off, the electrodes look very damaged and clearly do not make contact any more with the contact pads, see Figure 5.22. Not only is the contact lost, but the  $\text{AlO}_x$  tunnel barrier is also clearly etched away.

To find out the reason for this etching, lift-off was tried with different solvents. Shown in Figure 5.23 are the AFM and dark field microscopy results for lift-off using acetone and for lift-off using DMSO. Both lift-off procedures were done at elevated temperatures of 60-70 °C. Lift-off using DMSO at room temperature was not tried. Lift-off using acetone at room temperature works well. The lack of any scattering on the  $\text{Co}/\text{AlO}_x$  electrode in Figure 5.23(b) indicates a very smooth surface. The edges are approximately 15 nm high and show up brightly. From these results, it is very clear that the DMSO contributes significantly to the damage. Switching back to acetone as the lift-off solvent appears to solve the problem. These tests also indicate that lift-off of Ti35 with acetone does work, likely because of the large uncovered area of resist



(a)



(b)

**Figure 5.21** – (a) shows the AFM height signal of a  $\text{Co}/\text{AlO}_x$  electrode where lift-off was done before oxidation of the aluminium layer. (b) are the corresponding cross-sections. The ridges visible inside the channel in Figure 5.12 are not observed here, indicating that switching the order of oxidation and lift-off in the recipe works.

on the sides of the resist layer. This allows the acetone to etch away the photoresist cleanly.

Although acetone lift-off greatly decreases the etching of the ferromagnetic electrodes, it is not completely gone. Shown in Figure 5.24(a) is an AFM height signal of a ferromagnetic electrode after Pt contact pads were fabricated using lift-off. Some small etch marks are still visible, even though both lift-off steps on this sample were performed using acetone as the solvent. There is also some dirt visible inside the channel, shown in Figure 5.24(b). This dirt appears to be restricted to the places where the photoresist did not make direct contact with the substrate. However, the contact between the contact pads and the electrodes does look good when using just acetone as the lift-off solvent, as shown in Figure 5.24(c).

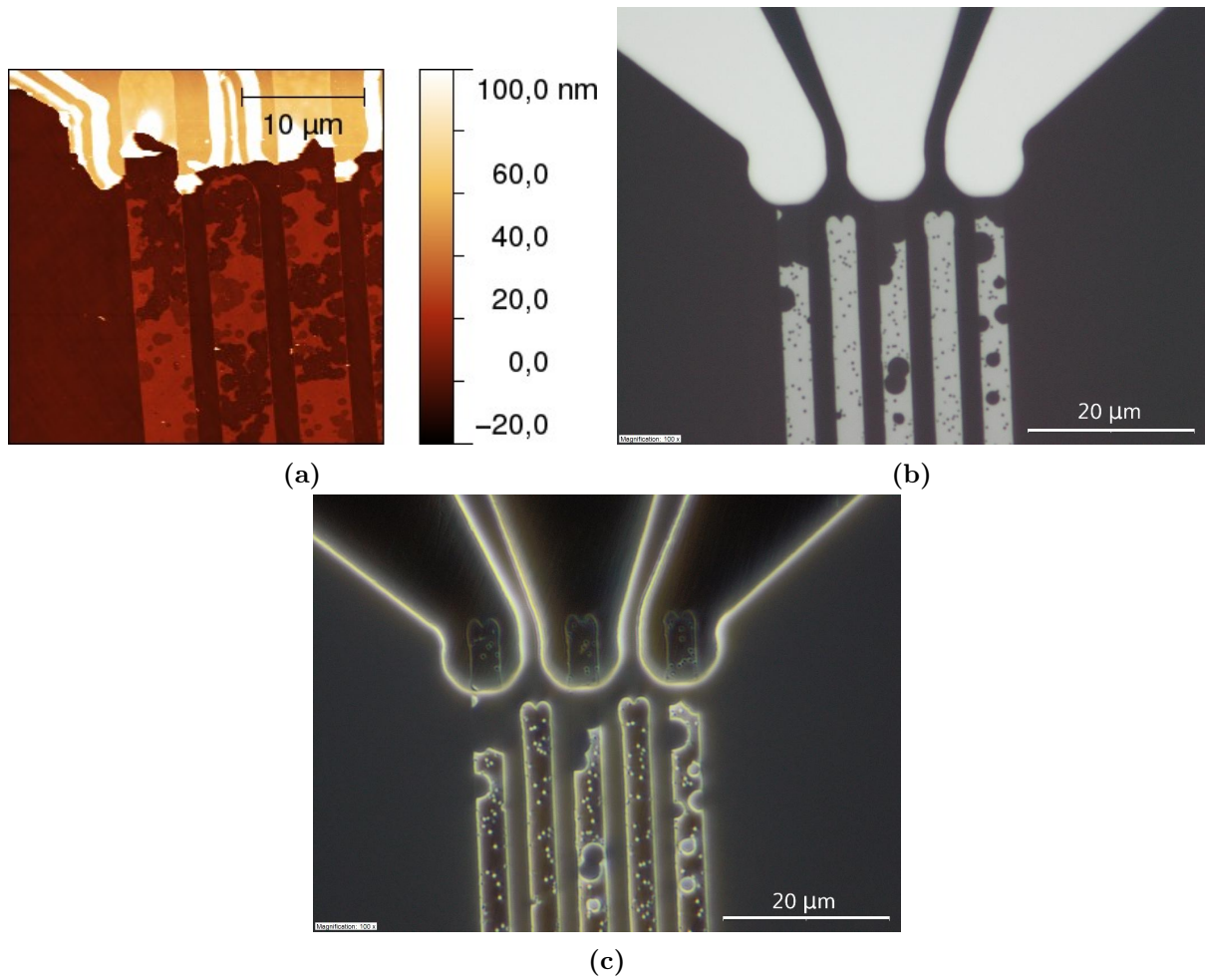


**Figure 5.22** – (a) shows the AFM height signal of the patterned  $\text{Co}/\text{AlO}_x$  electrodes, which are heavily etched by the DMSO lift-off solvent. (b) shows a microscopy bright field image of the same. (c) is the corresponding dark field image.

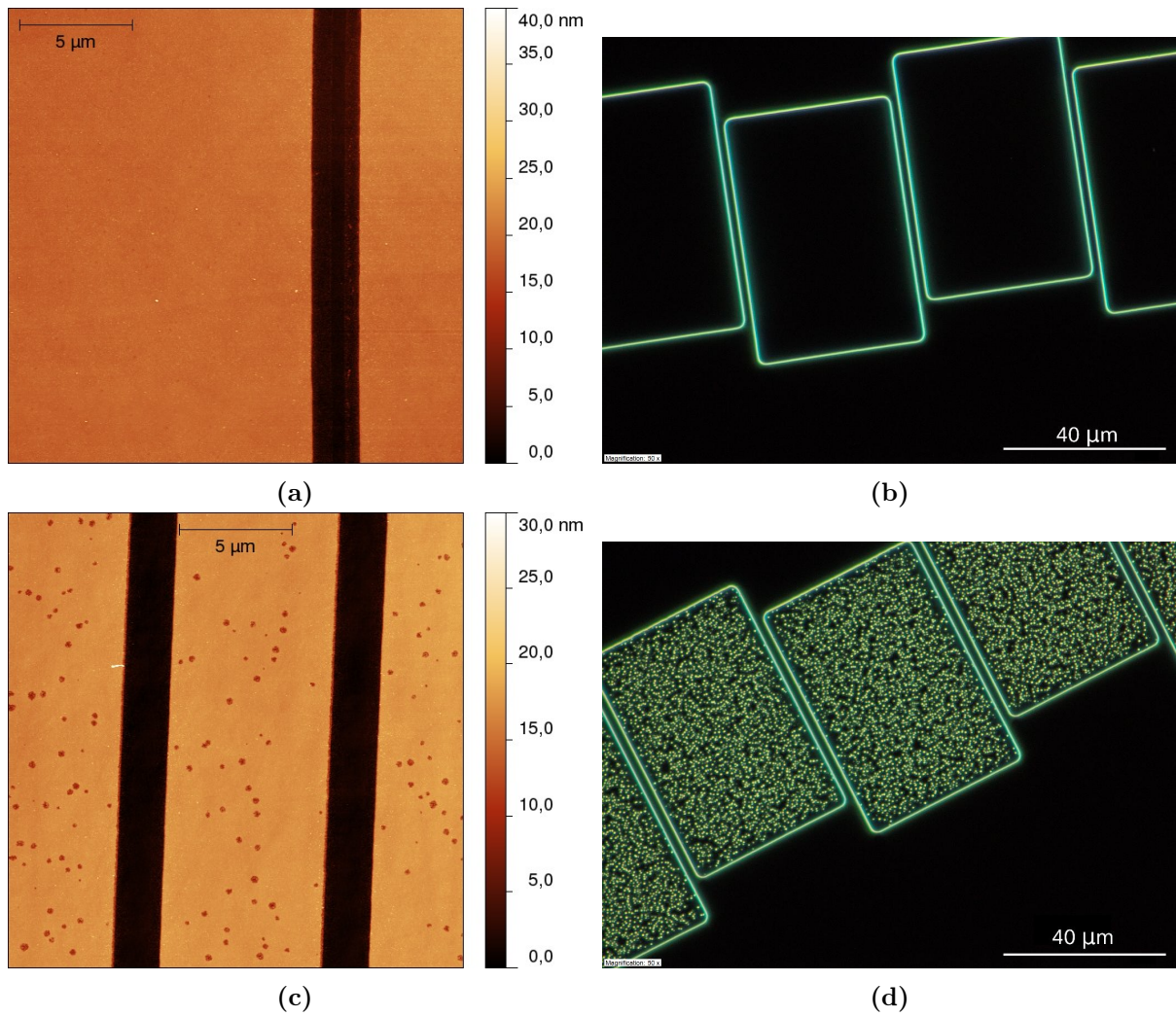


**Figure 5.23** – (a) is the AFM height signal of a  $\text{Co}/\text{AlO}_x$  electrode where acetone was used as lift-off solvent. (b) is the corresponding dark field microscopy image. (c) is the AFM height signal of a  $\text{Co}/\text{AlO}_x$  electrode where DMSO was the lift-off solvent. (d) is a corresponding dark field microscopy image.

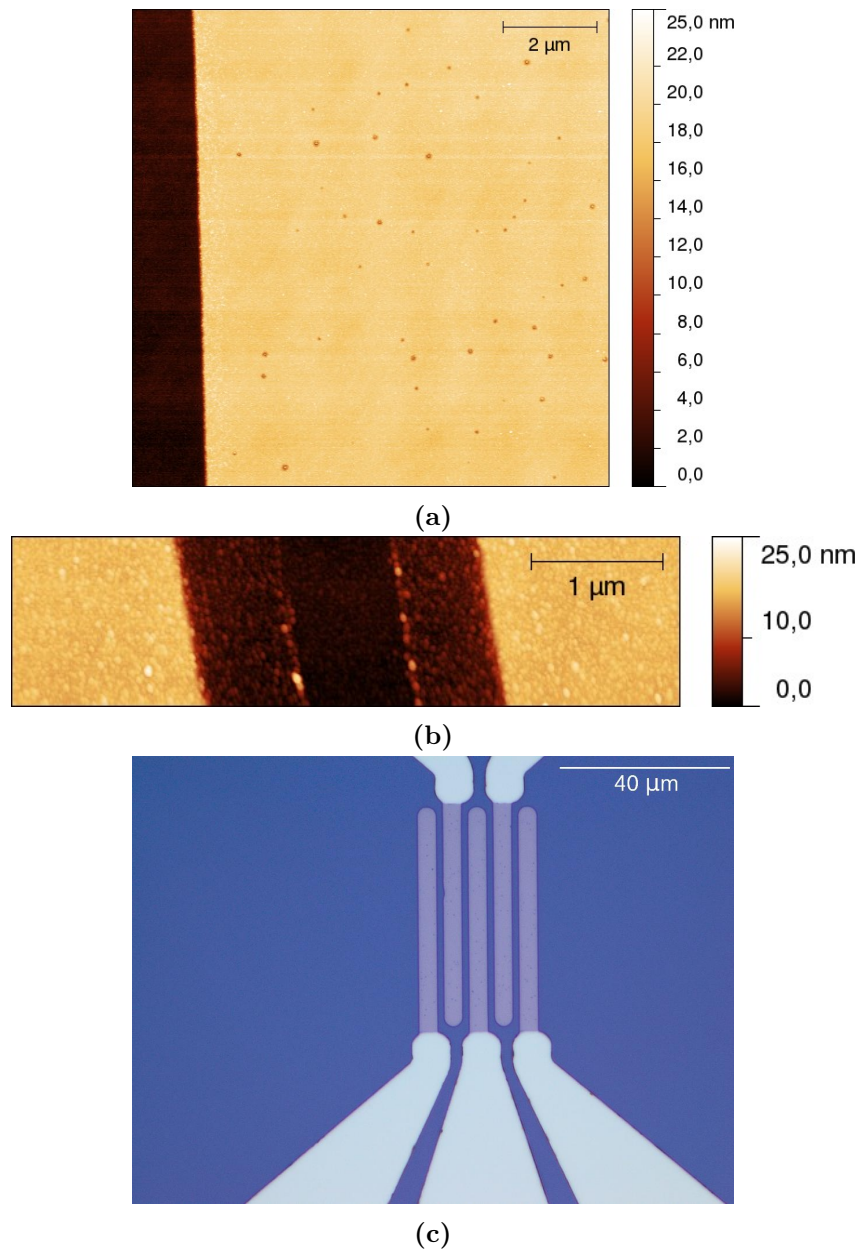


**Figure 5.24** – (a) shows the AFM height signal of a Co/AlO<sub>x</sub> electrode after lift-off of contact pads using acetone. (b) shows an AFM height signal of the channel between two electrodes. Some dirt is still observed in the sides of the channel. (c) is a bright field microscopy image of the contact pads on Co/AlO<sub>x</sub> electrodes, showing a good contact between the electrodes and contact pads when using acetone as the lift-off solvent.

## 5.5.2 Electrical characterisation

The top-gated O-FET devices with Pt electrodes were measured in the Bruker system, using two Keithley 2400 source-meters. These preliminary electrical results shows a higher drain current than seen in the back-gated O-FET devices. This is expected, since the electrodes are much closer together in the top-gated devices compared to the back-gated devices. The distance is approximately  $1.5\ \mu\text{m}$  and  $5\ \mu\text{m}$  respectively. Measurements at low  $V_d$  and low  $V_g$  show little gate action, and a clear hysteresis in the current, see Figure 5.25. For slightly higher voltages, the asymmetry also observed in the back-gated O-FET devices is seen. Since all the reasons discussed in Section 5.4.2 are still present, this asymmetry is expected. However, for this structure, and in fact for all top-gated O-FET structures measured, the drain current dropped to only a few  $\mu\text{A}$  and started to behave erratically when the drain voltage was increased to  $60\ \text{V}$ . The gate current was not affected, indicating that the cause is not a short circuit between the gate and the source or drain contacts.

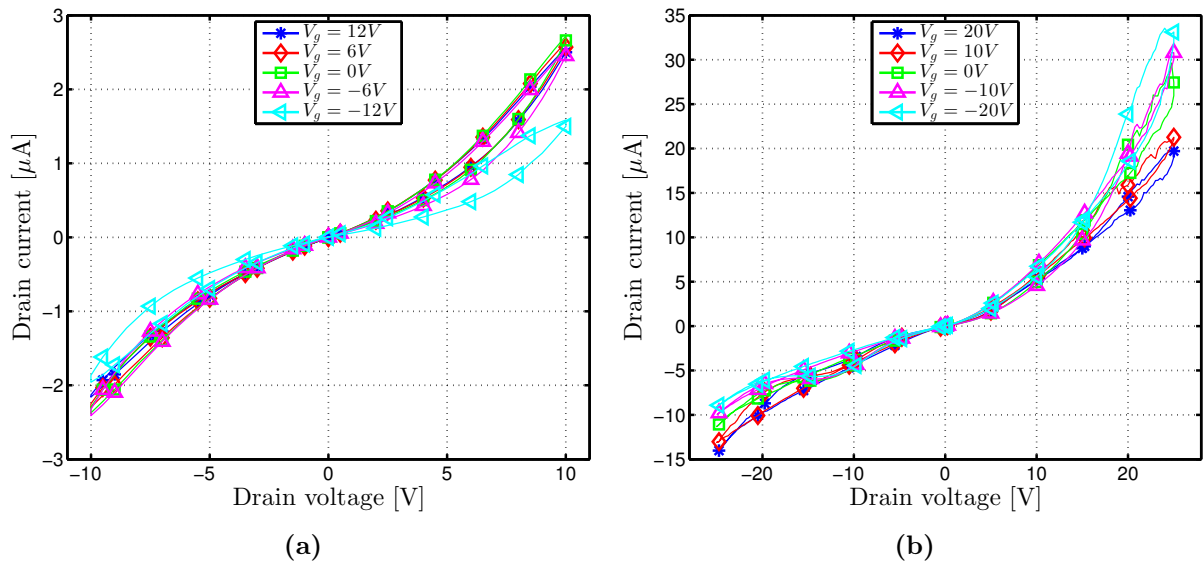


**Figure 5.25** – (a) are the  $IV$  curves of structure E3 on sample #1, measured with  $V_d$  going up to  $10\ \text{V}$  and  $V_g$  going up to  $12\ \text{V}$ . (b) shows  $IV$  curves on the same structure, now with  $V_d$  going up to  $25\ \text{V}$  and  $V_g$  going up to  $20\ \text{V}$ .

The erratic behaviour of the drain current in the structures at higher voltages is not due to the increased gate voltage, but rather due to the increased drain voltage. Measurements done at high gate voltages (up to  $50\ \text{V}$ ) but lower drain voltages do not show any erratic behaviour. The hysteresis is also examined more closely by performing these measurements in a slow fashion and comparing them to a fast measurement, see Figure 5.26. From these measurements, it is clear that the gate action (to the extent that it was present in the slow measurement) is much reduced in the fast measurement, indicating that this behaviour is more likely caused by some sort of degradation of the sample, or that the gate is charged very slowly.

To test the device stability over time, a fixed gate and drain bias were applied, and the current was measured overnight. Again, these are preliminary measurements, with only two devices measured. The first device, shown in Figure 5.27, show a very interesting two-level stabilisation of the current. No degradation takes place in this device, but the current switched between two levels, both equally preferred. The current is plotted over time in Figure 5.27(a), while the cross-correlation between the drain current and the gate current is plotted in Figure 5.27(b). The strong negative peak in the cross-correlation at zero lag indicates that the gate current is

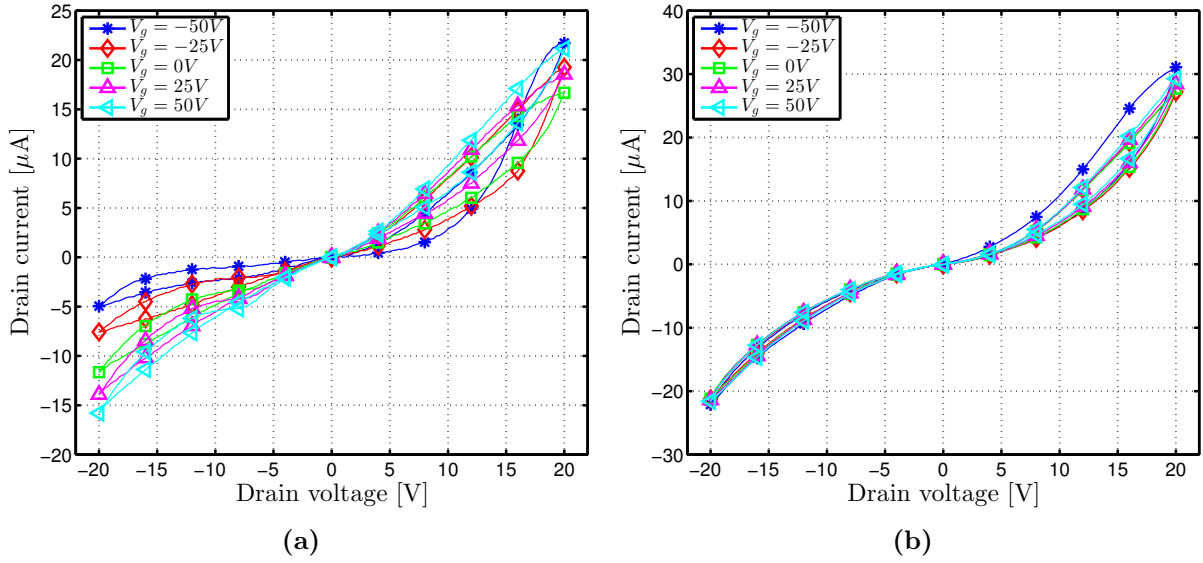


**Figure 5.26** – (a) shows the  $IV$  curves of structure C3 on sample #4. The drain voltage goes up to 20 V, while the gate voltage goes up to 50 V. These curves were measured using the normal measurement speed. (b) shows the exact same  $IV$  curves measurement, but now measured at a very fast measurement speed. Nearly all gate action disappeared, and the size of the hysteresis loops are also somewhat smaller. When performing a very fast measurement, the measurement software skips the direct plotting and keeps the data in its memory instead of writing it directly to the disk. No changes are made in the stabilisation and averaging settings when performing a fast measurement.

preferentially negative when the drain current is in the highest level, while the gate current is preferentially positive when the drain current is in the lowest level. This indicates that gate leakage effects play a role in this behaviour.

The second device measured in this way shows normal degradation, although some variations are observed where the current temporarily increases again. In general, the current degrades approximately exponential, as shown in Figure 5.28.

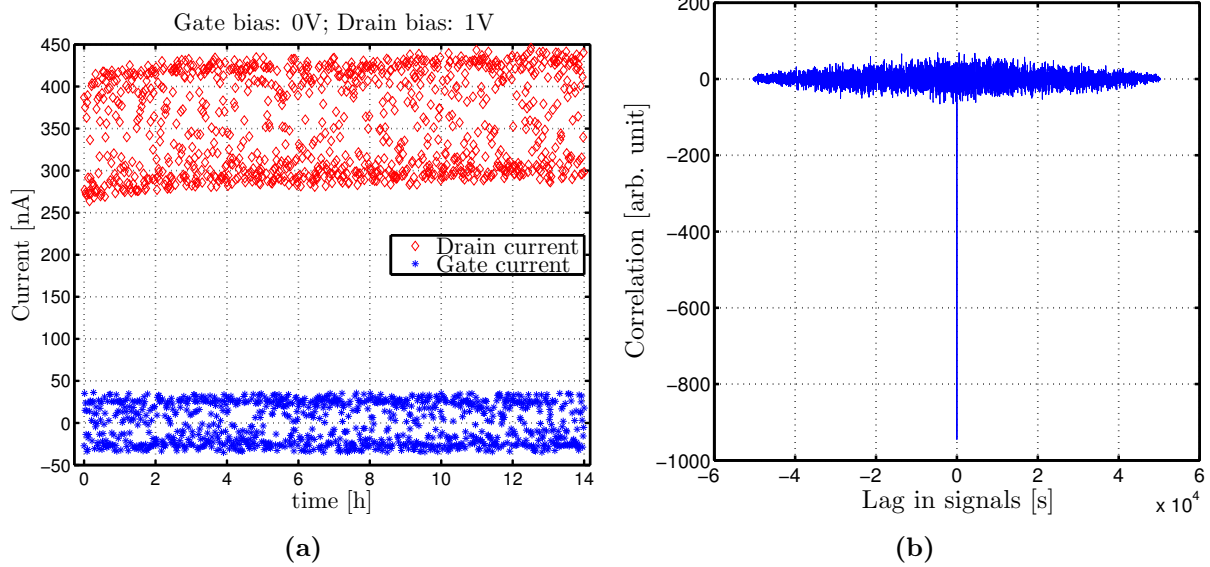


**Figure 5.27** – (a) shows every fiftieth data-point of the I-time measurement on structure D5 of sample #1. Plotted in red (diamonds) is the drain current, while plotted in blue (asterix) is the gate current. (b) shows the cross-correlation between the drain current and the gate current, with the DC offset in both signals removed.

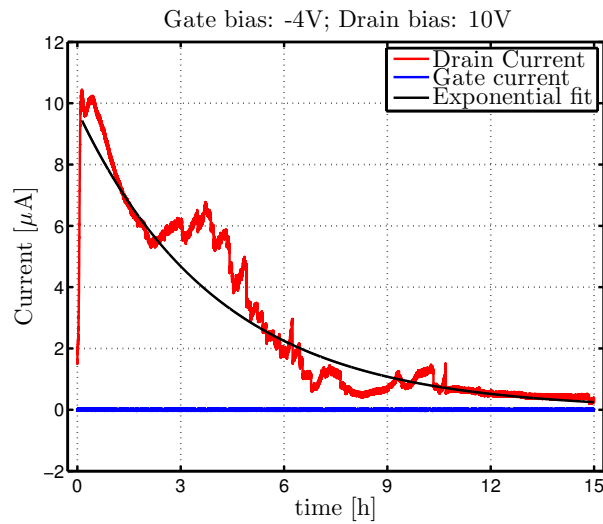


**Figure 5.28** – The decay of the drain current over time in the top-gated O-FET structure E1 on sample #2. The black line is the best fit of  $I = Ae^{\lambda t}$  to the drain current.

# Chapter 6

## Conclusion

In conclusion, much progress has been made during this masters assignment towards the goal of measuring spin accumulation in organic materials. However, this goal is clearly not yet reached and work on the project must continue. Preliminary electrical measurements have been made on back-gated O-FET devices as well as on top-gated O-FET devices, but neither measurements use spintronic effects.

Most of the progress has been made on the fabrication recipe to realise such devices. Lift-off photolithography has been extensively tested and optimised, and is shown in Figure 5.24 to result in high quality electrodes without ridges. This has been achieved by utilising an image reversal photoresist with a high aspect-ratio undercut, shown in Figure 5.8 and Figure 5.18. A serious problem with chemical etching of the Co/AlO<sub>x</sub> electrodes has been solved by changing the DMSO lift-off solvent to the less corrosive acetone, the results of which are shown in Figure 5.23.

In addition to the lift-off steps of the fabrication recipe, the organic spin-coating step has also been extensively tested. A suitable solvent (1,2-dichlorobenzene) has been selected for the P3HT and the spin-coating recipe has been tested and optimised for the available equipment. With this process in hand, it is very easy to switch organic materials if desired. The only constraint on such a selection is that the material is soluble in a solvent that does not degrade the Co/AlO<sub>x</sub> electrodes in any significant way, and that the solvent is allowed for use in the MESA+ cleanroom.

### 6.1 Recommendations

Because this project is clearly not yet finished, there are many recommendations and interesting avenues to explore in support of reaching the goal of spin accumulation measurements in organic materials. In addition to a host of smaller recommendations, there are three main points which are essential to address in the development of a magnetic top-gated O-FET device.

1. The most important next step in the development of the fabrication recipe is the solution to the remaining etch-marks in Co/AlO<sub>x</sub> electrodes, see Figure 5.24(a). Possible candidates for these etch-marks are; HMDS, Ti35, acetone, IPA, or the application of ultrasonic power during the lift-off. These are all the substances the sample is exposed to during the contact pads fabrication step. Fabrication of Co/AlO<sub>x</sub> electrodes and subsequent exposure to one of each of these candidates should give an idea of the cause.
2. A new photolithographic mask should be designed. The current mask has no variation in the distance between two electrodes, which prevents characterisation of the O-FET behaviour as a function of the channel length. Furthermore, all ferromagnetic electrode

patterns are currently of the same size. By introducing shape anisotropy in the new mask, the potential for MR measurements in the transistor device is obtained. Multiple smaller improvements are suggested. These are further discussed in minor recommendation viii.

3. The problems encountered with bonding wires to the first top-gated O-FET devices and the AFM results of the organic layer on these devices indicate that the current process for etching the organic layer using reactive ion beam etching (RIBE) is insufficient, see Figure 5.20. Better testing is necessary to optimise this process. As part of this optimisation, determining the etch rate of P3HT as well as determining how much variation occurs in the thickness of parylene coated samples are good points to start.

### 6.1.1 Minor recommendations

There are also many smaller points of improvement that can be made, or interesting topics to investigate.

- i. It may be advantageous to add an adhesion metal such as titanium as a target in the DCA system. With this target available, the platinum contact pads can be fabricated directionally in the DCA. This should improve the quality of lift-off while reducing lift-off times, and thus lowering the exposure of the Co/AlO<sub>x</sub> electrodes to the lift-off solvent.
- ii. Currently, problems are experienced with the Ti35 photoresist when doing accurate alignment in the mask aligner. Sometimes, the sample sticks to the mask, requiring the unloading and cleaning of the mask before the process can continue. This may be caused by the existence of the edge beads, which form on the small square substrates during spin-coating. If the removal of these edge beads can be done accurately and relatively easy, it would make the mask alignment step easier, and provide better resolution since the mask is pressed closer to the actual photoresist layer on the sample.
- iii. AFM measurements show there is some dirt inside the channels where the photoresist does not make direct contact with the substrate, see Figure 5.24(b). This may be problematic, especially for future measurements on back-gated devices. One possible solution may be to add an UV ozone cleaning step after patterning of the photoresist, but before the deposition of the Co/AlO<sub>x</sub> electrodes.
- iv. AFM measurements indicate that the borofloat glass wafers available in the cleanroom have a rougher surface than the thermally grown SiO<sub>2</sub> substrates. This may negatively influence the ferromagnetic electrode performance. Glass was used as a substrate to negate problems with breaking of the SiO<sub>2</sub> layer during bonding of the wires. Testing other wire bonder settings may be an alternative route to solving such problems, re-enabling the use of Si/SiO<sub>2</sub> substrates.
- v. It is currently difficult to accurately gauge when the Cr layer has been completely etched during the Au top-gate patterning step. In these structures, Cr only serves as an adhesion layer, but it has not been tested if this is necessary. If adhesion of Au directly to parylene is sufficient, Cr can be removed from the recipe, and the top-gate patterning step becomes easier.
- vi. In light of the uncertainty about three-terminal Hanle measurements[53], our device is envisioned as a four-terminal device. For this to work, the two inner terminals need to be closer together than can be realised using photolithography. Testing of the electron-beam lithography (EBL) patterns should be started. Especially important to figure out is the

use of a resist with a good undercut, its compatibility with acetone as lift-off solvent, and the speed of writing such patterns.

- vii. The current measurements that were done on back-gated O-FET devices are not directly usable for a scientific publication. New devices should be fabricated and measured while maintaining much tighter control over the variables. In reporting the effectiveness of spin accumulation measurements, such back-gated O-FET measurements would be a nice addition for comparison to top-gated O-FET behaviour. In addition, it is possible to fabricate a dual-gated device, where a Si/SiO<sub>2</sub> substrate doubles as a back-gate, in addition to an Au top-gate structure.
- viii. When fabricating the new photolithographic mask, it is important to take the behaviour of Ti35 photoresist into account. A mask strip of 4 µm wide results, using the current recipe, in a photoresist strip only 2 µm wide. This should also be kept in mind when determining the distance between two contact pads. Currently, such contact pads can be inadvertently connected close to the structure. It may also be useful to connect the gate structure of multiple magnetic O-FET structures together, and increase the size of the contact pads. This should make bonding of the wires to the final structures much easier. Furthermore, an orientation marker should be added at the edge of each pattern. The positions of each individual pattern on the mask should be tweaked such that all are accessible for the mask-aligner.
- ix. The degradation of the current through a top-gated O-FET device, as seen in Figure 5.28, may be caused by undesired reactions of the P3HT layer with the atmosphere. It may be useful to perform future electrical measurements under an inert atmosphere, such as He. This is easily achieved using the current setup of the Bruker system.



# Acknowledgements

This masters assignment took me nearly a year to complete, and would not have been possible without tons of support from many people. I originally joined the NanoElectronics research group because their projects really appealed to me. Spintronics is a hot new research area with plenty of challenges ahead. Thus, I would like to thank prof. Wilfred van der Wiel and dr. Michel de Jong for providing the opportunity to work in this field. Together with Kai Wang, their support and guidance during this project has been of great value, and really helped me to get the most out of it.

I also want to thank the technical staff, especially Johnny Sanderink and Thijs Bolhuis, for their support during my experiments. The entire NanoElectronics group is too big to name everyone, but I would like to thank all those who helped me in some way, as well as those who didn't. Because of the wide range of research projects within the group, there are many people I did not work together with. However, you have all been great fun, even if only during the lunch breaks. My experiments often required me to go into the MESA+ cleanroom. I consider myself lucky to have been able to work in this cleanroom, where everything is well taken care of, and experienced and helpful staff is available. Especially, I want to thank Huib van Vossen for his assistance in optimising the photoresist recipes.

Of course, I cannot forget the support of my family and friends. My parents supported me in every way, and did not freak out (or at least never showed it) when I went off for weekends on end to go skydiving again. To my friends, especially Frederik, Jaco, Dennis, and Jan: Thank you for the awesome times, the awesome jumps, and the awesome trips.

Blue skies!  
Frans van Wijngaarden

January 2014



# List of Acronyms

- AlO<sub>x</sub>** - aluminium oxide  
**AMR** - anisotropic magnetoresistance
- DMSO** - dimethyl sulfoxide
- EBL** - electron-beam lithography  
**EBPVD** - electron-beam physical vapour deposition
- GMR** - giant magnetoresistance
- HOMO** - highest occupied molecular orbital
- LSMO** - lanthanum strontium manganite (La<sub>0.7</sub>Sr<sub>0.3</sub>MnO<sub>3</sub>)  
**LUMO** - lowest unoccupied molecular orbital
- MR** - magnetoresistance
- P3HT** - poly(3-hexylthiophene)
- RIBE** - reactive ion beam etching
- TMR** - tunneling magnetoresistance
- UHV** - ultra-high vacuum



# Bibliography

- [1] David J. Griffiths. *Introduction to Quantum Mechanics*. 2nd Edition. Pearson Education, Inc., 2005 (cit. on p. 1).
- [2] Michel de Jong. *Compendium NanoElectronics*. July 2011 (cit. on pp. 2–5).
- [3] I.I. Mazin. “How to Define and Calculate the Degree of Spin Polarization in Ferromagnets”. In: *Physical Review Letters* 83.7 (Aug. 1999), pp. 1427–1430. DOI: 10.1103/PhysRevLett.83.1427 (cit. on p. 2).
- [4] W. Wulfhekel et al. “Tunneling magnetoresistance through a vacuum gap”. In: *Journal of Magnetism and Magnetic Materials* 242-245 (Apr. 2002), pp. 47–52. DOI: 10.1016/S0304-8853(01)01182-9 (cit. on p. 4).
- [5] Evgeny Y. Tsybmal et al. “Spin-dependent tunnelling in magnetic tunnel junctions”. In: *Journal of Physics: Condensed Matter* 15.4 (Feb. 2003), R109–R142. DOI: 10.1088/0953-8984/15/4/201 (cit. on pp. 4, 6).
- [6] M. Julliere. “Tunneling between ferromagnetic films”. In: *Physics Letters A* 54.3 (Sept. 1975), pp. 225–226. DOI: 10.1016/0375-9601(75)90174-7 (cit. on p. 4).
- [7] J.M. De Teresa. “Role of Metal-Oxide Interface in Determining the Spin Polarization of Magnetic Tunnel Junctions”. In: *Science* 286.5439 (Oct. 1999), pp. 507–509. DOI: 10.1126/science.286.5439.507 (cit. on pp. 5, 21).
- [8] Y. Fan et al. “Exchange bias of the interface spin system at the Fe/MgO interface.” In: *Nature nanotechnology* 8 (June 2013). DOI: 10.1038/nnano.2013.94 (cit. on pp. 5, 29).
- [9] C. Tiusan et al. “Spin tunnelling phenomena in single-crystal magnetic tunnel junction systems”. In: *Journal of Physics: Condensed Matter* 19.16 (Apr. 2007), p. 165201. DOI: 10.1088/0953-8984/19/16/165201 (cit. on pp. 5, 6, 21).
- [10] Jaroslav Fabian et al. “Semiconductor spintronics”. In: *Acta Physica Slovaca. Reviews and Tutorials* 57.4-5 (Jan. 2007), pp. 565–907. DOI: 10.2478/v10155-010-0086-8 (cit. on p. 6).
- [11] David D. Awschalom and Michael E. Flatté. “Challenges for semiconductor spintronics”. In: *Nature Physics* 3.3 (Mar. 2007), pp. 153–159. DOI: 10.1038/nphys551 (cit. on p. 6).
- [12] Supriyo Datta and Biswajit Das. “Electronic analog of the electro-optic modulator”. In: *Applied Physics Letters* 56.7 (1990), p. 665. DOI: 10.1063/1.102730 (cit. on pp. 6, 7).
- [13] G. Schmidt et al. “Fundamental obstacle for electrical spin injection from a ferromagnetic metal into a diffusive semiconductor”. In: *Physical Review B* 62.8 (Aug. 2000), R4790–R4793. DOI: 10.1103/PhysRevB.62.R4790 (cit. on p. 6).
- [14] R. Fiederling et al. “Injection and detection of a spin-polarized current in a light-emitting diode”. In: *Nature* 402 (Dec. 1999), pp. 787–790. DOI: dx.doi.org/10.1038/45502 (cit. on p. 6).

- [15] M.P. de Jong et al. “Electronic structure of  $\text{La}_{0.7}\text{Sr}_{0.3}\text{MnO}_3$  thin films for hybrid organic/inorganic spintronics applications”. In: *Journal of Applied Physics* 94.11 (Nov. 2003), p. 7292. DOI: 10.1063/1.1625081 (cit. on p. 6).
- [16] A. Fert and H. Jaffrès. “Conditions for efficient spin injection from a ferromagnetic metal into a semiconductor”. In: *Physical Review B* 64.18 (Oct. 2001), p. 184420. DOI: 10.1103/PhysRevB.64.184420 (cit. on p. 6).
- [17] Saroj P. Dash et al. “Electrical creation of spin polarization in silicon at room temperature.” In: *Nature* 462.7272 (Nov. 2009), pp. 491–4. DOI: 10.1038/nature08570 (cit. on pp. 7, 13, 24, 25).
- [18] R.S. Patel et al. “Magnetic tunnel contacts to silicon with low-work-function ytterbium nanolayers”. In: *Journal of Applied Physics* 106.1 (July 2009), p. 016107. DOI: 10.1063/1.3159638 (cit. on p. 7).
- [19] C. Herrmann et al. “Organic radicals as spin filters.” In: *Journal of the American Chemical Society* 132.11 (Mar. 2010), pp. 3682–4. DOI: 10.1021/ja910483b (cit. on p. 7).
- [20] Hee Taek Yi et al. “Ultra-flexible solution-processed organic field-effect transistors.” In: *Nature communications* 3 (Jan. 2012), p. 1259. DOI: 10.1038/ncomms2263 (cit. on p. 7).
- [21] Yang Wan Kim et al. “9.1: 40 Inch FHD AM-OLED Display with IR Drop Compensation Pixel Circuit”. In: *SID Symposium Digest of Technical Papers* 40.1 (July 2009), pp. 85–87. DOI: 10.1889/1.3256930 (cit. on p. 7).
- [22] Hyunkoo Lee et al. “Improvement of electron injection in inverted bottom-emission blue phosphorescent organic light emitting diodes using zinc oxide nanoparticles”. In: *Applied Physics Letters* 96.15 (Mar. 2010), p. 153306. DOI: 10.1063/1.3400224 (cit. on p. 7).
- [23] Paula Yurkanis Bruice. *Organic Chemistry*. Fourth Edition. Prentice Hall, 2004 (cit. on pp. 8, 9).
- [24] Veaceslav Coropceanu et al. “Charge transport in organic semiconductors.” In: *Chemical reviews* 107.4 (Apr. 2007), pp. 926–52. DOI: 10.1021/cr050140x (cit. on pp. 9, 18, 20, 40).
- [25] Editorial. “Why going organic is good.” In: *Nature materials* 8.9 (Sept. 2009), p. 691. DOI: 10.1038/nmat2517 (cit. on p. 10).
- [26] S. Sanvito and A.R. Rocha. “Molecular-Spintronics: the art of driving spin through molecules”. In: *Journal of Computational and Theoretical Nanoscience* 3 (May 2006), pp. 624–642. arXiv: 0605239v1 [arXiv:cond-mat] (cit. on p. 10).
- [27] V.I. Krinichnyi et al. “EPR and charge-transport studies of polyaniline”. In: *Physical Review B* 55.24 (June 1997), pp. 16233–16244. DOI: 10.1103/PhysRevB.55.16233 (cit. on p. 10).
- [28] B.R. Gautam et al. “Magnetic field effect on excited-state spectroscopies of  $\pi$ -conjugated polymer films”. In: *Physical Review B* 85.20 (May 2012), p. 205207. DOI: 10.1103/PhysRevB.85.205207 (cit. on pp. 10, 23).
- [29] Tho D. Nguyen et al. “Isotope effect in spin response of  $\pi$ -conjugated polymer films and devices.” In: *Nature materials* 9.4 (Apr. 2010), pp. 345–52. DOI: 10.1038/nmat2633 (cit. on pp. 10, 23).
- [30] A. Fert et al. “Semiconductors Between Spin-Polarized Sources and Drains”. In: *IEEE Transactions on Electron Devices* 54.5 (May 2007), pp. 921–932. DOI: 10.1109/TED.2007.894372 (cit. on p. 10).

- [31] M. Gobbi et al. “C60/NiFe combination as a promising platform for molecular spintronics”. In: *Organic Electronics* 13.3 (Mar. 2012), pp. 366–372. DOI: 10.1016/j.orgel.2011.12.002 (cit. on p. 10).
- [32] M. Wheeler et al. “Enhanced Exchange Bias of Spin Valves Fabricated on Fullerene-Based Seed Layers”. In: *IEEE Transactions on Magnetism* 48.11 (Nov. 2012), pp. 3047–3050. DOI: 10.1109/TMAG.2012.2198200 (cit. on p. 10).
- [33] Sabine Steil et al. “Spin-dependent trapping of electrons at spinterfaces”. In: *Nature Physics* 9.3 (Feb. 2013), pp. 1–6. DOI: 10.1038/nphys2548 (cit. on pp. 10, 13, 24).
- [34] Sayani Majumdar et al. “Comparing small molecules and polymer for future organic spin-valves”. In: *Journal of Alloys and Compounds* 423.1-2 (Oct. 2006), pp. 169–171. DOI: 10.1016/j.jallcom.2005.12.104 (cit. on pp. 10, 11).
- [35] V.A. Dediu et al. “Spin routes in organic semiconductors.” In: *Nature materials* 8.9 (Sept. 2009), pp. 707–16. DOI: 10.1038/nmat2510 (cit. on pp. 10, 11).
- [36] K.V. Raman et al. “Interface-engineered templates for molecular spin memory devices.” In: *Nature* 493.7433 (Jan. 2013), pp. 509–13. DOI: 10.1038/nature11719 (cit. on p. 10).
- [37] Tho D. Nguyen et al. “Spin diffusion in fullerene-based devices: Morphology effect”. In: *Physical Review B* 87.7 (Feb. 2013), p. 075205. DOI: 10.1103/PhysRevB.87.075205 (cit. on p. 10).
- [38] Fujian Wang and Z. Vally Vardeny. “Recent advances in organic spin-valve devices”. In: *Synthetic Metals* 160.3-4 (Feb. 2010), pp. 210–215. DOI: 10.1016/j.synthmet.2009.10.014 (cit. on p. 10).
- [39] Florian Machui et al. “Determination of the P3HT:PCBM solubility parameters via a binary solvent gradient method: Impact of solubility on the photovoltaic performance”. In: *Solar Energy Materials and Solar Cells* 100 (May 2012), pp. 138–146. DOI: 10.1016/j.solmat.2012.01.005 (cit. on pp. 11, 46).
- [40] W. Osikowicz et al. “Energetics at Au top and bottom contacts on conjugated polymers”. In: *Applied Physics Letters* 88.19 (May 2006), p. 193504. DOI: 10.1063/1.2201627 (cit. on p. 11).
- [41] Sota Ukai et al. “Electrical Conduction of Regioregular and Regiorandom Poly(3-hexylthiophene) Doped with Iodine”. In: *Journal of the Physics Society Japan* 74.12 (Dec. 2005), pp. 3314–3319. DOI: 10.1143/JPSJ.74.3314 (cit. on p. 11).
- [42] Ralf Mauer et al. “The Impact of Polymer Regioregularity on Charge Transport and Efficiency of P3HT:PCBM Photovoltaic Devices”. In: *Advanced Functional Materials* 20.13 (May 2010), pp. 2085–2092. DOI: 10.1002/adfm.201000320 (cit. on p. 11).
- [43] H. Sirringhaus. “Device Physics of Solution-Processed Organic Field-Effect Transistors”. In: *Advanced Materials* 17.20 (Oct. 2005), pp. 2411–2425. DOI: 10.1002/adma.200501152 (cit. on p. 11).
- [44] Clément Barraud et al. “Unravelling the role of the interface for spin injection into organic semiconductors”. In: *Nature Physics* 6.8 (June 2010), pp. 615–620. DOI: 10.1038/nphys1688 (cit. on p. 11).
- [45] Sarah Holliday et al. “Advances in Charge Carrier Mobilities of Semiconducting Polymers Used in Organic Transistors”. In: *Chemistry of Materials* 26.1 (2014), pp. 647–663. DOI: 10.1021/cm402421p (cit. on p. 11).

- [46] Shinuk Cho et al. “Thermal annealing-induced enhancement of the field-effect mobility of regioregular poly(3-hexylthiophene) films”. In: *Journal of Applied Physics* 100.11 (Dec. 2006), p. 114503. DOI: 10.1063/1.2400796 (cit. on p. 12).
- [47] N.A. Morley et al. “Room temperature organic spintronics”. In: *Journal of Applied Physics* 103.7 (Jan. 2008), 07F306. DOI: 10.1063/1.2829245 (cit. on p. 12).
- [48] Li Jinhua. “Low-voltage Organic Thin Film Transistors Based on High-k Gate Insulators”. PhD thesis. The Hong Kong Polytechnic University, 2012 (cit. on p. 12).
- [49] A.J. Drew et al. “Direct measurement of the electronic spin diffusion length in a fully functional organic spin valve by low-energy muon spin rotation.” In: *Nature materials* 8.2 (Feb. 2009), pp. 109–14. DOI: 10.1038/nmat2333 (cit. on p. 13).
- [50] L. Nuccio et al. “Electron spin relaxation in organic semiconductors probed through  $\mu$ SR”. In: *Journal of Physics: Conference Series* 292 (Apr. 2011), p. 012004. DOI: 10.1088/1742-6596/292/1/012004 (cit. on pp. 13, 15).
- [51] Mirko Cinchetti et al. “Determination of spin injection and transport in a ferromagnet/organic semiconductor heterojunction by two-photon photoemission.” In: *Nature materials* 8.2 (Feb. 2009), pp. 115–9. DOI: 10.1038/nmat2334 (cit. on p. 13).
- [52] M. Tran et al. “Enhancement of the Spin Accumulation at the Interface between a Spin-Polarized Tunnel Junction and a Semiconductor”. In: *Physical Review Letters* 102.3 (Jan. 2009), p. 036601. DOI: 10.1103/PhysRevLett.102.036601 (cit. on pp. 13, 24).
- [53] Oihana Txoperena et al. “How reliable are Hanle measurements in metals in a three-terminal geometry?” In: arXiv:1211.7273 [cond-mat.mes-hall] (Nov. 2012). arXiv: 1211.7273 (cit. on pp. 13, 14, 24, 72).
- [54] R. Meservey et al. “Magnetic Field Splitting of the Quasiparticle States in Superconducting Aluminum Films”. In: *Physical Review Letters* 25.18 (Nov. 1970), pp. 1270–1272. DOI: 10.1103/PhysRevLett.25.1270 (cit. on p. 13).
- [55] P. LeClair. *Laboratory web-page*. <http://bama.ua.edu/~pleclair/research.html>. Accessed January 2014 (cit. on p. 14).
- [56] Luisa Torsi et al. “Organic field-effect transistor sensors: a tutorial review.” In: *Chemical Society reviews* 42.22 (Nov. 2013), pp. 8612–28. DOI: 10.1039/c3cs60127g (cit. on pp. 18, 19).
- [57] Robert A. Street. “Thin-Film Transistors”. In: *Advanced Materials* 21.20 (May 2009), pp. 2007–2022. DOI: 10.1002/adma.200803211 (cit. on p. 18).
- [58] Jana Zaumseil and Henning Sirringhaus. “Electron and ambipolar transport in organic field-effect transistors.” In: *Chemical reviews* 107.4 (Apr. 2007), pp. 1296–323. DOI: 10.1021/cr0501543 (cit. on pp. 18, 19).
- [59] M. Grünewald et al. “Large room-temperature magnetoresistance in lateral organic spin valves fabricated by in situ shadow evaporation”. In: *Organic Electronics* 14.8 (Aug. 2013), pp. 2082–2086. DOI: 10.1016/j.orgel.2013.04.049 (cit. on p. 18).
- [60] J. Callaway and C.S. Wang. “Energy bands in ferromagnetic iron”. In: *Physical Review B* 16.5 (Sept. 1977), pp. 2095–2105. DOI: 10.1103/PhysRevB.16.2095 (cit. on p. 21).
- [61] “Magnesium oxide (MgO) band structure”. In: *II-VI and I-VII Compounds; Semimagnetic Compounds*. Ed. by O. Madelung et al. Vol. 41B. Landolt-Börnstein - Group III Condensed Matter. Springer Berlin Heidelberg, 1999, pp. 1–5. DOI: 10.1007/10681719\_203 (cit. on p. 21).

- [62] P. LeClair et al. “Large magnetoresistance using hybrid spin filter devices”. In: *Applied Physics Letters* 80.4 (Jan. 2002), p. 625. DOI: 10.1063/1.1436284 (cit. on p. 21).
- [63] M.W. Wu et al. “Spin dynamics in semiconductors”. In: *Physics Reports* 493.2-4 (Aug. 2010), pp. 61–236. DOI: 10.1016/j.physrep.2010.04.002 (cit. on pp. 22, 23).
- [64] J.B. Ko et al. “Detection of the Rashba Effect in a Two-Dimensional Electron Gas”. In: *Electronic Materials Letters* 2.1 (2006), pp. 49–52 (cit. on p. 22).
- [65] L. Nuccio et al. “Importance of Spin-Orbit Interaction for the Electron Spin Relaxation in Organic Semiconductors”. In: *Physical Review Letters* 110.21 (May 2013), p. 216602. DOI: 10.1103/PhysRevLett.110.216602 (cit. on p. 23).
- [66] Z.G. Yu. “Spin-Orbit Coupling, Spin Relaxation, and Spin Diffusion in Organic Solids”. In: *Physical Review Letters* 106.10 (Mar. 2011), p. 106602. DOI: 10.1103/PhysRevLett.106.106602 (cit. on p. 23).
- [67] N.J. Harmon and M.E. Flatté. “Distinguishing Spin Relaxation Mechanisms in Organic Semiconductors”. In: *Physical Review Letters* 110.17 (Apr. 2013). DOI: 10.1103/PhysRevLett.110.176602 (cit. on p. 23).
- [68] Sang-Yun Lee et al. “Tuning hyperfine fields in conjugated polymers for coherent organic spintronics.” In: *Journal of the American Chemical Society* 133.7 (Feb. 2011), pp. 2019–21. DOI: 10.1021/ja108352d (cit. on p. 23).
- [69] J. Campbell Scott. “Metal-organic interface and charge injection in organic electronic devices”. In: *Journal of Vacuum Science & Technology A: Vacuum, Surfaces, and Films* 21.3 (Mar. 2003), p. 521. DOI: 10.1116/1.1559919 (cit. on p. 24).
- [70] M. Yunus et al. “Ambipolar electrical spin injection and spin transport in organic semiconductors”. In: *Journal of Applied Physics* 103.10 (2008), p. 103714. DOI: 10.1063/1.2917215 (cit. on p. 24).
- [71] Wouter J. M. Naber. “Electron transport and spin phenomena in hybrid organic/inorganic systems”. PhD thesis. Enschede: University of Twente, Feb. 2010. DOI: 10.3990/1.9789036529884 (cit. on p. 29).
- [72] Wikimedia Commons. *Dark Field Microscope*. 2006. URL: [https://commons.wikimedia.org/wiki/File:Dark\\_Field\\_Microscope.png](https://commons.wikimedia.org/wiki/File:Dark_Field_Microscope.png) (cit. on p. 32).
- [73] K. Wang et al. “Tunneling anisotropic magnetoresistance in Co/AlO<sub>x</sub>/Al tunnel junctions with fcc Co (111) electrodes”. In: *Physical Review B* 88.5 (Aug. 2013), p. 054407. DOI: 10.1103/PhysRevB.88.054407 (cit. on p. 39).
- [74] MicroChemicals GmbH. *Image Reversal Photoresists*. [http://www.microchemicals.com/products/photoresists/image\\_reversallift\\_off.html](http://www.microchemicals.com/products/photoresists/image_reversallift_off.html). Accessed January 2014 (cit. on p. 41).



# Appendix A

## Fabrication recipes

### A.1 Top-gated organic field-effect transistor

#### A.1.1 Preparation

1. Pick an appropriate substrate. Possibilities include:
  - Highly doped n-type Si with a thermally grown SiO<sub>2</sub> layer. To avoid problems with wirebonding, the SiO<sub>2</sub> layer should be sufficiently thick (>300 nm).
  - Borofloat glass (normally available in the MESA+ cleanroom) can also be used, and does not have problems with wirebonding.
2. Dice the wafer into smaller substrates 11 mm by 11 mm.
3. Clean the substrates in acetone for 15 min in wetbench 11. Place the beaker in an ultrasonic bath at the highest power. Rinse for 10 min in isopropanol in an ultrasonic bath at the highest power. Spin-dry the substrates.

#### A.1.2 Magnetic electrodes

4. Apply and pattern Ti35ES resist:
  - Dehydration bake: >5 min on the 120 °C hotplate.
  - Spin-coat HMDS, using the 4000DYN recipe. Use a 0.2 µm filter on the bottle.
  - Spin-coat Ti35ES, using the 4000DYN recipe. Use a 0.45 µm filter on the bottle.
  - Bake for 120 s on the 95 °C hotplate.
  - Use the "FM contacts" mask. The exposure time is 23 s.
  - Leave in the yellow cleanroom area for >60 min to stabilise.
  - Reversal-bake for 120 s on the 120 °C hotplate.
  - Flood exposure time is 60 s.
  - Develop for 45 s in fresh OPD4262, rinse thoroughly with DI water afterwards. If using the Quick Dump Rinse, only use recipe 2.
  - Inspect optically. Both the patterns and the markers should be clearly defined. Clean with acetone and repeat if they are not.

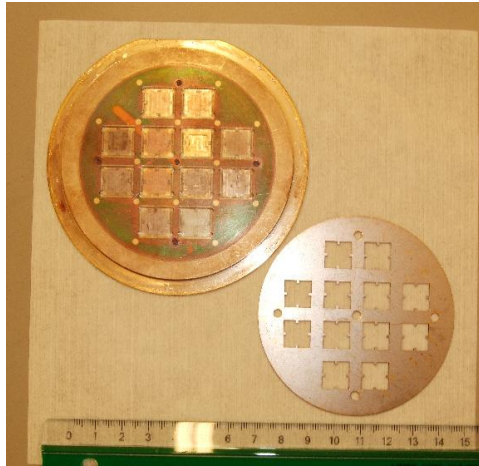


**Figure A.1** – The holder used for clamping the samples in the DCA. It is marked TCoater holder. Do not use the other holder marked RIBE! The scale shown is in cm.

5. Deposit 10 nm cobalt and 2.5 nm aluminium using the DCA M600 system. Take care to orient all the samples towards E-gun 2. Use the holder shown in Figure A.1 and rotate accordingly, see Figure 3.3.
6. Do the lift-off in acetone.
  - Place the substrates in a vertical holder found in the cupboard under WB2, and place into a beaker with acetone.
  - Place this in the ultrasonic bath, and turn on the ultrasonic power at the highest setting. Turn on the heater of the ultrasonic bath to 80 °C. It will not reach this, but increasing the water temperature will help.
  - Lift-off should take 30-60 min.
7. Oxidise the aluminium tunnel barrier inside the loadlock of the DCA for 30 min.
  - With the samples inside, pump down the loadlock to below  $1 \times 10^{-7}$  Torr.
  - Switch the turbo pump to low speed. Wait until it reaches a speed of 37 krpm. Turn off the ion gauge in the loadlock and in the main chamber.
  - Open the nitrogen purge valve at the back of the turbo pump such that the markers align.
  - Close the turbo gatevalve until it is nearly fully closed.
  - Set the mass flow controller to 100 sccm oxygen flow.
  - Open the oxygen valve at the wall, and slowly open the oxygen valve below the loadlock. Regulate the pressure rise with this valve to a slow increase.
  - When the valves are all open, regulate the pressure inside the loadlock to 100 mTorr by opening the gatevalve slightly.
  - After oxidation, close all oxygen valves. Slowly open the turbo gatevalve. Switch the turbopump back to normal speed (56 krpm). Pump down the loadlock for a few minutes before venting and closing the nitrogen purge valve.

### A.1.3 Contact pads

8. Spin-coat Ti35 photoresist.
  - Use the same recipe as step 4. This time, use the "Contact Pads" pattern on the mask.
  - Align the mask markers on marker 2 on the substrate. Do this alignment very carefully, it is the most critical one.
  - Alignment may be easier if the keypad of the mask aligner is used for fine alignment. The movement after a single key-press can be changed in the mask aligner software.
9. Deposit 5 nm of Ti or Cr adhesion layer in Sputterke, followed by 50 nm of Pt or Au (depending on which targets are available). The Ti/W target can also be used as adhesion layer.
10. Do the lift-off in acetone.
  - Place the substrates in a vertical holder, and place into a beaker with acetone.
  - Place this in the ultrasonic bath, and turn on the ultrasonic power at the highest setting. Turn on the heater of the ultrasonic bath to 80 °C. It will not reach this, but increasing the water temperature will help.
  - Lift-off should take 30-60 min.

### A.1.4 Organic layers

11. Spin-coat P3HT in wetbench 23. Also spin-coat P3HT on three dummy substrates.
  - Get the following from the NE cupboard: "FvW separation wafer (P3HT contaminated)"; pipet, including pistons and tips; timer; P3HT solution. Make new stock using the recipe in Appendix A.2 if the current stock is insufficient.
  - Turn the hotplate to 90 °C and place the separation wafer on it. Ensure the dwell time is long enough.
  - Wrap aluminium foil all around the inside of the spin-coater, as well as around the cover.
  - Clean the chuck for small samples using acetone and a few cleanroom tissues and insert it in the spin-coater.
  - Place the samples on the 90 °C hotplate for >5 min, to drive off water.
  - Deposit the P3HT solution by pipet to the middle of the sample. Use 50 µl for 11 mm by 11 mm samples.
  - The spin-coating recipe is named "FVW P3HT". This recipe spins the sample at 500 rpm for 10 s, followed by the main step at 6000 rpm for 45 s, adjust the main step rotation speed if necessary. See the P3HT thickness calibration data in Figure 5.4.
  - Anneal the samples on the 90 °C hotplate for 60 min. Place them on the separation wafer to prevent contamination of the hotplate.
  - Ensure the wetbench is fully cleaned! Aluminium foil and pipet tips are contaminated with halogenated organic solvents. Carefully put it all in a plastic bag marked "P3HT and 1,2-dichlorobenzene" and place it in the waste fumehood next to WB11.

12. Coat parylene on the samples. Add the three P3HT-coated dummy samples. People who can use the parylene coater include Kai Wang, Liang Du, Bojian Xu, and Johnny Sanderink.
13. Determine the thickness of P3HT and parylene on one dummy sample. For example, use Dektak or AFM.

### A.1.5 Gate etching

14. Cover up the alignment markers with photoresist.
  - Using a pipet piston, very carefully apply a small amount of 907-17 resist to the corners of the samples.
  - Bake for 90 s at 95 °C.
  - Check under a microscope. The markers should be fully covered, while none of the structures are covered. Wash the resist off and try again if this is not the case.
15. Deposit 5 nm of Cr (adhesion layer) and 50 nm of Au in the Sputterke. Add three dummy substrates.
16. Do lift-off of the marker covers in acetone for 15 min in wetbench 11. Place the beaker in an ultrasonic bath at the highest power. Rinse for 10 min in isopropanol in an ultrasonic bath at the highest power. Spin-dry the substrates.
17. Apply positive photoresist as etch mask for gate etching to both the structure samples and the dummy samples.
  - Dehydration bake: >5 min on the 120 °C hotplate.
  - Spin-coat HMDS, using the 4000DYN recipe. Use a 0.2 µm filter on the bottle.
  - Spin-coat 907-17, using the 4000DYN recipe. Use a 0.45 µm filter on the bottle.
  - Bake for 90 s on the 95 °C hotplate.
  - Use the "Gate electrodes" mask. The exposure time is 4 s. Align on marker 3 of the substrate.
  - Bake for 60 s on the 120 °C hotplate.
  - Develop for 45 s in fresh OPD4262, rinse thoroughly with DI water afterwards. If using the Quick Dump Rinse, only use recipe 2.
  - Hard-bake for 10 min on the 120 °C hotplate.
  - Inspect optically. Clean with acetone and repeat if the alignment is wrong, or if the resist looks bad.
18. Etch the Au/Cr layer.
  - In WB9 or WB10, prepare beakers with gold etchant, chromium etchant and DI water. Label accordingly. Wear a chemical skirt and protective gloves when pouring the etchants!
  - Check the etch time of Au with one dummy sample. Etch rate is approximately 50 nm min<sup>-1</sup>, but can vary significantly. Inspect the dummy sample by microscope, and adjust the etch time as necessary.

- When etching, always rinse the samples afterwards with DI water. If using the Quick Dump Rinse, only use recipe 2.
  - Chromium etchant has an etch rate of approximately  $60 \text{ nm min}^{-1}$ , but can also vary significantly. Again, check the actual etch time required with the dummy samples.
19. Clean the substrates in acetone for 15 min in wetbench 11. Place the beaker in an ultrasonic bath at the highest power. Rinse for 10 min in isopropanol in an ultrasonic bath at the highest power. Spin-dry the substrates.

### A.1.6 Organic etching

20. Apply positive resist as organic etch mask. Use the same recipe as step 17.
- Use the "Organic Etch" mask pattern. Rotate the mask (and sample holder)  $90^\circ$  before putting it into the mask aligner. Otherwise, the optics cannot reach the alignment markers.
  - Align on marker 4.
21. Etch the organic parylene/P3HT layer using RIBE. People who can do this include Johnny Sanderink, Elmer van Geijn, and Saurabh Bose.
- Organic etching in the RIBE needs 5 sccm Ar flow to the neutraliser and 10 sccm  $\text{O}_2$  to the beam.
  - Etch rate of parylene is approximately  $60 \text{ nm min}^{-1}$ .
  - The etch rate of P3HT is not known, but is assumed to be similar to parylene.
  - Use the dummy samples to check the etch rate, if desired.
22. Clean the substrates in acetone for 15 min in wetbench 11. Place the beaker in an ultrasonic bath at the highest power. Rinse for 10 min in isopropanol in an ultrasonic bath at the highest power. Spin-dry the substrates.
23. Fabrication is now finished!

## A.2 P3HT solution preparation

This recipe prepares the P3HT solution for spin-coating during fabrication of the organic field-effect transistor (see Section A.1). P3HT can be dissolved in 1,2-dichlorobenzene or bromobenzene, and preparation takes place in the MnF chemical laboratory. You should always wear safety goggles, safety gloves, and a labcoat.

The concentration obtained by this recipe is  $10 \text{ mg ml}^{-1}$ . Adjust the amount in step 4 if a different concentration is desired.

1. Gather the following items:
  - 5 ml glass vial and cap
  - Cleanroom tissue
  - Stock bottle of P3HT
  - Metal spoon for weighing
  - Weighing paper

- stock bottle of solvent
  - 1 ml syringe + long needle (for getting solvent from stock)
  - 18 G 1 1/2 syringe needle (pink)
  - Balloon with rubber cap (in cupboard to the right of NE fumehood)
- 
- 0.2  $\mu\text{m}$  filter
  - 2x 1 ml syringe
  - 2x 18 G 1 1/2 needle (pink)
  - 5 ml glass vial
  - 2 ml glass vial, with screw-on cap, label it.
2. Take the first five items to the other chemical laboratory for weighing (more accurate scale).
  3. Fold the weighing paper, put it on the scale and zero it.
  4. Weigh 10 mg of P3HT (black powder-like substance). Get it from the bottle using the metal spoon.
  5. Carefully empty the weighing paper into the 5 ml glass vial, and close it.
  6. Go back to the NE fumehood, and take out the stock bottle of solvent.
  7. Using the 1 ml syringe attached to the long syringe needle, withdraw 1 ml of solvent from the bottle.
  8. Carefully and slowly empty the syringe in the 5 ml glass vial with P3HT in it.
  9. Push the attachment end of the pink needle in the rubber cap of the balloon, and push the needle through the plastic cap of the 5 ml glass vial.
  10. Put the stirring magnet labelled "For P3HT only!" into the 5 ml glass vial, and close it with the cap with needle pushed through it.
  11. Clamp it in the clamp above the oil bath and stirrer. Take care to clamp it low enough so the vial can touch the oil. Try it with an empty glass vial if necessary!
  12. Insert the thermocouple into the oil bath, and put the setpoint on 80 °C (this is the actual temperature).
  13. Turn on the heater and put the temperature setpoint on 100 °C (this is the safety temperature).
  14. Turn on the magnetic stirrer, and increase to 300 rpm. Make sure the stirring magnets in the oil AND in the P3HT solution are rotating properly.

15. Let it stir for 3 h. Check on it after 1.5 h. If there is P3HT on the walls of the vial (black specks), then remove it from the clamp and gently swirl the bottle or use a metal weighing spoon to get them into the solvent. Put it back in the clamp and continue with the stirring.
16. Turn off the temperature and stir for 1 h.
17. Take the bottle out of the clamp.
18. With a 1 ml syringe and pink needle, withdraw the solution from the 5 ml glass vial.
19. Remove the needle from the syringe, and attach the 0.2  $\mu\text{m}$  filter.
20. VERY gently empty the syringe through the filter in a clean 5 ml glass vial.
21. Using a NEW 1 ml syringe and pink needle, withdraw again from the 5 ml glass vial, and gently empty in 2 ml glass vial with green screw-on cap.
22. Wrap aluminium foil around the 2 ml vial, label and store in the fridge in the TST laboratory.
23. Clean up the fumehood. Wash the stirrer magnet in acetone, and throw away all chemical waste.